TAMPEREEN TEKNILLINEN YLIOPISTO
TAMPERE UNIVERSITY OF TECHNOLOGY

Juha Huusari

DC-DC Converters in Distributed Photovoltaic Electricity System

Analysis, Control and Design

Julkaisu 1070 • Publication 1070

Tampere 2012

Tampereen teknillinen yliopisto. Julkaisu 1070
Tampere University of Technology. Publication 1070

Juha Huusari

DC-DC Converters in Distributed Photovoltaic Electricity System

Analysis, Control and Design

Thesis for the degree of Doctor of Science in Technology to be presented with due permission for public examination and criticism in Sähkötalo Building, Auditorium S4, at Tampere University of Technology, on the 5th of October 2012, at 12 noon.

Tampereen teknillinen yliopisto - Tampere University of Technology
Tampere 2012

ISBN 978-952-15-2901-6 (printed)
ISBN 978-952-15-2917-7 (PDF)
ISSN 1459-2045

ABSTRACT

This thesis presents a comprehensive review on switched-mode converters in terms of dynamic behavior and practical limitations that arise from the fundamental properties of the electrical sources and loads, control engineering principles and topological properties of the converters. The main focus is on analyzing the behavior of a single converter used to interface a photovoltaic generator into a high-voltage dc link. The main objective is to introduce interfacing principles with numerous examples and a thorough discussion.

The interfacing of photovoltaic generators by means of switched-mode converters has proven to be problematic according to numerous scientific publications indicating operational disadvantages and anomalies. The output characteristics of the photovoltaic generator, which are bound to varying environmental conditions, introduce design challenges. It has been recognized recently that the photovoltaic generator does not contain similar electrical behavior as conventional electrical sources, most notably due to its limited-power characteristics, yielding two distinctive operating regions. Yet, the constraints arising from the properties of the source have not been completely recognized, although the effect of these constraints can be seen from the published research results. When switched-mode converters are used to adapt individual photovoltaic modules into larger system by connecting converters in series or in parallel, severe operational limitations are observed. On the other hand, if the photovoltaic generator is substituted with a source that does not contain similar characteristics, observations may lead to misconclusions as the effect of the photovoltaic generator is not properly modeled. Therefore, claims that are not valid for actual applications with photovoltaic generators may be presented and widely accepted.

This thesis presents methods to perform proper analysis of switched-mode converters implemented in distributed photovoltaic applications, by continuing previous work around the subject (Leppäaho, 2011). The dynamic models for series-connected and parallel-connected systems of interfacing converters are given, explaining the observed operational anomalies. Additionally, it is shown by a thorough review that the parallel configuration does not contain the claimed disadvantageous properties and actually provides better performance. A patented converter topology designed for the parallel configuration is presented with comprehensive analysis and practical validation. Finally, the problematics of photovoltaic interfacing is summarized under the interfacing constraints, which give guidelines for design and analysis of interfacing converters.

PREFACE

The research and measurements for this thesis were performed at the Department of Electrical Energy Engineering (DEEE) at Tampere University of Technology (TUT) during years 2009–2012. Main contributors to the funding of the research were TUT as well as ABB Ltd. Additionally, personal grants from the Ulla Tuominen Foundation and the Fortum Foundation provided financial support, deserving my special thanks.

The first individual to be thanked is Professor Teuvo Suntio, to whom I express my deepest gratitude for supervising my thesis. I thank you for having trust in me and for providing not only constructive feedback, but also enlightening discussions with groundbreaking concepts, pushing me forward towards the degree. I admire your devotion and inexorability, it has been an honor to work under your guidance. Members of our former research group at TUT, comprising Dr.Tech. Jari Leppäaho, M.Sc. Tuomas Messo, M.Sc. Joonas Puukko, M.Sc. Lari Nousiainen, M.Sc. Anssi Mäki and M.Sc. Diego Torres Lobera had a significant role both in providing professional support and criticism as well as in creating an encouraging and relaxed atmosphere to work in. Thank you all!

I am also most grateful to Professors Adrian Ioinovici and Toshihisa Shimizu for examining my thesis and for the resulting supportive discussion which helped me to improve the quality of the thesis. Further, the staff at the DEEE, most notably Professor Seppo Valkealahti and Secretary Merja Teimonen deserve my thanks for support, as well as the staff at the former Department of Electromagnetism for various sports activities during past years.

Accomplishing these kinds of deeds is not possible without the support of one's closest persons. Therefore, I express my gratitude to my parents, my brothers and family Lauronen for their unfailing support and encouragement during my academic career. Moreover, I thank family Hiltunen for all that they once were to me. Finally, I thank my dear Katariina for her love and patience. Without you, my life would be void.

Zürich, July 2012

Juha Huusari

CONTENTS

SYMBOLS AND ABBREVIATIONS

ABBREVIATIONS

AC, ac	Alternating current
BIPV	Building-integrated photovoltaic
CC	Constant current region
CdTe	Cadmium telluride
CF	Refers to current-fed system or interface
CFQFB	Current-fed quadratic full-bridge
CIGS	Copper indium gallium selenide
CSP	Concentrating solar power
CV	Constant voltage region
DC, dc	Direct current
DSC	Digital signal controller
DMPPT	Distributed maximum power point tracking
EA	Refers to a certain electronic load
EMI	Electromagnetic interference
FRA	Frequency response analyzer
GCC	Generation control circuit
LHP	Left half of the complex plane
NREL	National renewable energy laboratory (U.S.)
MIC	Module-integrated converter
MOSFET	Metal-oxide-semiconductor field-effect transistor
MPPT	Maximum power point tracking
MPP	Maximum power point
PID	Proportional integral derivative
PV	Photovoltaic
RHP	Right half of the complex plane
SAS	Solar array simulator
Si	Silicon
VF	Refers to voltage-fed system or interface
VSI	Voltage source inverter
XFR	Transformer

GREEK CHARACTERS

Θ	Angle of incidence of solar irradiation
η	Efficiency or ideality factor
λ	Wavelength

ϕ	Phase angle
ω	Angular frequency

LATIN CHARACTERS

$\mathbf{A}$	State coefficient matrix A
$\mathbf{B}$	State coefficient matrix B
C	Capacitance
C	Capacitor
$\mathbf{C}$	State coefficient matrix C
c	Speed of light in vacuum or control variable
c_{pv}	Capacitance of a PV cell
$\hat{c}$	Perturbed control signal
$\mathbf{D}$	State matrix D
D, d	Duty cycle
D', d'	Complementary duty cycle
D	Diode
E	Energy
E_{G}	Band gap energy
$\hat{e}$	Perturbed error signal
f	Frequency
f_{s}	Switching frequency
$\mathbf{G}_{\mathrm{L}}$	Transfer functions of a load sub-system
$\mathbf{G}_{\mathrm{S}}$	Transfer functions of a source sub-system
G	Irradiance
G_{11}	Ohmic characteristics of the input terminal
G_{22}	Ohmic characteristics of the output terminal
G_{c}	Gain of the control loop
G_{cc}	Controller transfer function
G_{ci}	Control-to-input transfer function
G_{co}	Control-to-output transfer function
G_{cr}	Control cross-coupling transfer function
G_{io}	Forward transfer function
G_{ioS}	Forward transfer function of a source sub-system
G_{ioL}	Forward transfer function of a load sub-system
G_{se}	Sensing gain
h	Planck's constant
$\mathbf{I}$	Identity matrix
I_{L}	Average current through load or average inductor current
I_{mpp}	Current of the maximum power point
i_{ac}	Instantaneous current delivered to the utility grid

i_{in}	Refers to input current
i_{ph}	Current generated via photovoltaic effect (the photocurrent)
i_{pv}	Terminal current of a PV cell
I_{S}	Source current
I_{s}	Saturation current of a PV cell
I_{sc}	Short-circuit current of a PV cell
i_{L}	Instantaneous inductor current
i_{S}	Instantaneous source current
i_{T}	Instantaneous terminal current
$\hat{i}$	Perturbed current
Δi_{pv}	Incremental change in the terminal current of a PV cell
$\langle i \rangle$	Time-averaged current
j	Complex variable
k	Boltzmann's constant
k_1	Open-circuit voltage coefficient
k_2	Short-circuit current coefficient
L	Inductance
L	Inductor
L_{M}	Magnetizing inductance of a transformer
L_{m}	Conventional minor-loop gain (i.e., for voltage-fed system)
$L_{\mathrm{m,inv}}$	Inverse minor-loop gain (i.e., for current-fed system)
L_{v}	Loop gain for input-voltage control loop
M, m	Converter-specific modulo
N_1	Number of turns in the primary winding of a transformer
N_2	Number of turns in the secondary winding of a transformer
n	Turns ratio of transformer windings
P_{in}	Average input power of a converter
P_{out}	Average output power of a converter
P_{pv}	Average output power of a photovoltaic generator
p_{ac}	Instantaneous power delivered to the utility grid
p_{pv}	Generated power of a PV cell
ΣP_{pv}	Total output power of a system of multiple photovoltaic generators
q	Elementary charge
R	Resistance or coefficient variable
R_{pv}	Static resistance of a PV cell
R_{L}	Load resistance
r_{C}	Equivalent resistance of a capacitor
r_{d}	Dynamic resistance of a diode
r_{D}	Forward resistance of a diode
r_{ds}	Resistance of a switch channel
r_{L}	Equivalent resistance of an inductor

r_{pv}	Dynamic resistance of a PV cell
r_{pri}	Resistance of the primary winding in a transformer
r_{s}	Parasitic series resistance of a PV cell
r_{sec}	Resistance of the secondary winding in a transformer
r_{sh}	Parasitic shunt resistance of a PV cell
S	Switch
s	Laplace variable
T	Temperature
T_{cr}	Input cross-coupling transfer function
T_{d}	Time delay in digital control loop
T_{s}	Switching period
T_{oi}	Reverse transfer function
T_{oiL}	Reverse transfer function of a load sub-system
T_{oiS}	Reverse transfer function of a source sub-system
t	Time
t_{i}	Duration of the active part of the switching period
t_{off}	Duration of non-conduction period of a switch
t_{on}	Duration of conduction period of a switch
$\mathbf{U}$	Frequency-domain vector containing input variables
U	Voltage or coefficient variable
U_{C}	Average voltage of a capacitor
U_{D}	Forward voltage of a diode
U_{L}	Average load voltage
U_{S}	Average source voltage
U_{mpp}	Voltage of the maximum power point
U_{oc}	Open-circuit voltage of a PV cell
U_{link}	Voltage of a dc link
$\mathbf{u}$	Time-domain vector containing input variables
$u_{\mathrm{grid}}, u_{\mathrm{ac}}$	Instantaneous voltage of the utility grid
u_{i}	Refers to an input variable of a system
u_{in}	Refers to input voltage
u_{bridge}	Voltage across the switch bridge
u_{C}	Instantaneous capacitor voltage
u_{pv}	Terminal voltage of a PV cell
u_{ref}	Refers to reference voltage
u_{S}	Instantaneous source voltage
u_{T}	Instantaneous terminal voltage
$\hat{u}$	Perturbed input variable of a system or perturbed voltage
Δu_{pv}	Incremental change in the terminal voltage of a PV cell
$\langle u \rangle$	Time-averaged voltage
$\mathbf{X}$	Frequency-domain vector containing state variables

$\mathbf{x}$	Time-domain vector containing state variables
x_{i}	Refers to a state variable of a system
$\hat{x}$	Perturbed state variable of a system
$\mathbf{Y}$	Frequency-domain vector containing output variables
Y_{o}	Output admittance
Y_{oL}	Output admittance of a load sub-system
Y_{oS}	Output admittance of a source sub-system
Y_{tot}	Total admittance
Y_{S}	Admittance of a non-ideal source
$\mathbf{y}$	Time-domain vector containing output variables
y_{i}	Refers to an output variable of a system
$\hat{y}$	Perturbed output variable of a system
z	Discrete-time variable
Z_{L}	Impedance of a non-ideal load
Z_{in}	Input impedance
Z_{inL}	Input impedance of a load sub-system
Z_{inS}	Input impedance of a source sub-system

SUBSCRIPTS

-c	Closed loop
den	Refers to the denominator of a transfer function
-ins	Refers to an ideal input source
-o	Open loop
-oco	Refers to output terminal open-circuit
max	Refers to defined maximum value
min	Refers to defined minimum value
-sci	Refers to input terminal short-circuit
$-\infty$	Refers to ideal transfer function

SUPERSCRIPTS

-1	Matrix inverse
c	Cross-coupled transfer function
S	Refers to source-affected transfer function or source-related variable
L	Refers to load-affected transfer function or load-related variable
T	Transpose

1 INTRODUCTION

This chapter introduces the background of the research and clarifies the motivation for the conducted research. The operation and essential characteristics of the photovoltaic (PV) generator are discussed, specifically in the light of an electricity system comprising PV generators. A brief introduction to switched-mode converters is given as well due to their integral part of the research topic. In addition, this chapter presents the structure of the thesis and, finally, summarizes the scientific contributions at the end of the chapter.

1.1 Energy Consumption and Renewable Energy Sources

Since the invention of the first practical steam engine in 1712 by Thomas Newcomen and the internal combustion engine in the late 1800s, both social and economic development have been increasingly bound to utilization of various machines and devices. Soon after these two major discoveries were made, their potential in replacing muscle and horsepower was realized. Enabling steady, around-the-clock operation of different branches of industry, a sudden boom in the availability of consumer goods and industrial hardware resulted. A new era known as industrialization began, which had tremendous impacts on our societies. First, consumption became a synonym for development and later for the standard of living. Second, a strong dependence on energy was formed (Mattick et al., 2010).

During the first decades of industrialization, the primary source for energy was coal in its different forms. Being abundant throughout the globe, the early industry was built around extensive use of coal, which continues even now. Although the usage of coal has been increasing, there is a consensus that the combined reserves of coal are vast and not expected to deplete in near future with the current rate of use (Abbott, 2010; Bose, 2010). However, recent political decisions made after the Fukushima incident in Japan in 2011, have accelerated the consumption of coal. Most notably these include the announcement to run down the nuclear power plants in Germany by 2022 (The Federal Government of Germany, 2011).

After the invention of the internal combustion engine, another natural source of energy, oil, became increasingly important. Due to its outstanding energy-per-volume characteristics (Krein (1998) gives an example stating that one liter of gasoline stores about 10 MJ energy), oil has become the single most important means of providing energy to

vehicles and also to make a significant contribution to heating. During the first oil crisis in 1973, it became clear that the global economy had become permanently dependent on this source of energy. In addition, as the oil consumption has been increasing but the amount of discovered oil resources has not increased correspondingly, a critical depletion of oil in near future will be seen (Abbott, 2010; Bose, 2010).

The impact of extensive usage of fossil fuel on the nature has become a major concern during the recent decades. Therefore, various alternative solutions have been proposed and advertised as 'green' options, although the actual effect on the nature may be far from being environmentally friendly. Let us classify the natural sources of energy using two definitions: The other describes the availability or regeneration of the energy resource and the other describes the impact of the resource on the nature when used. For the first definition, a word 'renewable' indicates that the source of energy is vast and cannot be depleted even by increased consumption. For the other, a word 'green' indicates that the source has no significant adverse effect on the nature. Using these two *ad hoc* definitions, a following figure can be drawn, relating some widely used sources to each other. It is evident that a source being both 'renewable' and 'green' would be preferred for long-term energy generation.

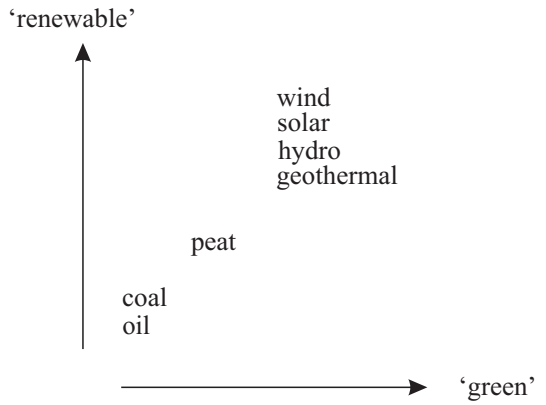

Fig. 1.1. Environmental illustration of some energy sources.

Conventionally, renewable energy sources are considered to include wind energy, hydropower, geothermal energy and solar energy. Of these, hydropower and geothermal energy can be considered not to originate directly from the Sun. Hydropower describes the potential energy available either due to tidal activity on the Earth (ocean energy) or due to natural flow of water towards sea level. Caused by the gravitational forces between Earth and Moon, the sea level rises on the side of Earth that is currently facing the Moon. The equal effect is experienced simultaneously on the opposite side of the Earth. This regularly available potential energy can be converted into usable form of energy,

typically electricity. Practical difficulties related to suitable locations and implementation are evident, yet operational prototypes have been demonstrated (Spagnuolo et al., 2010). On the other hand, harnessing the natural flow of water by building dams is a well-established and widely adopted method to generate electricity (Abbott, 2010; REN21, 2011). In 2010, the estimated global capacity for ocean energy was 6 MW whereas the hydroelectric production reached up to 1010 GW (REN21, 2011).

Geothermal energy is originated from the nuclear reactions taking place in the core of Earth, where the temperature is significantly higher than on the surface on the Earth, creating a thermal gradient forcing a heat flow towards the surface. Geothermal energy is most conveniently utilized directly at the locations where the heat is naturally available, i.e., on the edges of tectonic plates. However, these areas are volcanically active, making the utilization prone to disturbances caused by earthquakes. The approximated capacity of geothermal power plants in 2010 was in the order of 10 GW (REN21, 2011).

It is justified to state that solar energy in its different forms is renewable and green. From mankind's point of view, the Sun is an endless and steady source of energy, which ultimately enables the life on Earth in all those forms that we know it. The energy generation within the Sun is mainly contributed by the proton-proton chain, in which hydrogen is converted into helium through fusion reaction. It is estimated that the power produced by the Sun is approximately 3.486 x 10^{26} W. From this enormous amount the Earth receives approximately 1.74 x 10^{17} W, i.e., 1.74 x 10^{17} J of energy every second. The total approximated annual energy consumption is 4.74 x 10^{20} J, stating that the Earth receives in less than an hour as much energy as mankind uses annually.

The energy released within the Sun is carried away by electromagnetic radiation, i.e., photons, and the arrival of these photons on Earth is referred to as solar irradiation. At Earth's distance from the Sun the irradiation is close to 1361 W/m^2 (Kopp and Lean, 2011). Significant part of this incoming irradiation is either absorbed by the atmosphere or reflected back, blocking photons with certain wavelengths (i.e., certain energies) from arriving at the surface of the Earth (see Fig. 1.2). The amount of irradiation reaching sea level is typically approximated to be 1000 W/m^2.

Solar energy is typically utilized by two main methods: Either by conversion into electrical energy by the photovoltaic effect or by utilizing the heating effect of the incoming irradiation in solar thermal applications. In solar thermal applications, the incoming irradiation is used to heat up water or some other medium, by means of which the heat is transferred into the place of use. Typical applications are low-temperature solar thermal systems, which may be used to provide heating e.g. for residential houses. High-temperature solar thermal systems are conventionally utilized to generate electricity (Cabeza et al., 2011). With concentrators the incoming irradiation can be focused on smaller area, improving the heating effect (concentrating solar power, CSP). With this

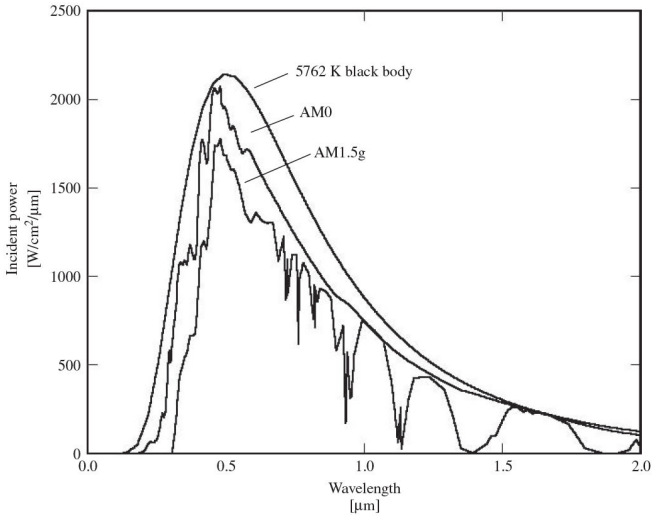

Fig. 1.2. Solar irradiation (Lugue and Hegedus, 2003).

kind of solution, for example water can be heated up to boiling point and the resulting steam can be used to rotate a generator, thus enabling alternating current (ac) to be generated.

1.2 Photovoltaic Electricity

The photovoltaic effect describes the property of certain materials to generate charge carriers, i.e., electrical current when exposed to external electromagnetic radiation. In 1839, a French physicist Alexandre-Edmond Becquerel discovered that when exposed by light, certain materials were able to generate electrical current. The observed phenomenon was explained by Albert Einstein in 1905, of which he was awarded the Nobel Prize in Physics in 1925.

1.2.1 Photovoltaic Cell

The photovoltaic effect and generation of free charge carriers is conveniently explained using the energy band structure, where two different energy levels (i.e., the valence band and the conduction band) describe the behavior of electrons within a certain material. In materials having no free electrons in equilibrium, the valence band is located at lower energy level than the conduction band, meaning that electrons are bound to atomic bonds and hence are unable to move within the structure. If this kind of bound electron receives sufficient amount of energy, it may move up to conduction band and thus become free of atomic bond. The energy difference between the conduction band and the valence

band is known as the energy gap (E_G). The possibility for an electron to move within the material requires that the material contains atomic bonds lacking electrons. Hence, when given enough external energy, a single electron may move freely within the atomic structure, which on a larger scale is observed as electrical current.

The electromagnetic radiation coming from the Sun is divided into discrete packets (photons), each containing a certain amount of energy. The energy carried by a photon is related to its wavelength according to the well-known relation

$$E = \frac{hc}{\lambda}, \tag{1.1}$$

where E describes the photon energy, h the Planck's constant, c the speed of light and λ the wavelength of the photon. The amount of energy required to excite an electron from the valence band into the conduction band is depended on the material properties. Typically, PV cells are manufactured using doped[1] silicon (Si) having energy gap of 1.02 eV, corresponding to a wavelength λ of 1.2 μm, which means that incoming photons must have at least this amount of energy to generate free electrons. Referring to Fig. 1.2, it can be seen that for a certain material, only a narrow part of the Sun's irradiance can be utilized to generate electricity via photovoltaic effect, because the energy content of arriving photons spans over wide range of wavelengths. A photon carrying more energy than the energy gap will not generate more charge carriers, instead, the excess energy will be converted into heat within the material by thermal relaxation (Razykov et al., 2011).

The first practical silicon PV cell was introduced in 1954 by Chapin et al. (1954), achieving an efficiency of 6 % which was significant improvement compared to previous efficiencies of less than 1 percent. The theoretical limit for a single-junction cell depends on the material E_G and for silicon it is approximately 48 % according to Lugue and Hegedus (2003). From the 1950s on the development of different types of PV cell and manufacturing processes has been rapid and vast improvement in the efficiency of a single PV cell has resulted. The PV cells are typically categorized as follows: Silicon-based cells with efficiencies around 20 to 25 %, thin-film cadmium telluride (CdTe) or copper indium gallium diselenide (CIGS) cells having efficiencies generally lower than Si cells and multi-junction cells that achieve the best efficiencies, up to 42 % (Kroposki et al., 2009; Razykov et al., 2011; Wenham and Green, 1996). Emerging technologies, such as dye-sensitized cells and organic cells are studied intensively, yet no commercial breakthrough has been made (Razykov et al., 2011).

In terms of becoming economically feasible, the previously mentioned cell types can be categorized into two main groups, aiming to reduce the cost of produced power by two

[1] Doping means introduction of impurities within a material to obtain a desired semi-conductive behavior.

main approaches. The other approach is to focus on high operational efficiency with elaborate structural solutions, resulting in relatively high manufacturing costs. Silicon-based cells, multi-junction cells and cells operating under concentrated illumination belong to this group. The other approach aims to minimize the manufacturing costs at the expense of the cell efficiency. This group contains thin-film cells, organic and dye-sensitized cells. Figure 1.3 visualizes the evolution of cell manufacturing processes and the obtained efficiencies as summarized by U.S. National Renewable Energy Laboratory (NREL) (Renewable Energy Index, 2011). It is notable that for most cell types, the obtained efficiency has not increased during the past decades, indicating that those technologies are mature and some kind of limit has been reached. On the basis of Fig. 1.3 it seems that multi-junction and organic cells may still see some development in the future.

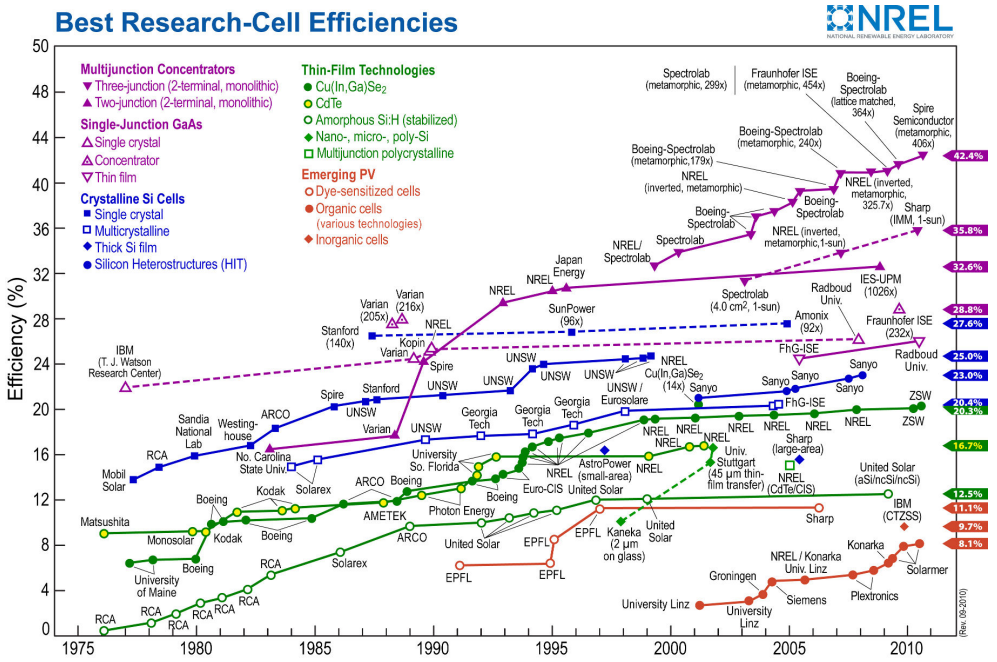

Fig. 1.3. Development of PV cell efficiencies according to NREL.

1.2.2 Behavior of a Photovoltaic Generator

Due to the internal semiconductor junction, essentially all PV cells regardless of the manufacturing method have similar electrical performance. Therefore, it is possible to form an electrical model for a general PV cell using fundamental electrical components, and the behavior of individual cell types can be emulated by altering the numerical parameters of the model. A typical equivalent electrical circuit used to represent a PV

cell is the single-diode circuit shown in Fig. 1.4, (Chenvidhya et al., 2006), where the photocurrent source i_{ph} describes the fundamental source of the produced power due to generation of charge carriers by the photovoltaic effect.

The other parts of the model are the non-ideal diode representing the internal semiconductor junction, the cell capacitance c_{pv}, the shunt resistance r_{sh} and the series resistance r_{s}. The properties of the semiconductor junction yield the non-linear capacitance seen at the cell terminals (Kumar et al., 2006). The shunt resistance originates from various non-idealities of the cell structure down to molecular level, whereas the series resistance is conventionally used to describe losses introduced by the physical construction of the cell, such as the resistance of the cell terminal wires (Lugue and Hegedus, 2003).

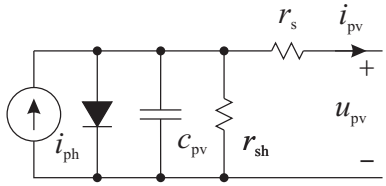

Fig. 1.4. An electrical equivalent model for a PV Cell.

By neglecting the parasitic cell capacitance (i.e., by considering the low-frequency operation only) an equation describing the cell terminal current i_{pv} can be formed according to (1.2), taking the parasitic elements of the equivalent circuit into account. The electrical behavior of the semiconductor diode is modeled by the standard diode equation (Streetman and Banerjee, 2005), where I_{s} represents the dark photocurrent (i.e., the current generated as random thermal movement excites electrons into conduction band), q the elementary charge, k the Boltzmann's constant, T the temperature of the cell and η the ideality factor of the diode.

$$i_{\mathrm{pv}} = i_{\mathrm{ph}} - I_{\mathrm{s}} \left[\exp\left(\frac{q(u_{\mathrm{pv}} - r_{\mathrm{s}} i_{\mathrm{pv}})}{\eta k T} \right) - 1 \right] - \frac{u_{\mathrm{pv}} - r_{\mathrm{s}} i_{\mathrm{pv}}}{r_{\mathrm{sh}}} \tag{1.2}$$

Clearly, the equation does not have a solution in closed form, which is why numerical computation methods are used to find values for terminal current i_{pv} and terminal voltage u_{pv} at a certain operating point. Using the equation (1.2), the characteristic current-voltage curve (Fig. 1.5) can be drawn, visualizing the electrical behavior of a PV cell.

The PV cell terminal current (i_{pv}, solid line) and terminal power ($p_{\mathrm{pv}} = u_{\mathrm{pv}} i_{\mathrm{pv}}$, dashed line) are plotted on the ordinate versus the terminal voltage u_{pv} on the abscissa, with all of these variables represented using per unit values for convenience. According to the figure, at a specific voltage and current the generated power reaches its maximum. This point is known as the maximum power point (MPP) and for energy production purposes it is the desired operating point. Examining the shape of the current-voltage curve, two

distinctive regions can be defined: The constant current region (CC) at terminal voltages lower than the MPP, where the cell current stays almost constant despite the changes in terminal voltage and the constant voltage region (CV) at terminal voltages higher than the MPP, where the terminal voltage stays relatively constant even if the terminal current changes. Considering the generation of photocurrent due to incoming irradiation and the characteristic curve in Fig. 1.5, the PV cell can be said to be a non-ideal current source with limited output power (Shmilovitz and Singer, 2002).

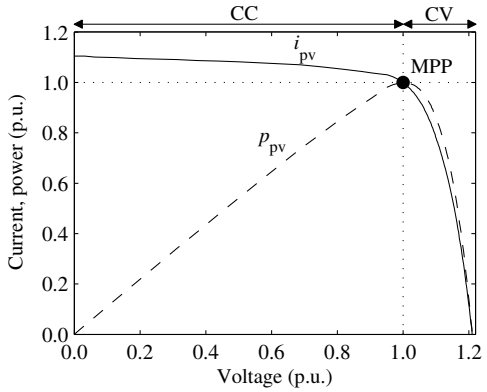

Fig. 1.5. Current-voltage characteristic.

Environmental conditions have significant effect on the electrical performance of a PV cell. Because the band gap energy E_G decreases with temperature, the cell terminal voltage is dependent on the operating temperature. For silicon the temperature coefficient is approximately -2.3 mV/°C, indicating that at low temperatures higher terminal voltages are obtained, increasing the generated power. The short-circuit current, on the other hand, is relatively unaffected by temperature. Instead, the generated current is directly proportional to incoming irradiation. Hence the most beneficial operating conditions for power generation would be at low temperatures with bright sunshine. The curves in Fig. 1.6 illustrate the electrical behavior of a silicon PV cell under varying environmental conditions.

Typical electrical parameters for a silicon PV cell are as follows: The short-circuit current I_{sc} is usually between 3 to 8 amperes and the open-circuit voltage U_{oc} is close to 0.6 volts. The short-circuit current is mainly defined by the physical area of the cell whereas the open-circuit voltage depends on the used material (Lugue and Hegedus, 2003). The voltage at MPP is typically 80 % of the open-circuit voltage and the current at MPP 90 % of the short-circuit current, respectively (Esram and Chapman, 2007).

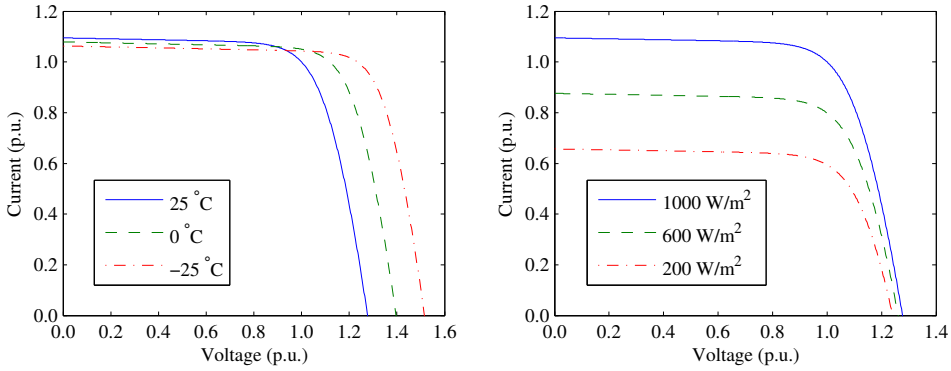

(a) Temperature effects **(b)** Irradiance effects

Fig. 1.6. Effects of varying environmental conditions on electrical operation of PV cell.

Properties of a PV Module

Regardless of the size of a practical PV system, the fundamental building block of the system is a PV module comprising a number of PV cells connected electrically in series, thus enabling convenient power extraction as the voltage level rises. Commercial PV modules contain typically 30 to 60 cells, yielding module open-circuit voltage of approximately $20 - 40$ V with MPP voltage of $18 - 32$ V. The nominal power of a single PV module varies significantly, from 20 W to 240 W.

The physical structure of a PV module imposes significant operational constraints that affect the design of interfacing converters. Due to series connection, if a single cell is shaded, the total current available from the module is limited to the value dictated by the shaded cell. To overcome this, the module is divided into segments, each having own bypass diode in parallel. Thus, if one segment is shaded, the other segments are able to generate nominal current. The difference of the nominal current and the current generated by the shaded segment is diverted into the corresponding bypass diode.

The bypass diodes, therefore, indirectly shape the nominal current-voltage characteristic shown in Fig. 1.5 under shaded conditions. Under uniform illumination, a PV generator (either a cell or a module) has only one MPP. However, under shaded conditions there can be as many MPPs as there are bypass diodes in the system. Therefore, for the previous example module with three bypass diodes, there can be three local MPPs, each at different voltage level. The desired operation for power generation purposes is the global MPP generating highest power. The location of the global MPP is thus constantly changing due to environmental and shading conditions, posing a challenge to the MPP-tracking ability of the interfacing converter. An example situation is presented in

Fig. 1.7, depicting the behavior of a PV module with three bypass diodes when two segments receive reduced irradiation (indicated with relative magnitudes G_1, G_2 and G_3). The global MPP occurs, thus, at approximately 25 % of the open-circuit voltage compared to nominal 80 %. Additionally, at the global MPP twice as much power is generated compared to the local MPP at higher voltage, indicating that the interfacing converter has to be designed to enable power extraction even from low voltage levels.

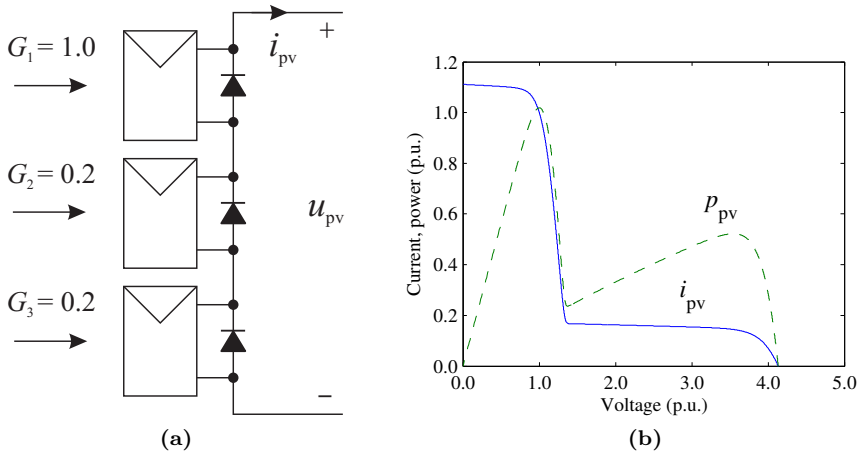

Fig. 1.7. Effect of partial shading on the operation of a PV module with three bypass diodes.

1.3 DC-DC Converters in Photovoltaic Systems

A conventional method to perform power transfer from a certain dc source to a certain dc load is to utilize switched-mode dc-dc converters. As the name implies, the power transfer is based on switching action, in which energy is periodically stored into magnetic or electric fields (i.e., in inductors and capacitors) and then released to load by means of controllable or passive semiconductor switches (i.e., transistors and diodes). By using switched-mode conversion, it is possible to obtain very high conversion efficiencies because in principle, only the required amount of power demanded by the system load is taken from the corresponding system source. Ideally, this would imply a lossless conversion (Mohan et al., 2003). However, various loss mechanisms reduce the efficiency, and typically switched-mode converters obtain conversion efficiencies between 80 to 98 percent, depending e.g. on conversion type and power level.

An alternative method to obtain dc-dc conversion is to utilize linear regulators. Linear regulators do not contain switching elements, instead, the operating principle is based on dissipating the excess power not required by the load into heat. In other words, linear regulators operate as controllable resistors either in series with a voltage source (series regulator) or in parallel with a current source (shunt regulator) (Fig. 1.8). Due to absence

of switching action, linear regulators are able to provide power transfer only from higher to lower voltage level or from higher to lower current level (i.e., $U_L \leq U_s$ and $I_L \leq I_s$). Inherent benefits of linear regulators are simplicity of design due to operation principle and reduced amount of electrical noise compared to switched-mode converter. For these reasons, linear regulators are still used in applications requiring low-noise power supplies, such as precision measurement systems or high-fidelity audio systems.

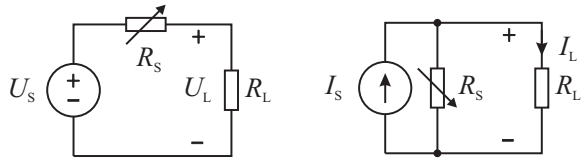

(a) Series regulator **(b)** Shunt regulator

Fig. 1.8. Linear regulator types.

Typical PV systems comprise a number of PV modules in a series configuration (string) (Bergveld et al., 2011; Liu et al., 2011). The final stage in the power conversion chain is the grid-connected inverter, which enables power transfer from a dc source into an ac load, operating under similar switching action with that of dc-dc converters. In order to feed undistorted current into the ac grid as dictated by the grid regulation codes (Kjaer et al., 2005), the conventional VSI-type[2] inverter requires an input voltage higher than the peak value of the grid voltage. For an inverter connected to a 230-V single-phase grid the required input voltage is typically 350 V, whereas for three-phase inverters connected to 400-V grid the input voltage has to be 700 V. This constraint of required input voltage level set by the inverter can be solved either by connecting a sufficient amount of PV modules into a string or by utilizing dc-dc converters. Four main methods to realize high-power PV systems are presented in Fig. 1.9: (a) The string inverter with a single PV string, (b) the central inverter with more than one PV strings, (c) a two-stage conversion with a dc-dc converter connected to a string and (d) modular system with module-level dc-dc conversion. (Kjaer et al., 2005; Myrzik and Calais, 2003).

In systems illustrated by Figs. 1.9a and 1.9b, there may not be need for an additional dc-dc converter, because the MPP voltage generated by the string can reach sufficient level under nominal operating conditions. These kind of systems are commonly used in high-power PV power plants due to lowest number of power conversion stages, reducing power losses caused by multi-stage conversion. However, large number of PV modules are required, resulting in large variation of the MPP voltage caused by environmental conditions. The design of the inverter is, therefore, more difficult because the power stage has to be designed to endure large variation of input voltage while maintaining high operational efficiency. It should be noted that systems like these are unable to

[2]Voltage source inverter, an inverter supplied by a voltage-type source

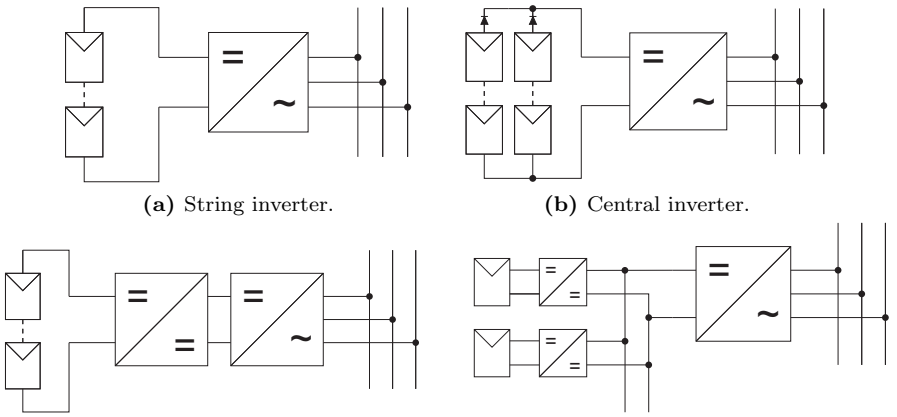

(a) String inverter.

(b) Central inverter.

(c) String inverter with two-stage conversion.

(d) Modular system.

Fig. 1.9. Four main PV system configurations.

extract maximum power if the voltage of the global MPP falls below the minimum required input voltage. It is also evident that in a string configuration, it is impossible to control each individual module into MPP under partial shading conditions: Due to non-uniform irradiance distribution, the modules have different MPP currents, but the string configuration forces each module to carry equal current. Therefore, some modules are forced to operate at an undesired operating point. (Imhoff et al., 2008; Kjaer et al., 2005; Liu et al., 2011)

To enable power extraction from lower voltages, dc-dc converter with voltage step-up capability can be implemented between a string of PV modules and the inverter in a so-called two-stage configuration (Fig. 1.9c). With this kind of arrangement, the maximum voltage imposed on the inverter (i.e., the open-circuit voltage of the string) is reduced, which eases the design requirements of the inverter and enables the use of switching devices with lower voltage rating. In general, the lower the voltage rating of a semiconductor switch, the better the operating characteristics, yielding increased efficiency. Moreover, a shorter PV string more likely operates under uniform irradiance, improving the energy yield, according to Mäki and Valkealahti (2012).

In order to extract the maximum available power out of each individual PV module within the system, a concept of converter-per-module has been presented and studied extensively (Bergveld et al., 2011; Kim and Krein, 2010; Li and Wolfs, 2008; Walker and Sernia, 2004). This concept, known also as distributed maximum power point tracking (DMPPT), is intended to decouple the operation of individual modules from each other, so that the system would be able to generate maximum instantaneous power regardless of environmental conditions at each module. These DMPPT systems can either be realized

using dc-dc converters, which are connected to a common dc bus (Kim et al., 2010; Liang et al., 2011; Roman et al., 2008) or with low-power module-integrated inverters (Deline et al., 2011; Kjaer et al., 2005; Wills et al., 1996).

Although a vast majority of practical and experimental systems are designed to be connected to a PV module, there are some approaches in which a PV module is split into sub-modules for power extraction. The principle in these solutions is to remove the bypass diodes and implement several low-power converters per each module (Burger et al., 2010; Dhople et al., 2010). As previously discussed, the effect of partial shading is further minimized as the remaining sub-modules have only a single MPP, thus making it easier to design the interfacing converter.

1.3.1 Maximum Power Point Tracking

As previously discussed, the location of the global MPP of a PV module on the I-V curve can vary significantly during the day due to environmental conditions and partial shading. Therefore, it is evident that the actual location of the global MPP (i.e., the values of corresponding module current and voltage) cannot be known exactly without direct measurement. Research around algorithms and methods to find the location of the MPP and to correctly drive the operating point to the MPP has been performed for decades, starting right from the early practical applications in space power systems (Capel et al., 1983; Glass, 1977). There are two main approaches in maximizing the produced energy: i) electrical maximum power point tracking and ii) solar tracking. Applying both methods simultaneously would ultimately maximize the energy production.

Solar tracking is based on tracking the path of the sun on the sky during the day and adjusting the direction of the module accordingly (Armstrong and Hurley, 2005). By changing the direction of the module, the conditions for maximum power generation can be ensured as the normal of the module surface is maintained towards the sun, i.e., the angle of incidence (Θ) at which the incoming irradiation arrives is maintained at zero. However, this method itself only aims to maximize the incoming irradiation on the module and, as such, does not actually track the electrical MPP of the module. Nevertheless, significant improvement in the generated energy during a day can be achieved, as presented by Armstrong and Hurley (2005): Actual measurements performed in Galway, Ireland and in Rome, Italy showed that during a summer day, solar tracking yielded 19 % more energy in Rome and approximately 30 % in Galway. Respectively, the increase during a winter day was approximately 55 % in Rome and 100 % in Galway. Despite the benefits, large-scale PV systems are typically not equipped with solar trackers due to increased installation and maintenance cost as well as increased demand for space due to moving modules.

Electrical maximum power point tracking (MPPT), however, is widely utilized and

the research around different algorithms is active (Esram and Chapman, 2007; Jain and Agarwal, 2007; Tsao et al., 2009). The fundamental operation is rather simple: To find the electrical operating point, i.e., the voltage and the current, at which the PV module generates maximum power. Most of the proposed MPPT algorithms and methods aim to maximize the output power of the module, although concepts have been presented (e.g., by Shmilovitz (2005)), where the power delivered to the system load by the interfacing converter is maximized. However, for most practical PV interfacing systems the module output power and the load power are maximized at the same operating point, because the efficiency of the interfacing systems is typically almost constant at the operating power levels of interest.

A convenient way to perform MPPT for a PV module is to utilize a dc-dc converter between the module and the system load. For grid-connected systems the load equals the input port of an inverter and, thus, by proper selection of the dc-dc converter type, the power transfer can be realized simultaneously. A number of different algorithms have been presented, which can be categorized into methods in which i) the PV module power or ii) either the module current or voltage is used as the source of information. Of these, the most widely utilized methods are presented briefly here, although the design and implementation of MPP tracking falls out of the actual scope of this thesis. Under nominal irradiation there is a single MPP, whose location can be approximated on the basis of the open-circuit voltage or the short-circuit current. *Fractional open-circuit voltage* method aims to locate the MPP by assuming linear relationship between the open-circuit voltage and the MPP voltage (i.e., $U_{\mathrm{mpp}} = k_1 U_{\mathrm{oc}}$), whereas *fractional short-circuit current* method assumes similar relationship for the currents ($I_{\mathrm{mpp}} = k_2 I_{\mathrm{sc}}$). These methods perform sufficiently well as long as there is only a single MPP. However, as soon as multiple MPPs emerge, the global MPP may not be found. (Esram and Chapman, 2007; Jain and Agarwal, 2007)

Hill climbing and *perturb & observe* methods operate under principle of performing periodic perturbation to the operating point and examining the difference in the produced power. By comparing the power in consecutive operation points, the direction towards MPP can be found. These methods, however, are criticized to fail under rapidly changing environmental conditions (Esram and Chapman, 2007) and, furthermore, they are only able to find a local MPP (Patel and Argawal, 2008). A similar method known as *incremental conductance* introduces, respectively, a periodic perturbation and examines the change in the PV module conductance, i.e., $\Delta i_{\mathrm{pv}}/\Delta u_{\mathrm{pv}}$, which equals zero at MPP. However, the global MPP cannot be guaranteed to be found. The only way to locate the global MPP regardless of the operating conditions is to use *I-V curve sweep* method to record the entire current-voltage curve and to extract the MPP out of the measured data. (Esram and Chapman, 2007; Jain and Agarwal, 2007; Shmilovitz, 2005)

1.4 Structure of the Thesis

The first chapter of this thesis provides introduction to the scope of the thesis by presenting the background for DMPPT systems and PV electricity systems in general. The nature of a PV cell and the PV module are discussed, including the limitations and practical behavior of systems comprising PV generators. Additionally, this thesis contains four other chapters, briefly summarized as follows:

The modeling tools and methods for analyzing the behavior of dc-dc converters in PV applications are discussed in Chapter 2. The general dc-dc conversion schemes are presented briefly and clear difference between them are pointed out. Moreover, the dynamic models for investigated converter structures are presented with predictions based on the analytical findings. It is also shown that in the field, some fundamental aspects in analyzing PV generator and the distributed converter systems are not completely understood, resulting in misinterpretations and false conclusions.

Chapter 3 discusses the distributed MPP-tracking scheme more in detail. The different system configurations that are either implemented in practical systems or presented in publications are covered, paying attention to the claimed operational properties and the overall feasibilities. Chapter 3 gives the reader a thorough review on DMPPT systems and presents also the interfacing constraints that are crucial fundamental laws dictating the behavior of interfacing converters. It is shown that contrary to general assumptions, the parallel configuration of dc-dc converters performs notably well, and may actually be more beneficial than the series configuration.

The practical verification of the claimed issues with the actual prototypes are introduced in Chapter 4, including description of the measurement system and the essential equipment used during the measurements. The importance of utilizing proper emulating devices is clarified with practical examples, further supporting the need for decent approach in modeling the PV generator itself. Chapter 4 also presents a new dc-dc converter topology, which was invented by the author during the research process. Finally, the conclusions are drawn in Chapter 5, summarizing the main claims. In addition, issues for future research are discussed.

1.5 Objectives and Scientific Contribution

This thesis discusses the characteristics and operation of dc-dc converters implemented in distributed photovoltaic systems. The two concepts in implementing distributed systems, the series and the parallel configuration, are given a thorough review and the most important properties are discussed. By analyzing the published research results, it can be concluded that complete understanding on the nature of PV electricity systems has not been reached yet. Therefore, the interfacing constraints dictating the operation of

dc-dc converters as well as dc-ac inverters in PV systems are classified and presented with practical examples.

In addition, it is shown that in order to reach correct conclusions and correct interpretation on the system under analysis, the true nature of the system has to be carefully considered. Among the issues to be considered is the nature of the PV generator itself. The published results reveal that the PV generator has to be modeled and emulated properly to obtain correct operation. It is shown that the static operation of an emulating electrical source is not sufficient, but also the dynamic operation has to accurately describe an actual PV generator. The voltage-fed systems and properties of voltage sources can be seen to dominate in the field of power electronics, although it has been proved that concepts that apply for voltage sources cannot be applied as such for other types of sources. Therefore, this thesis serves as a set of justified claims that are meant to evoke new ideas and improve understanding of PV systems in general.

The main scientific contribution of this thesis can be summarized as follows:

- It is shown that parallel configuration of dc-dc interfacing converters provides good performance, contrary to what was claimed
- The interfacing constrains affecting the implementation of dc-dc converters in distributed photovoltaic applications are explicitly defined
- Explicit system models for series and parallel-connected converters are given, revealing the existence of cross-couplings between series-connected converters
- The operational anomalies observed in the system of series-connected dc-dc converters are explained and shown to originate from the cross-couplings
- It is shown that under input-voltage control, the cross-coupling effects vanish due to high low-frequency gain of the control loop
- A patented interfacing converter structure, the current-fed quadratic full-bridge buck converter is introduced with extensive dynamic and static characterization, revealing the benefits: High efficiency, absence of control anomalies and capability to operate under high conversion ratio
- It is shown that an electronic emulator has to contain both static and dynamic characteristics resembling an actual PV generator to yield correct system performance

1.6 Related Publications and Author's Contribution

This thesis is related to the following publications, where the author's contribution is as follows: The publications [R1] - [R5] and [R10] are mainly contributed by the author, in publications [R6] - [R9] the author participated in the practical experiments.

[R1] Huusari, J. and Suntio, T. 'Dynamic properties of current-fed quadratic full-bridge buck converter for distributed photovoltaic MPP-tracking systems', in *IEEE Trans. Power Electron.*, vol. 27, no. 11, pp. 4681-4689, 2012.

[R2] Huusari, J. and Suntio, T. 'Current-fed quadratic full-bridge converter for PV systems interfacing: Static operation', *IEEE EPE 2011, Birmingham, UK*, pp.1-10, 2011.

[R3] Huusari, J. and Suntio, T. 'Current-fed quadratic full-bridge buck converter for PV systems interfacing: Dynamic characterization', *IEEE ECCE 2011, Phoenix, USA*, pp. 487-494, 2011.

[R4] Huusari, J. and Suntio, T. 'Interfacing constraints of distributed maximum power point tracking converters in photovoltaic applications', in *IEEE EPE-PEMC 2012, Novi Sad, Serbia* (in press).

[R5] Huusari, J. and Suntio, T. 'Distributed MPP-tracking: cross-coupling effects in series and parallel connected DC/DC converters', in *EU-PVSEC 2012, Frankfurt, Germany* (in press).

[R6] Leppäaho, J., Huusari, J., Nousiainen, L., Puukko, J. and Suntio, T. 'Dynamic properties and stability assessment of current-fed converters in photovoltaic applications', in *IEEJ Trans. Ind. Appl.*, vol. 131, no. 8, pp. 976-984, 2011.

[R7] Suntio, T., Leppäaho, J. and Huusari, J., 'Issues on solar-generator-interfacing with current-fed MPP-Tracking converters', in *IEEE Trans. Power Electron.*, vol. 25, no. 9, pp. 2409- 2419, 2010.

[R8] Suntio, T., Huusari, J. and Leppäaho, J. 'Issues on solar-generator interfacing with voltage-fed MPP-tracking converters', *European Power Electronics and Drives Journal*, vol. 20, no. 3, pp. 40-47, Sept. 2010.

[R9] Puukko, J., Nousiainen, L., Mäki, A., Huusari, J., Messo, T. and Suntio, T. 'Photovoltaic generator as an input source for power electronic converters', in *IEEE EPE-PEMC 2012, Novi Sad, Serbia* (in press).

[R10] Huusari, J. and Suntio, T. 'Transformer-isolated switching converter', February 22, 2010, US 2012044717, EP 2421138, CN 102377346.

2 MODELING

This chapter presents the modeling methods used in the analysis of the converters and systems in this thesis. The concept of state-space averaging is discussed with application to modeling switched-mode converters. The inclusion of non-idealities of the source and load is discussed in detail, with connection to the impedance-based stability assessment of switched-mode converters. In addition, the models for the converter structures and the claims based on the analysis are presented.

2.1 Introduction

In order to correctly analyze a switched-mode dc-dc converter in an arbitrary application, the applicable conversion scheme must first be selected. Traditionally, a vast majority of switched-mode converters have had a constant voltage as the input source, such as the utility grid, a battery or a dc link and had their output voltage controlled by means of feedback loop. Moreover, if the output voltage is to be controlled, the load cannot be a constant voltage as the control engineering principles state that only the output variables can be controlled (Dorf and Bishop, 2001). This is a natural constraint, as it would be meaningless to try to control a parameter that is already controlled by another mechanism. Therefore, a dc-dc converter supplied by a constant voltage source with a feedback loop from the output voltage is to be analyzed as a network that allows control of the input current and the output voltage.

According to this principle, there are four conversion schemes that can be defined as shown in Fig. 2.1: The G-parameter scheme, the H-parameter scheme, the Y-parameter scheme and the Z-parameter scheme. Each conversion scheme is represented by a specific network model, which is an extension of a general two-port model by addition of a third port, representing the control signal. A thorough overview of different conversion schemes is presented by Leppäaho (2011).

As previously explained, the PV generator has to be treated as a current source with non-linear characteristics. This implies that the corresponding network model has a constant current source at the input terminal, limiting the applicable models to H-parameter and Z-parameter schemes. Conventionally, dc-dc converters that are connected directly at the PV generator terminals have some kind of constant voltage at the output terminal. For example, in residential small-scale applications this would mean a battery

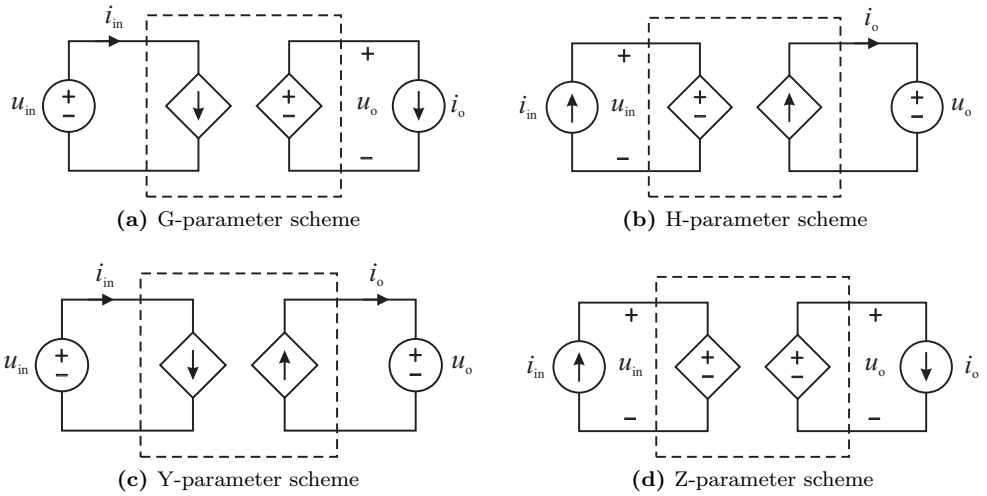

(a) G-parameter scheme **(b)** H-parameter scheme

(c) Y-parameter scheme **(d)** Z-parameter scheme

Fig. 2.1. dc-dc conversion schemes.

bank and in systems with higher power output the load would be a dc link, whose voltage is controlled by another network. These system configurations correspond to H-parameter network scheme. Photovoltaic applications having a current sink at the output terminal, i.e., the Z-parameter scheme, are rarely discussed (with a few exceptions, such as Linares et al. (2009)).

Current-Fed Converters

The naming convention for a network is crucial, as it gives direct insight into the source, load and controllable variables. As indicated in Fig. 2.1, when a certain network is called a current-fed system, one immediately assumes certain properties for the network, such as the ability to control the input voltage. A common misconception among the practicing engineers and researchers in the field is to name a voltage-fed converter with a series inductor at the input terminal as a current-fed or a current-sourced converter (Fig. 2.2a) leading to improper conclusions and misunderstandings (Averberg et al., 2008; Liu and Lee, 1988; Mohr and Fuchs, 2006; Song and Lehman, 2007; Weaver and Krein, 2007). Although at high frequencies or momentarily at low frequencies the structure in Fig. 2.2a mimics a current source, the equality must also hold at dc for the naming convention and static operation to be justified. According to Fig. 2.2a, this requirement does not hold, because the inductor is a short circuit at dc.

Referring to Fig. 2.2a, if the series connection equals a current source, then one should be able to control the terminal voltage u_T to an arbitrary value. It is obvious that by controlling u_T to a value different than u_S, a constant voltage difference is applied on

the inductor terminals, resulting in constant derivative in the inductor current which, in turn, leads to infinitely increasing or decreasing inductor current.

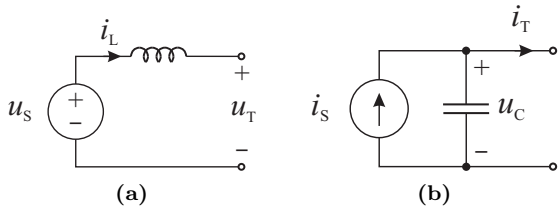

Fig. 2.2. (a) A voltage-fed and (b) a current-fed input port.

Similar misconception usually encountered in PV applications is to assume the PV generator with a parallel-connected capacitor (Fig. 2.2b) to equal a constant voltage source. According to the same arguments as above, the capacitor is an open circuit at dc and, therefore, the parallel connection retains the properties of the original source (i.e., the current source) at dc. Therefore, if the terminal current i_T is controlled to a value different to i_S, a constant derivative in the capacitor voltage results, leading to increase or decrease in the capacitor voltage. Substituting a parallel connection of a current source and a capacitor with a voltage source has a profound effect on the operation of the converter connected to it. This is explained later in detail, when the effect of the source impedance is included in the dynamic model of the system.

2.2 Dynamic Modeling of DC-DC Converters

A switched-mode dc-dc converter is inherently non-linear due to its variable-structure nature caused by switching actions. In principle, the non-linearity means that a change in one operating parameter (e.g., in the input voltage) does not yield directly proportional change in some other operating parameter (Middlebrook, 1988). The non-linearity of the semi-conductive components, transistors and diodes, is typically taken into account by replacing the components with operating-point-specific linear circuit elements.

Depending on the state of the switches in the circuit (i.e., either they are conducting or non-conducting), the original circuit structure goes through different equivalent switching stages (sub-circuits). The sub-circuits are active for a certain part t_i of the switching period T_s. The ratio of the main active part t_{on} to the switching period (the duty cycle, $d = t_{on}/T_s$) is used to define the conversion ratio of the converter ($m(d)$), i.e., the relationship between the input and output voltage, for example. The non-linearity caused by switching action means, therefore, that a certain change in the duty cycle may not yield directly proportional change in the conversion ratio. The actual definition for t_{on} depends on the converter under study, as converters may have different number of sub-circuits.

2.2.1 State-Space Averaging

In order to conveniently model and analyze the operation of a switched-mode converter, a linear model for the converter is required. Conventionally, the state-space averaging approach (Middlebrook and Ćuk, 1976) is used to obtain a linear small-signal model describing the circuit operation in frequency domain. Frequency-domain analysis is mandatory to correctly predict the operation of the circuit in time domain, i.e., to guarantee stable and controlled power processing as well as to predict the circuit response to changes in operating conditions. Moreover, the control of switched-mode converter can be reliably designed and verified only with frequency-domain methods.

In state-space averaging, the sub-circuits are analyzed separately and corresponding state-space equations are developed according to well-known Kirchhoff's circuit laws. In a state-space model, the system *output* variables and the derivatives of the system *state* variables are given as a function of the *input* and the state variables. An averaged state-space model is obtained, when the equations describing the sub-circuits are averaged over one switching period, according to the durations that each sub-circuit is active. The averaged model, therefore, presents the averaged, time-invariant behavior of the circuit but is non-linear by its nature (Maksimović et al., 2001). A linear model is finally obtained, when the averaged equations are linearized around a specific operating point, i.e., partial derivatives of each variable are developed from the state equations.

Regarding switched-mode dc-dc converters, there are three input variables with defined values and two output variables whose values depend on the input variables. A general block model for a system describing a dc-dc converter is given in Fig. 2.3:

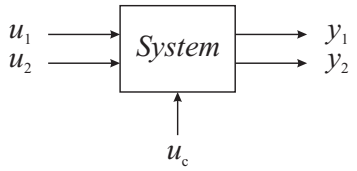

Fig. 2.3. A general input-output model.

The input variables are u_1, u_2 and u_c depicting the input source, the output load and the control variable. Respectively, the output variables y_1 and y_2 depict the electrical dual pairs of u_1 and u_2. For example, if u_1 is a voltage source, then y_1 is the current of that source. The state variables can be selected arbitrarily, provided that they are linearly independent. Typically, the inductor currents i_L and capacitor voltages u_C are selected as state variables. The amount and type of the state variables are defined by the actual structure of the system.

When the averaged state-space consisting of time-domain differential equations is linearized around a certain operating point, the resulting linearized time-domain state-

space, i.e., the small-signal model (Middlebrook, 1988) can be expressed as in (2.1), where $\hat{\mathbf{x}}(t)$, $\hat{\mathbf{u}}(t)$ and $\hat{\mathbf{y}}(t)$ are vectors containing the state variables, input variables and output variables, respectively. The matrices $\mathbf{A}$, $\mathbf{B}$, $\mathbf{C}$ and $\mathbf{D}$ contain the effects of the parasitic elements within the circuit, such as parasitic resistances, as well as the effects of the inductances and capacitances in the system. Additionally, depending on the converter topology, these matrices contain typically some average values of the converter terminal variables, such as the average output or input voltage. Thus, these matrices effectively contain information on the operating point.

$$\begin{aligned} \frac{\mathrm{d}}{\mathrm{d}t}\hat{\mathbf{x}}(t) &= \mathbf{A}\hat{\mathbf{x}}(t) + \mathbf{B}\hat{\mathbf{u}}(t) \\ \hat{\mathbf{y}}(t) &= \mathbf{C}\hat{\mathbf{x}}(t) + \mathbf{D}\hat{\mathbf{u}}(t). \end{aligned} \tag{2.1}$$

To obtain the frequency-domain small-signal model, Laplace transformation is applied to (2.1), yielding the following frequency-domain equations, where s denotes the Laplace variable:

$$\begin{aligned} s\mathbf{X}(s) &= \mathbf{A}\mathbf{X}(s) + \mathbf{B}\mathbf{U}(s) \\ \mathbf{Y}(s) &= \mathbf{C}\mathbf{X}(s) + \mathbf{D}\mathbf{U}(s). \end{aligned} \tag{2.2}$$

The output variables $\mathbf{Y}(s)$ can be solved from (2.2), yielding (2.3)

$$\mathbf{Y}(s) = [\mathbf{C}(s\mathbf{I} - \mathbf{A})^{-1}\mathbf{B} + \mathbf{D}]\mathbf{U}(s) = \mathbf{G}(s)\mathbf{U}(s). \tag{2.3}$$

The matrix $\mathbf{G}(s)$ contains six transfer functions, describing the mapping between input variables ($\mathbf{U} = [\hat{u}_1 \;\; \hat{u}_2 \;\; \hat{u}_\mathrm{c}]^\mathrm{T}$) and output variables ($\mathbf{Y} = [\hat{y}_1 \;\; \hat{y}_2]^\mathrm{T}$). Using matrix notation, the mapping can be expressed as follows

$$\begin{bmatrix} \hat{y}_1 \\ \hat{y}_2 \end{bmatrix} = \begin{bmatrix} G_{11} & T_\mathrm{oi} & G_\mathrm{ci} \\ G_\mathrm{io} & -G_{22} & G_\mathrm{co} \end{bmatrix} \begin{bmatrix} \hat{u}_1 \\ \hat{u}_2 \\ \hat{u}_\mathrm{c} \end{bmatrix}. \tag{2.4}$$

These transfer functions are typically interpreted as follows: The ohmic characteristics of input and output terminals are described by transfer functions G_{11} and G_{22}. The reverse (i.e., output-to-input) transfer function T_oi describes the effect caused by the input variable of the output terminal on the output variable of the input terminal. Respectively, the forward (i.e, input-to-output) transfer function G_io describes the effect caused by the input variable of the input terminal on the output variable of the output terminal. Finally, the interactions of the control variable to the output variables are described by G_ci and

G_{co}. These control transfer functions are of significant importance, as the control loops of a converter are designed based on them.

An important aspect to note is the sign of the transfer function G_{22}. The minus sign originates from the fact that the state-space equations are constructed according to the actual direction of power flow, i.e., the defined positive direction of currents coincide with the actual positive current. However, the transfer function G_{22} describes the ohmic characteristics of the converter output terminal, which is defined by assuming positive current flowing inwards at the output terminal. Therefore, a negative sign has to be added to the developed state-space representation to obtain correct results.

In this thesis, the H-parameter scheme (Fig. 2.1b) plays the most significant role, since it is used to describe an individual dc-dc converter in distributed PV system, as discussed in Chapter 3. Therefore, for convenience, the transfer function matrix $\mathbf{G}(s)$ and the actual transfer functions of the H-parameter scheme are presented in (2.5).

$$\begin{bmatrix} \hat{u}_{\mathrm{in}} \\ \hat{i}_{\mathrm{o}} \end{bmatrix} = \begin{bmatrix} Z_{\mathrm{in}} & T_{\mathrm{oi}} & G_{\mathrm{ci}} \\ G_{\mathrm{io}} & -Y_{\mathrm{o}} & G_{\mathrm{co}} \end{bmatrix} \begin{bmatrix} \hat{i}_{\mathrm{in}} \\ \hat{u}_{\mathrm{o}} \\ \hat{c} \end{bmatrix}. \tag{2.5}$$

Characteristic to H-parameter scheme is that a constant current source is connected to the input terminal and a constant-voltage-type load at the converter output terminal. Therefore, the input variables of the system are $\mathbf{U} = [\hat{i}_{\mathrm{in}} \;\; \hat{u}_{\mathrm{o}} \;\; \hat{c}]^{\mathrm{T}}$ and the output variables $\mathbf{Y} = [\hat{u}_{\mathrm{in}} \;\; \hat{i}_{\mathrm{o}}]^{\mathrm{T}}$, respectively. A network model for the H-parameter network is shown in Fig. 2.4, equaling (2.5):

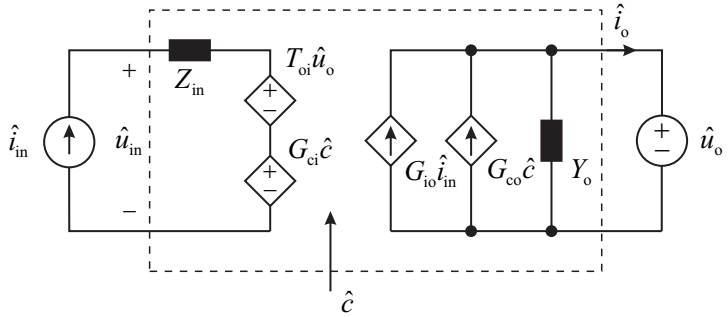

Fig. 2.4. An H-parameter network.

It should be noted that contrary to the conventional network model, the positive output current is now defined to flow out of the output terminal, to comply with presentations in (2.5) and (2.4).

2.2.2 Non-Ideal Source and Load

The non-idealities of source and load (i.e., the corresponding impedances) play a significant role in the behavior of a switched-mode converter. Therefore, in order to correctly model and predict the system operation, these effects have to be taken into account in the modeling. In the following, the method for including the source and load non-idealities is presented for the H-parameter scheme. Following the same procedure, similar analysis can be performed for any conversion scheme.

Simplified Non-Ideality Model

Referring to Fig. 2.4, the load non-idealities can be analyzed by introducing an arbitrary impedance Z_{L} in series with the voltage-type load, resulting in a network model shown in Fig. 2.5.

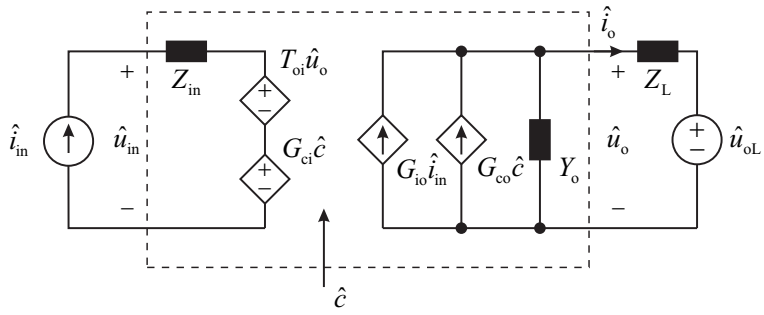

Fig. 2.5. An H-parameter network with non-ideal load.

The effect of load impedance can be found by computing $\hat{u}_{\mathrm{o}}$ from Fig. 2.5 and substituting $\hat{u}_{\mathrm{o}}$ in (2.5) with the obtained expression:

$$\hat{u}_{\mathrm{o}} = Z_{\mathrm{L}}\hat{i}_{\mathrm{o}} + \hat{u}_{\mathrm{oL}}. \tag{2.6}$$

The load-affected small-signal model, therefore, no longer has $\hat{u}_{\mathrm{o}}$ as an input variable, instead, it is replaced by the actual load voltage $\hat{u}_{\mathrm{oL}}$.

By computing the input and output dynamics (i.e., the expressions for input voltage and output current) from the network model in Fig. 2.5, the set of transfer functions shown in (2.7) results. The transfer functions are manipulated to contain the same denominator, which results in two special output admittances: The output admittance at short-circuited input terminal $Y_{\text{o-sci}}$ and the ideal output admittance $Y_{\text{o-}\infty}$.

$$\begin{bmatrix} \hat{u}_{\text{in}} \\ \hat{i}_{\text{o}} \end{bmatrix} = \begin{bmatrix} Z_{\text{in}} \dfrac{1+Z_{\text{L}}Y_{\text{o-sci}}}{1+Z_{\text{L}}Y_{\text{o}}} & T_{\text{oi}} \dfrac{1}{1+Z_{\text{L}}Y_{\text{o}}} & G_{\text{ci}} \dfrac{1+Z_{\text{L}}Y_{\text{o-}\infty}}{1+Z_{\text{L}}Y_{\text{o}}} \\ G_{\text{io}} \dfrac{1}{1+Z_{\text{L}}Y_{\text{o}}} & -Y_{\text{o}} \dfrac{1}{1+Z_{\text{L}}Y_{\text{o}}} & G_{\text{co}} \dfrac{1}{1+Z_{\text{L}}Y_{\text{o}}} \end{bmatrix} \begin{bmatrix} \hat{i}_{\text{in}} \\ \hat{u}_{\text{oL}} \\ \hat{c} \end{bmatrix}. \quad (2.7)$$

Respectively, the ideal small-signal model can be expanded to contain the effects of a non-ideal source, described by an arbitrary source admittance Y_{S}, yielding the network model shown in Fig. 2.6.

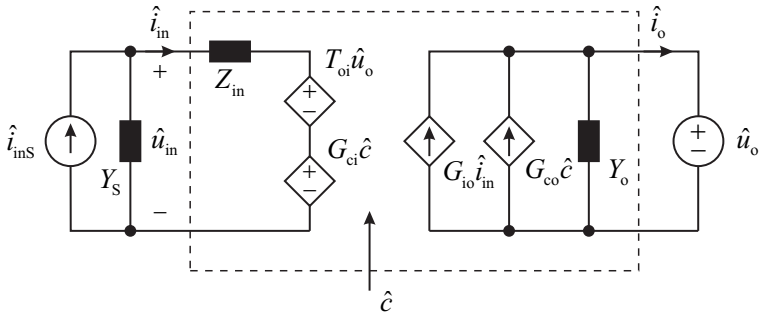

Fig. 2.6. An H-parameter network with non-ideal source.

The actual input current $\hat{i}_{\text{in}}$ is computed from Fig. 2.6 and substituted in (2.5) as follows:

$$\hat{i}_{\text{in}} = \hat{i}_{\text{inS}} - Y_{\text{S}}\hat{u}_{\text{in}}. \quad (2.8)$$

Thus, the input variable $\hat{i}_{\text{in}}$ is replaced by the current of the actual source i_{inS}.

The transfer functions describing the input and output dynamics of the source-affected H-parameter network can be presented as in (2.9). Again, the transfer functions are manipulated to share a common denominator, resulting in two additional special transfer functions: The input impedance at open-circuited output terminal $Z_{\text{in-oco}}$ and the ideal input impedance $Z_{\text{in-}\infty}$.

$$\begin{bmatrix} \hat{u}_{\text{in}} \\ \hat{i}_{\text{o}} \end{bmatrix} = \begin{bmatrix} Z_{\text{in}} \dfrac{1}{1+Z_{\text{in}}Y_{\text{S}}} & T_{\text{oi}} \dfrac{1}{1+Z_{\text{in}}Y_{\text{S}}} & G_{\text{ci}} \dfrac{1}{1+Z_{\text{in}}Y_{\text{S}}} \\ G_{\text{io}} \dfrac{1}{1+Z_{\text{in}}Y_{\text{S}}} & -Y_{\text{o}} \dfrac{1+Z_{\text{in-oco}}Y_{\text{S}}}{1+Z_{\text{in}}Y_{\text{S}}} & G_{\text{co}} \dfrac{1+Z_{\text{in-}\infty}Y_{\text{S}}}{1+Z_{\text{in}}Y_{\text{S}}} \end{bmatrix} \begin{bmatrix} \hat{i}_{\text{inS}} \\ \hat{u}_{\text{o}} \\ \hat{c} \end{bmatrix}. \quad (2.9)$$

The four special transfer functions in H-parameter conversion scheme, emerging from the inclusion of source and load non-idealities can be summarized as follows

$$Z_{\text{in-oco}} = Z_{\text{in}} + \frac{G_{\text{io}}T_{\text{oi}}}{Y_{\text{o}}} \qquad Y_{\text{o-sci}} = Z_{\text{in}} + \frac{G_{\text{io}}T_{\text{oi}}}{Y_{\text{o}}}$$
$$Z_{\text{in-}\infty} = Z_{\text{in}} - \frac{G_{\text{io}}G_{\text{ci}}}{G_{\text{co}}} \qquad Y_{\text{o-}\infty} = Z_{\text{in}} + \frac{G_{\text{io}}T_{\text{oi}}}{Y_{\text{o}}}. \tag{2.10}$$

The actual effect of the relevant special transfer functions regarding this thesis are discussed later in detail.

Complete Non-Ideality Model

The simplified models presented previously are sufficient, when only the impedance behavior of the source interface or the load interface is examined, or when the actual source terminals are inaccessible. For example, the output impedance of a laboratory voltage supply has to be modeled with a series connection of an ideal source and an impedance, because it is possible to examine only the behavior of this series connection, not the actual source.

However, if the converter has a filter network between its output terminal and the actual load, for example, the simplified model yields limited information. In this kind of configuration, the terminal of the actual load is accessible, thus enabling transfer functions related to the load terminal to be examined. Therefore, if the load and source effects are modeled as individual sub-systems according to Fig. 2.7, a complete picture of the system can be obtained. The block 'C' represents the switched-mode converter, 'S' the source subsystem and 'L' the load subsystem.

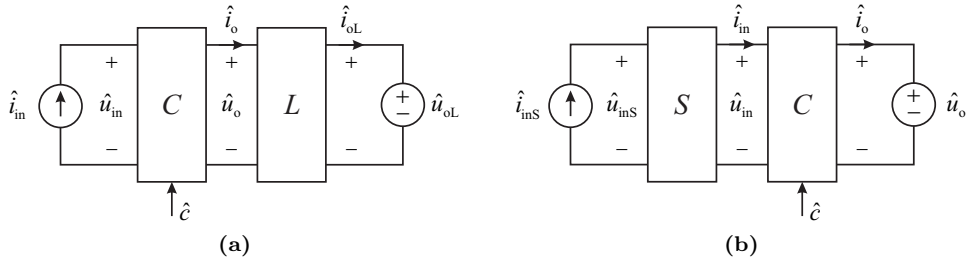

Fig. 2.7. (a) A load sub-system and (b) a source sub-system.

The inclusion of a non-ideal subsystem is most conveniently performed by forming separate mapping for the sub-system and combining it with the converter model. The mapping for non-ideal load and source can be, therefore, expressed as

$$\begin{bmatrix} \hat{u}_{\mathrm{inS}} \\ \hat{i}_{\mathrm{in}} \end{bmatrix} = \begin{bmatrix} Z_{\mathrm{inS}} & T_{\mathrm{oiS}} \\ G_{\mathrm{ioS}} & -Y_{\mathrm{oS}} \end{bmatrix} \begin{bmatrix} \hat{i}_{\mathrm{inS}} \\ \hat{u}_{\mathrm{in}} \end{bmatrix}, \quad \begin{bmatrix} \hat{u}_{\mathrm{o}} \\ \hat{i}_{\mathrm{oL}} \end{bmatrix} = \begin{bmatrix} Z_{\mathrm{inL}} & T_{\mathrm{oiL}} \\ G_{\mathrm{ioL}} & -Y_{\mathrm{oL}} \end{bmatrix} \begin{bmatrix} \hat{i}_{\mathrm{o}} \\ \hat{u}_{\mathrm{oL}} \end{bmatrix}. \tag{2.11}$$

The network model corresponding to the load sub-system shown in Fig. 2.7a can be presented as in Fig. 2.8, where the input variables are $\hat{i}_{\mathrm{in}}, \hat{u}_{\mathrm{oL}}$ and $\hat{c}$ as well as the output variables $\hat{u}_{\mathrm{in}}, \hat{u}_{\mathrm{o}}$ and $\hat{i}_{\mathrm{oL}}$, respectively.

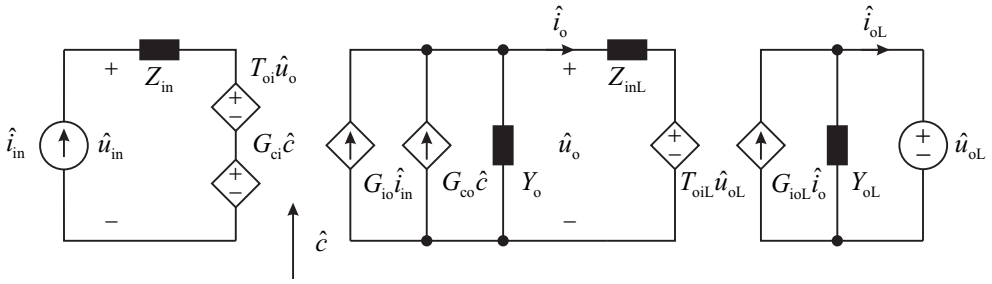

Fig. 2.8. An H-parameter network with complete non-ideal load.

For the source sub-system in Fig. 2.7b, the input variables are $\hat{i}_{\mathrm{inS}}, \hat{u}_{\mathrm{o}}$ and $\hat{c}$ as well as the output variables $\hat{u}_{\mathrm{inS}}, \hat{u}_{\mathrm{in}}$ and $\hat{i}_{\mathrm{o}}$.

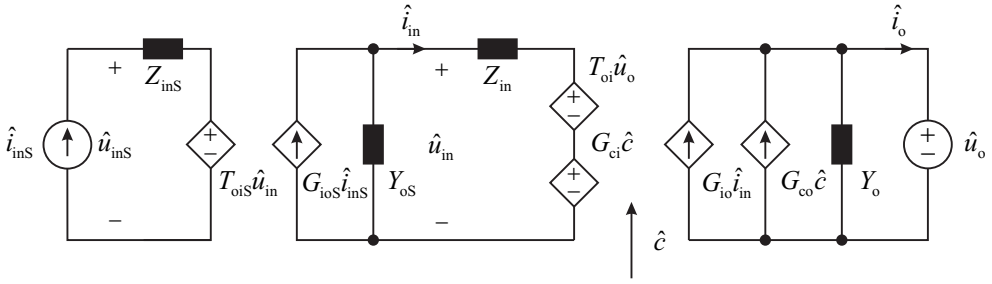

Fig. 2.9. An H-parameter network with complete non-ideal source.

When combined with the H-parameter mapping in (2.5), the transfer function matrices $\mathbf{G}_{\mathrm{L}}$ and $\mathbf{G}_{\mathrm{S}}$ comprising the mapping between input and output variables are obtained

$$\begin{bmatrix} \hat{u}_{\mathrm{inS}} \\ \hat{u}_{\mathrm{in}} \\ \hat{i}_{\mathrm{o}} \end{bmatrix} = \mathbf{G}_{\mathrm{S}} \begin{bmatrix} \hat{i}_{\mathrm{inS}} \\ \hat{u}_{\mathrm{o}} \\ \hat{c} \end{bmatrix}, \quad \begin{bmatrix} \hat{u}_{\mathrm{in}} \\ \hat{u}_{\mathrm{o}} \\ \hat{i}_{\mathrm{oL}} \end{bmatrix} = \mathbf{G}_{\mathrm{L}} \begin{bmatrix} \hat{i}_{\mathrm{in}} \\ \hat{u}_{\mathrm{oL}} \\ \hat{c} \end{bmatrix}, \tag{2.12}$$

where the complete load and source sub-system mappings are as follows:

$$\mathbf{G}_{\mathrm{S}} = \begin{bmatrix} Z_{\mathrm{inS}} \dfrac{1 + Z_{\mathrm{in}} Y_{\mathrm{oS\text{-}sci}}}{1 + Z_{\mathrm{in}} Y_{\mathrm{oS}}} & T_{\mathrm{oi}} \dfrac{T_{\mathrm{oiS}}}{1 + Z_{\mathrm{in}} Y_{\mathrm{oS}}} & G_{\mathrm{ci}} \dfrac{T_{\mathrm{oiS}}}{1 + Z_{\mathrm{in}} Y_{\mathrm{oS}}} \\ Z_{\mathrm{in}} \dfrac{G_{\mathrm{ioS}}}{1 + Z_{\mathrm{in}} Y_{\mathrm{oS}}} & T_{\mathrm{oi}} \dfrac{1}{1 + Z_{\mathrm{in}} Y_{\mathrm{oS}}} & G_{\mathrm{ci}} \dfrac{1}{1 + Z_{\mathrm{in}} Y_{\mathrm{oS}}} \\ G_{\mathrm{io}} \dfrac{G_{\mathrm{ioS}}}{1 + Z_{\mathrm{in}} Y_{\mathrm{oS}}} & -Y_{\mathrm{o}} \dfrac{1 + Z_{\mathrm{in\text{-}oco}} Y_{\mathrm{oS}}}{1 + Z_{\mathrm{in}} Y_{\mathrm{oS}}} & G_{\mathrm{co}} \dfrac{1 + Z_{\mathrm{in\text{-}}\infty} Y_{\mathrm{oS}}}{1 + Z_{\mathrm{in}} Y_{\mathrm{oS}}} \end{bmatrix}. \tag{2.13}$$

$$\mathbf{G}_{\mathrm{L}} = \begin{bmatrix} Z_{\mathrm{in}} \dfrac{1 + Z_{\mathrm{inL}} Y_{\mathrm{o\text{-}sci}}}{1 + Z_{\mathrm{inL}} Y_{\mathrm{o}}} & T_{\mathrm{oi}} \dfrac{T_{\mathrm{oiL}}}{1 + Z_{\mathrm{inL}} Y_{\mathrm{o}}} & G_{\mathrm{ci}} \dfrac{1 + Z_{\mathrm{inL}} Y_{\mathrm{o\text{-}}\infty}}{1 + Z_{\mathrm{inL}} Y_{\mathrm{o}}} \\ G_{\mathrm{io}} \dfrac{1}{1 + Z_{\mathrm{inL}} Y_{\mathrm{o}}} & -Y_{\mathrm{o}} \dfrac{T_{\mathrm{oiL}}}{1 + Z_{\mathrm{inL}} Y_{\mathrm{o}}} & G_{\mathrm{co}} \dfrac{1}{1 + Z_{\mathrm{inL}} Y_{\mathrm{o}}} \\ G_{\mathrm{io}} \dfrac{G_{\mathrm{ioL}}}{1 + Z_{\mathrm{inL}} Y_{\mathrm{o}}} & -Y_{\mathrm{oL}} \dfrac{1 + Z_{\mathrm{inL\text{-}oco}} Y_{\mathrm{o}}}{1 + Z_{\mathrm{inL}} Y_{\mathrm{o}}} & G_{\mathrm{co}} \dfrac{G_{\mathrm{ioL}}}{1 + Z_{\mathrm{inL}} Y_{\mathrm{o}}} \end{bmatrix}. \tag{2.14}$$

The special transfer functions from the interactions of these sub-systems can be summarized accordingly:

$$\begin{aligned} Z_{\mathrm{in\text{-}oco}} &= Z_{\mathrm{in}} + \frac{G_{\mathrm{io}} T_{\mathrm{oi}}}{Y_{\mathrm{o}}} & Y_{\mathrm{o\text{-}sci}} &= Y_{\mathrm{o}} + \frac{G_{\mathrm{io}} T_{\mathrm{oi}}}{Z_{\mathrm{in}}} \\ Z_{\mathrm{in\text{-}}\infty} &= Z_{\mathrm{in}} - \frac{G_{\mathrm{io}} G_{\mathrm{ci}}}{G_{\mathrm{co}}} & Y_{\mathrm{o\text{-}}\infty} &= Y_{\mathrm{o}} + \frac{G_{\mathrm{co}} T_{\mathrm{oi}}}{G_{\mathrm{ci}}} \\ Z_{\mathrm{inL\text{-}oco}} &= Z_{\mathrm{inL}} + \frac{G_{\mathrm{ioL}} T_{\mathrm{oiL}}}{Y_{\mathrm{oL}}} & Y_{\mathrm{oS\text{-}sci}} &= Y_{\mathrm{oS}} + \frac{G_{\mathrm{ioS}} T_{\mathrm{oiS}}}{Z_{\mathrm{inS}}}. \end{aligned} \tag{2.15}$$

2.2.3 The Concept of Minor-Loop Gain

The stability of interconnected systems, such as a switched-mode converter and accompanying EMI-filter (see Fig. 2.7b), can be inspected on the basis of the impedances at a

certain interface, by applying the Nyquist stability criterion (Dorf and Bishop, 2001), according to Middlebrook (1976). Middlebrook introduced the concept of *minor-loop gain* L_m, which he defined as the ratio of the source output impedance $Z_\mathrm{o,S}$ to the load input impedance $Z_\mathrm{in,L}$

$$L_\mathrm{m} = \frac{Z_\mathrm{o,S}}{Z_\mathrm{in,L}}. \tag{2.16}$$

The definition for 'source' and 'load' depend on the interface of interest. In the case of an input filter connected to the input terminal of a switched-mode converter, the minor-loop gain is formed as the ratio of the filter output impedance and the converter input impedance. By assuming that both of these subsystems are stable itself, the boundary condition for the system instability is the point, where the impedance ratio equals -1, i.e., the impedances have equal magnitude and a phase shift of 180 degrees:

$$\left|\frac{Z_\mathrm{o,S}}{Z_\mathrm{in,L}}\right| = 1 \wedge |\phi_\mathrm{S} - \phi_\mathrm{L}| = 180^\circ \rightarrow L_\mathrm{m} = \frac{|Z_\mathrm{o,S}|\angle\phi_\mathrm{S}}{|Z_\mathrm{in,L}|\angle\phi_\mathrm{L}} = \left|\frac{Z_\mathrm{o,S}}{Z_\mathrm{in,L}}\right| \angle(\phi_\mathrm{S} - \phi_\mathrm{L}) = -1. \tag{2.17}$$

The original minor-loop gain was defined by analyzing voltage-fed (VF) interface, in which power was transferred from a voltage source into a current sink (note the correspondence to conversion schemes and related interfaces in Fig. 2.1). Therefore, the minor-loop gain can also be presented as a product of the source output impedance and the sink input admittance, i.e., $L_\mathrm{m} = Z_\mathrm{o,S}Y_\mathrm{in,L}$. However, when analyzing current-fed (CF) systems, where power is transferred from current source into voltage-type load, the correct tool for inspecting the system stability is the *inverse minor-loop gain* (Sun, 2011; Suntio, Leppäaho, Huusari and Nousiainen, 2010), $L_\mathrm{m,inv} = Y_\mathrm{o,S}Z_\mathrm{in,L}$, visible e.g. in the denominators in (2.9).

According to Middlebrook (1976), a sufficient condition to ensure system stability is to require $|L_\mathrm{m,inv}| < 1$. If this requirement is met, the phase behavior is of no importance. At the boundary, however, the system is *marginally stable* and oscillates at the frequency at which the boundary condition (2.17) is valid. On the basis of practical measurements, it can be deduced that the system is unstable, if $|L_\mathrm{m,inv}| > 1$ and the phase difference exceeds 180 degrees, as will be shown in Chapter 4.

The concept of minor-loop gain is a valuable tool with which the system stability can be determined at an arbitrary interface, as long as the sub-systems separated by the interface are not dependent on each other. In addition to converter input-side interface, the same procedure can be applied on the output-side interface as well, yielding similar insight on system stability. In this thesis, the minor-loop gain is used especially to inspect the stability of the system at the interface between the PV module and the interfacing converter.

2.2.4 Dynamic Modeling Under Feedback Control

According to control engineering principles, processes can be categorized as either *open-loop* systems or *closed-loop* systems (Dorf and Bishop, 2001). An open-loop system does not contain feedback from a controllable output variable, such as the output voltage (Suntio, 2009). Therefore, a change in any of the input variable results in a permanent change in the system operating point, i.e., in all output variables. Thus, the system itself does not return to the original operating point after the change.

Closed-loop systems, on the other hand, have a feedback mechanism that aims to maintain the controlled variable at a value corresponding to the defined reference value. This is accomplished by applying negative feedback, which means that a disturbance in the value of the controlled variable causes the system to respond with an opposite change. A positive change in the controlled variable causes, therefore, the system to generate a negative change to the same variable.

As previously discussed, the control engineering principles state that only the system output variables can be controlled by means of a feedback loop. Thus, for switched-mode dc-dc converters, the conversion scheme (see Fig. 2.1) dictates the variables that can be controlled. For the H-parameter scheme these variables are the input voltage $\hat{u}_{\mathrm{in}}$ and the output current $\hat{i}_{\mathrm{o}}$. The input voltage control (i.e., the PV module voltage control) is easily accomplished due to the properties of the PV module, as discussed by Xiao, Dunford, Palmer and Capel (2007) and Xiao, Ozog and Dunford (2007). Further, it is shown by Suntio, Huusari and Leppäaho (2010) that PV terminal voltage control is the only viable scheme.

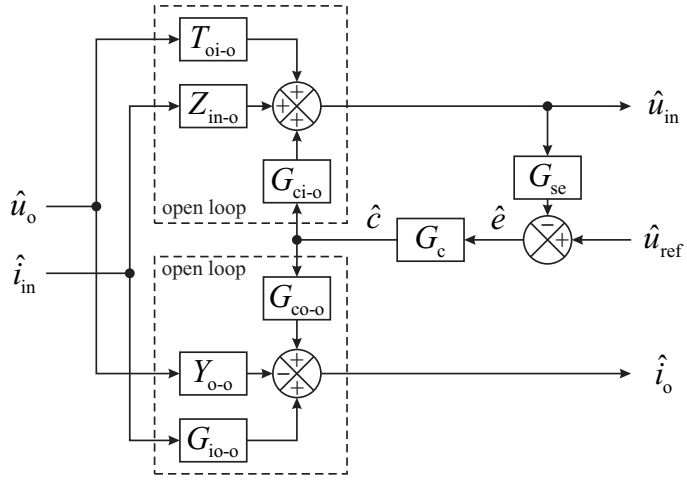

Fig. 2.10. Block diagram for input-voltage control in H-parameter scheme.

A control engineering block diagram representing input-voltage control in H-parameter scheme can be presented as in Fig. 2.10, depicting the addition of a feedback loop to the open-loop system (i.e., the dashed-line boxes). It should be noted that the transfer functions presented in (2.5) are valid both at open loop and closed loop. The subscript extensions '-o' and '-c' denote open-loop and closed-loop transfer functions, respectively.

According to Fig. 2.10, a negative feedback loop is formed to control the input voltage $\hat{u}_{\mathrm{in}}$: An error signal $\hat{e}$ is generated from the scaled input voltage $G_{\mathrm{se}}\hat{u}_{\mathrm{in}}$ and the reference voltage $\hat{u}_{\mathrm{ref}}$, which is fed to the control circuitry (lumped within G_{c}), yielding the control signal $\hat{c}$ for the converter. By denoting the gain of the feedback loop as

$$L_{\mathrm{v}} = G_{\mathrm{se}} G_{\mathrm{c}} G_{\mathrm{ci\text{-}o}}, \tag{2.18}$$

the closed-loop transfer functions can be presented as follows:

$$\begin{bmatrix} \hat{u}_{\mathrm{in}} \\ \hat{i}_{\mathrm{o}} \end{bmatrix} = \begin{bmatrix} \dfrac{Z_{\mathrm{in\text{-}o}}}{1+L_{\mathrm{v}}} & \dfrac{T_{\mathrm{oi\text{-}o}}}{1+L_{\mathrm{v}}} & \dfrac{1}{G_{\mathrm{se}}}\dfrac{L_{\mathrm{v}}}{1+L_{\mathrm{v}}} \\ \dfrac{G_{\mathrm{io\text{-}o}}+G_{\mathrm{io\text{-}\infty}}L_{\mathrm{v}}}{1+L_{\mathrm{v}}} & -\dfrac{Y_{\mathrm{o\text{-}o}}+Y_{\mathrm{o\text{-}\infty}}L_{\mathrm{v}}}{1+L_{\mathrm{v}}} & \dfrac{1}{G_{\mathrm{se}}}\dfrac{G_{\mathrm{co\text{-}o}}}{G_{\mathrm{ci\text{-}o}}}\dfrac{L_{\mathrm{v}}}{1+L_{\mathrm{v}}} \end{bmatrix} \begin{bmatrix} \hat{i}_{\mathrm{in}} \\ \hat{u}_{\mathrm{o}} \\ \hat{u}_{\mathrm{ref}} \end{bmatrix}. \tag{2.19}$$

The input-voltage feedback introduces an additional special transfer function, the ideal input-to-output transfer function $G_{\mathrm{io\text{-}\infty}}$. The meaning of $G_{\mathrm{io\text{-}\infty}}$ and $Y_{\mathrm{o\text{-}\infty}}$ can be seen from (2.19) by examining the magnitude of the loop gain L_{v}: Typically, the control loop is designed to have a high gain at low frequencies to eliminate the steady-state error, i.e., to obtain a value for the controlled variable exactly matching the reference value. This can be achieved by using a controller with an integrator, resulting in theoretically infinite gain at dc. Therefore, the value for the loop gain L_{v} is very high at low frequencies, indicating that the low-frequency values for $G_{\mathrm{io\text{-}c}}$ and $Y_{\mathrm{o\text{-}c}}$ equal $G_{\mathrm{io\text{-}\infty}}$ and $Y_{\mathrm{o\text{-}\infty}}$, respectively. At high frequencies, where the magnitude of the loop gain is low, the closed-loop transfer functions $Z_{\mathrm{in\text{-}c}}$, $T_{\mathrm{oi\text{-}c}}$, $G_{\mathrm{io\text{-}c}}$ and $Y_{\mathrm{o\text{-}c}}$ approach the corresponding open-loop transfer functions.

Moreover, by examining the denominators in (2.19) it can be seen that the loop gain acts to reduce the magnitude of the open-loop transfer functions related to converter input terminal. Therefore, for H-parameter scheme this indicates that the input impedance is low under closed-loop operation at low frequencies. According to basic circuit theory, an ideal voltage source has zero internal impedance, thus being able to provide equal voltage to a load having arbitrary impedance. Therefore, it can be stated that closed-loop operation at low frequencies shifts the H-parameter input terminal behavior towards an ideal voltage-type load.

2.3 Dynamic Modeling of the PV Generator

To correctly predict the system operation with a PV generator as the input source, the model of the PV generator itself has to be correctly formed. As explained previously, the PV generator is modeled with a photocurrent source, a parallel-connected diode and accompanying parasitic elements, yielding the characteristic current-voltage-curve, presented in Fig. 2.11.

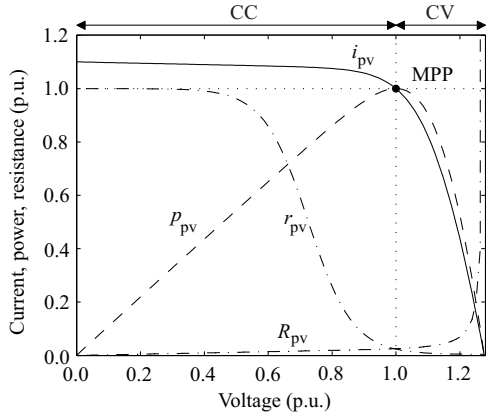

Fig. 2.11. Current-voltage characteristic.

The two additional resistances presented in Fig. 2.11 (dash-dotted lines) have significant effect on the behavior of interfacing devices. The PV cell static resistance (R_{pv}) is defined as the ratio between the PV cell current and voltage at given operating point, i.e., $R_{\mathrm{pv}} = U_{\mathrm{pv}}/I_{\mathrm{pv}}$. The operating point (i.e, R_{pv}) is determined by the interfacing converter that dictates the operating point. The dynamic resistance of the PV cell (r_{pv}) describes the low-frequency value of the PV cell output impedance and it is defined as $r_{\mathrm{pv}} = \Delta u_{\mathrm{pv}}/\Delta i_{\mathrm{pv}}$. By examining the equivalent circuit in Fig. 1.4, the PV cell output impedance $Z_{\mathrm{o,pv}}$ and its low-frequency value r_{pv} can be expressed as

$$Z_{\mathrm{o,pv}} = Z_{\mathrm{r,s}} + Z_{\mathrm{r,sh}} || Z_{\mathrm{c,pv}} || Z_{\mathrm{d}} \overset{f\to 0}{\to} r_{\mathrm{pv}} = r_{\mathrm{s}} + \frac{r_{\mathrm{sh}} r_{\mathrm{d}}}{r_{\mathrm{sh}} + r_{\mathrm{d}}}, \tag{2.20}$$

where r_{d} represents the dynamic resistance of the diode.

According to the Fig. 2.11 the resistances R_{pv} and r_{pv} are equal at MPP. The same result can be obtained by noting that at MPP, the derivative of the cell power in respect to the cell current is zero. In other words,

$$\frac{\mathrm{d}p_{\mathrm{pv}}}{\mathrm{d}i_{\mathrm{pv}}} = \frac{\mathrm{d}u_{\mathrm{pv}} i_{\mathrm{pv}}}{\mathrm{d}i_{\mathrm{pv}}} = U_{\mathrm{pv}} + I_{\mathrm{pv}} \frac{\Delta u_{\mathrm{pv}}}{\Delta i_{\mathrm{pv}}} = 0 \;\Leftrightarrow\; \frac{U_{\mathrm{pv}}}{I_{\mathrm{pv}}} = -\frac{\Delta u_{\mathrm{pv}}}{\Delta i_{\mathrm{pv}}}. \tag{2.21}$$

On the basis of (2.21) it would be obvious to state that the dynamic resistance of the PV cell is negative. Indeed, by developing tangent to the current-voltage curve shown in Fig. 2.11, the resulting slope representing the dynamic resistance is negative, as claimed etc. by Xiao, Dunford, Palmer and Capel (2007). There is, however, a fundamental flaw with this reasoning: The negative sign in front of the dynamic resistance in (2.21) originates from the fact that the dynamic resistance is defined by assuming positive current flowing into the terminal, although the actual current flows out of the terminal. By treating the dynamic resistance as the output impedance of the PV cell, in a similar way as the output impedance is defined, e.g., by Middlebrook (1976), it can be concluded that the dynamic resistance is positive. (Chenvidhya et al., 2006)

The importance of correct interpretation of the dynamic resistance is seen by examining the source-affected transfer functions, shown in (2.9) and (2.13), where the source-affected control-to-output transfer function is presented as

$$G_{\mathrm{co}}^{\mathrm{S}} = G_{\mathrm{co}} \frac{1 + Z_{\mathrm{in}\text{-}\infty} Y_{\mathrm{oS}}}{1 + Z_{\mathrm{in}} Y_{\mathrm{oS}}}, \tag{2.22}$$

with $Y_{\mathrm{oS}} = 1/Z_{\mathrm{oS}}$ depicting the PV generator output impedance. At low frequencies, the ideal input impedance of the interfacing converter approaches the negative static ratio between the input current and the input voltage (i.e., $-R_{\mathrm{pv}}$), while the PV generator output impedance approaches the dynamic resistance r_{pv}. Thus, the denominator of the control-to-output transfer function $G_{\mathrm{co,den}}^{S}$ becomes

$$G_{\mathrm{co,den}}^{\mathrm{S}} = 1 + Z_{\mathrm{in}\text{-}\infty} Y_{\mathrm{oS}} \overset{f \to 0}{\to} 1 - \frac{R_{\mathrm{pv}}}{r_{\mathrm{pv}}}. \tag{2.23}$$

According to Fig. 2.11, the static resistance is greater in magnitude than the dynamic resistance at voltages above MPP and smaller in magnitude at voltages below MPP. The change in the ratio occurring at the MPP changes the sign of the control-to-output transfer function, indicating that a phase shift of 180 degrees is experienced as the MPP is crossed over. If the interfacing converter has an output-side control loop (like a conventional output-voltage-controlled converter), the change in the phase behavior will compromise the stability of the control loop.

Furthermore, if the sign of the dynamic resistance has been defined to be negative, the previously described phase shift does not take place, therefore hiding the true nature of the PV generator. Measurement results presented in Chapter 4 prove that the dynamic resistance indeed is positive and output-side control cannot be safely applied throughout the PV generator operating curve.

2.4 Dynamic Models for Investigated Converter Structures

This section presents the dynamic models for the converter structures used in the experiments. For each converter, the schematic diagram of the power stage is presented briefly, and the formulation of state-space representation is explained in detail.

2.4.1 Current-Fed Quadratic Full-Bridge Buck Converter

The current-fed quadratic full-bridge converter (CFQFB) developed by the author was designed for parallel connection of module-integrated converters. By thorough analysis and discussion, the reader is provided with a complete methodology to analyze and design a parallel-connected interfacing dc-dc converter.

The power stage of CFQFB is shown in Fig. 2.12 with the polarities of the relevant currents and voltages shown in the figure (Huusari and Suntio, 2011a,b). The components within the schematic contain parasitic elements that are included in the analysis, but not shown in the figure for clarity.

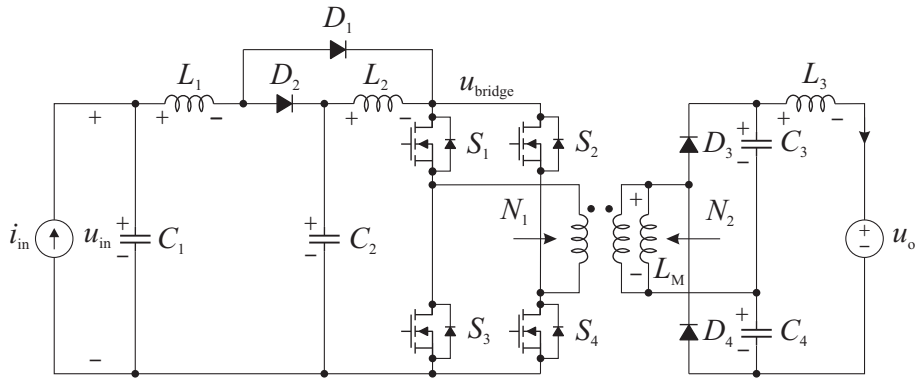

Fig. 2.12. Schematic diagram of the proposed converter.

The operation of the converter can be split into four different sub-circuits, corresponding to the switch operation as follows: During the on-time 1, the first pair of the primary switches (S_1, S_4) and the diodes D_2 and D_3 conduct, yielding the on-time 1 sub-circuit given in Fig. 2.13. During the off-times 1 and 2, all of the switches and the diode D_1 conduct, yielding the off-time sub-circuit given in Fig. 2.14. The off-time is followed by on-time 2, during which the sub-circuit (see Fig. 2.15) is otherwise identical to Fig. 2.13 except that the other switch pair (S_2, S_3) and the other secondary rectifier conduct. During the off times 1 and 2 the fluxes within the inductor L_1 ad L_2 cores increase due to applied positive voltage. During the on times, the stored energy is released and power is transmitted into the secondary side, also resembling the power transfer in a voltage-fed buck converter.

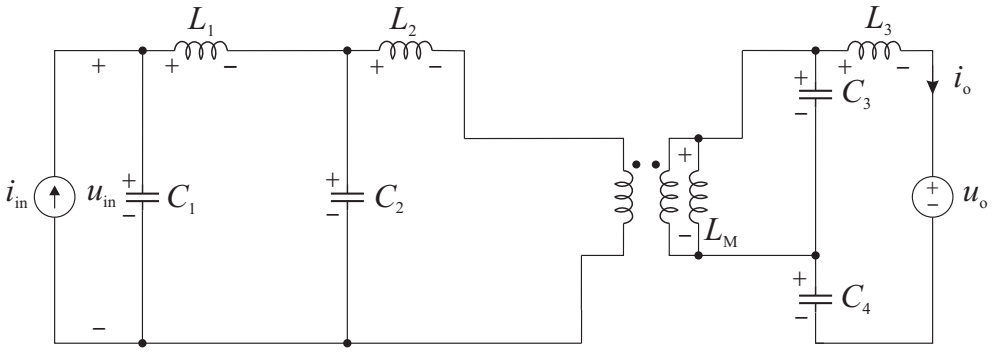

Fig. 2.13. On-time 1 sub-circuit.

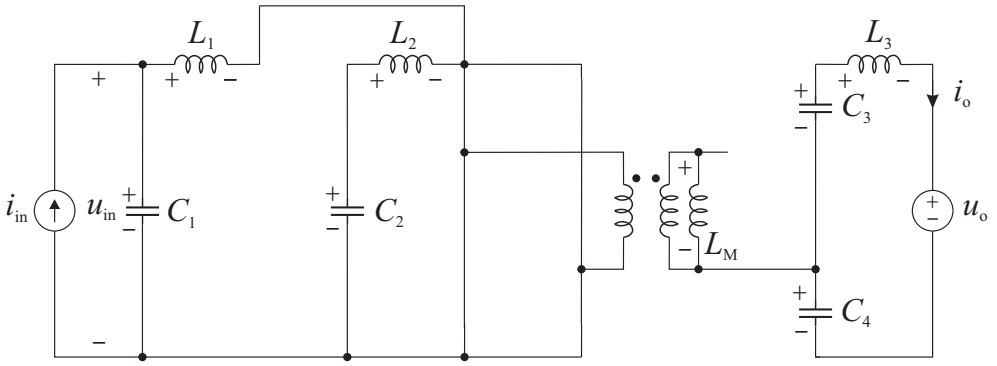

Fig. 2.14. Off-time 1 and 2 sub-circuit.

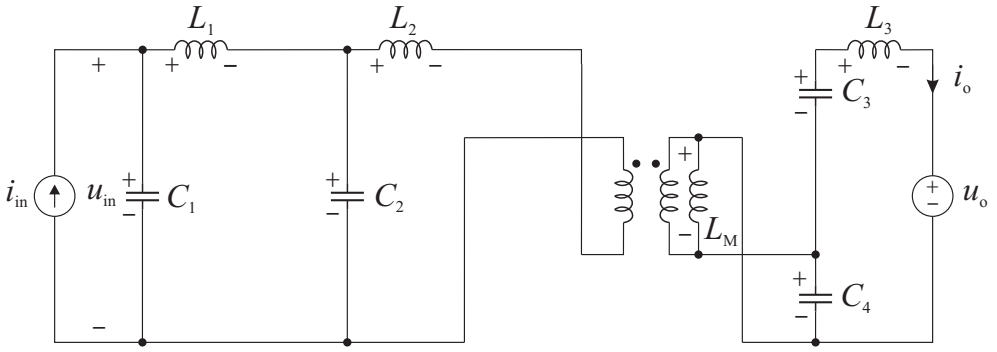

Fig. 2.15. On-time 2 sub-circuit.

In the applied analysis, the switching frequency f_s is defined by the duration of the four sub-cycles

$$t_{\mathrm{on},1} + t_{\mathrm{off},1} + t_{\mathrm{on},2} + t_{\mathrm{off},2} = T_\mathrm{s} = \frac{1}{f_\mathrm{s}}, \tag{2.24}$$

and the duty cycle d is defined by

$$d = d_1 + d_2 = \frac{t_{\mathrm{on},1}}{T_\mathrm{s}} + \frac{t_{\mathrm{on},2}}{T_\mathrm{s}} \qquad , \qquad d + d' = 1. \tag{2.25}$$

The dynamic modeling of the converter is based on the operational sub-circuits. By multiplying the on-time 1 equations with d_1, off-time equations with d_1' and d_2' and on-time 2 equations with d_2 and adding these together the averaged model is obtained (2.26). Assuming that the duration of the sub-cycles are pair-wise equal (i.e., $t_{\mathrm{on},1} = t_{\mathrm{on},2}$, $t_{\mathrm{off},1} = t_{\mathrm{off},2}$), the original four sub-circuits comprising the averaged equations can be effectively merged into two. Therefore, the elements that are effective only during one on-time sub-cycle have a coefficient of $d/2$.

$$\begin{aligned}
\frac{\mathrm{d}}{\mathrm{d}t}\langle i_{\mathrm{L}1}\rangle &= \frac{1}{L_1}\langle u_{\mathrm{C}1}\rangle - \frac{d}{L_1}\langle u_{\mathrm{C}2}\rangle \\
\frac{\mathrm{d}}{\mathrm{d}t}\langle i_{\mathrm{L}2}\rangle &= \frac{1}{L_2}\langle u_{\mathrm{C}2}\rangle - \frac{\frac{nd}{2}}{L_2}\langle u_{\mathrm{C}3}\rangle - \frac{\frac{nd}{2}}{L_2}\langle u_{\mathrm{C}4}\rangle \\
\frac{\mathrm{d}}{\mathrm{d}t}\langle i_{\mathrm{L}3}\rangle &= \frac{1}{L_3}\langle u_{\mathrm{C}3}\rangle + \frac{1}{L_3}\langle u_{\mathrm{C}4}\rangle - \frac{1}{L_3}\langle u_\mathrm{o}\rangle \\
\frac{\mathrm{d}}{\mathrm{d}t}\langle u_{\mathrm{C}1}\rangle &= -\frac{1}{C_1}\langle i_{\mathrm{L}1}\rangle + \frac{1}{C_1}\langle i_\mathrm{in}\rangle \\
\frac{\mathrm{d}}{\mathrm{d}t}\langle u_{\mathrm{C}2}\rangle &= \frac{d}{C_2}\langle i_{\mathrm{L}1}\rangle - \frac{1}{C_2}\langle i_{\mathrm{L}2}\rangle \\
\frac{\mathrm{d}}{\mathrm{d}t}\langle u_{\mathrm{C}3}\rangle &= \frac{\frac{nd}{2}}{C_3}\langle i_{\mathrm{L}2}\rangle - \frac{1}{C_3}\langle i_{\mathrm{L}3}\rangle \\
\frac{\mathrm{d}}{\mathrm{d}t}\langle u_{\mathrm{C}4}\rangle &= \frac{\frac{nd}{2}}{C_4}\langle i_{\mathrm{L}2}\rangle - \frac{1}{C_4}\langle i_{\mathrm{L}3}\rangle \\
\langle u_\mathrm{in}\rangle &= \langle u_{\mathrm{C}1}\rangle \\
\langle i_\mathrm{o}\rangle &= \langle i_{\mathrm{L}3}\rangle,
\end{aligned} \tag{2.26}$$

where the turns ratio of the main transformer is denoted by n for clarity according to

$$n = \frac{N_1}{N_2}. \tag{2.27}$$

The small-signal state space can be obtained by linearizing (i.e., developing the partial derivatives) the equations in (2.26), yielding

$$
\begin{aligned}
\frac{\mathrm{d}}{\mathrm{d}t}\hat{i}_{\mathrm{L1}} &= -\frac{R_1}{L_1}\hat{i}_{\mathrm{L1}} - \frac{R_2}{L_1}\hat{i}_{\mathrm{L2}} + \frac{1}{L_1}\hat{u}_{\mathrm{C1}} - \frac{D}{L_1}\hat{u}_{\mathrm{C2}} + \frac{r_{\mathrm{C1}}}{L_1}\hat{i}_{\mathrm{in}} - \frac{U_1}{L_1}\hat{d} \\
\frac{\mathrm{d}}{\mathrm{d}t}\hat{i}_{\mathrm{L2}} &= -\frac{R_2}{L_2}\hat{i}_{\mathrm{L1}} - \frac{R_3}{L_2}\hat{i}_{\mathrm{L2}} + \frac{DR_4}{L_2}\hat{i}_{\mathrm{L3}} + \frac{1}{L_2}\hat{u}_{\mathrm{C2}} - \frac{\frac{nD}{2}}{L_2}\hat{u}_{\mathrm{C3}} \\
&\quad - \frac{\frac{nD}{2}}{L_2}\hat{u}_{\mathrm{C4}} + \frac{1}{L_2}\hat{u}_{\mathrm{o}} - \frac{U_2}{L_2}\hat{d} \\
\frac{\mathrm{d}}{\mathrm{d}t}\hat{i}_{\mathrm{L3}} &= \frac{DR_4}{L_3}\hat{i}_{\mathrm{L2}} - \frac{R_5}{L_3}\hat{i}_{\mathrm{L3}} + \frac{1}{L_3}\hat{u}_{\mathrm{C3}} + \frac{1}{L_3}\hat{u}_{\mathrm{C4}} + \frac{R_4 I_{\mathrm{L2}}}{L_3}\hat{d} \\
\frac{\mathrm{d}}{\mathrm{d}t}\hat{u}_{\mathrm{C1}} &= -\frac{1}{C_1}\hat{i}_{\mathrm{L1}} + \frac{1}{C_1}\hat{i}_{\mathrm{in}} \\
\frac{\mathrm{d}}{\mathrm{d}t}\hat{u}_{\mathrm{C2}} &= \frac{D}{C_2}\hat{i}_{\mathrm{L1}} - \frac{1}{C_2}\hat{i}_{\mathrm{L2}} + \frac{I_{\mathrm{L2}}}{C_2}\hat{d} \\
\frac{\mathrm{d}}{\mathrm{d}t}\hat{u}_{\mathrm{C3}} &= \frac{\frac{nD}{2}}{C_3}\hat{i}_{\mathrm{L2}} - \frac{1}{C_3}\hat{i}_{\mathrm{L3}} + \frac{nI_{\mathrm{L2}}}{C_3}\hat{d} \\
\frac{\mathrm{d}}{\mathrm{d}t}\hat{u}_{\mathrm{C4}} &= \frac{\frac{nD}{2}}{C_4}\hat{i}_{\mathrm{L2}} - \frac{1}{C_4}\hat{i}_{\mathrm{L3}} + \frac{nI_{\mathrm{L2}}}{C_4}\hat{d} \\
\hat{u}_{\mathrm{in}} &= -r_{\mathrm{C1}}\hat{i}_{\mathrm{L1}} + \hat{u}_{\mathrm{C1}} + r_{\mathrm{C1}}\hat{i}_{\mathrm{in}} \\
\hat{i}_{\mathrm{o}} &= \hat{i}_{\mathrm{L3}}.
\end{aligned}
\tag{2.28}
$$

where the parasitic elements are defined as follows:

$$
\begin{aligned}
R_1 &= r_{\mathrm{C1}} + r_{\mathrm{L1}} + D(r_{\mathrm{D2}} + r_{\mathrm{C2}}) + D'(r_{\mathrm{D2}} + r_{\mathrm{C2}}) \\
R_2 &= D' r_{\mathrm{ds}} - D r_{\mathrm{C2}} \\
R_3 &= r_{\mathrm{C2}} + r_{\mathrm{L2}} + r_{\mathrm{ds}} + D(r_{\mathrm{ds}} + r_{\mathrm{pri}}) \\
R_4 &= \frac{n}{2}(r_{\mathrm{C3}} + r_{\mathrm{C4}}) \\
R_5 &= r_{\mathrm{C3}} + r_{\mathrm{C4}} + r_{\mathrm{L3}} \\
U_1 &= (r_{\mathrm{D2}} + r_{\mathrm{C2}} - r_{\mathrm{D1}} - r_{\mathrm{ds}})I_{\mathrm{L1}} - (r_{\mathrm{ds}} + r_{\mathrm{C2}})I_{\mathrm{L2}} \\
&\quad + U_{\mathrm{C2}} + U_{\mathrm{D2}} - U_{\mathrm{D1}} \\
U_2 &= \frac{n}{2}\left[U_{\mathrm{C3}} + U_{\mathrm{C4}} + U_{\mathrm{D3}} + U_{\mathrm{D4}} - (r_{\mathrm{C3}} + r_{\mathrm{C4}})I_{\mathrm{L3}}\right] \\
&\quad - (r_{\mathrm{ds}} + r_{\mathrm{C2}})I_{\mathrm{L1}} + (r_{\mathrm{ds}} + r_{\mathrm{pri}})I_{\mathrm{L2}} \\
&\quad \frac{n^2}{2}(2r_{\mathrm{sec}} + r_{\mathrm{D3}} + r_{\mathrm{C3}} + r_{\mathrm{D3}} + r_{\mathrm{C4}})I_{\mathrm{L2}}.
\end{aligned}
\tag{2.29}
$$

The voltages U_{D} represent the forward voltage losses of the diodes, with the resistances r_{D} denoting the dynamic forward characteristics of the diodes. The resistances r_{L} and r_{C}

denote the series resistances of the inductors and capacitors and, finally, the resistances r_{ds}, r_{pri}, r_{sec} denote the resistances of the switch channel and the main transformer windings, respectively. The measured transfer functions and the design of the input-voltage control loop are presented in Chapter 4. In addition, a Matlab$^{\mathrm{TM}}$ m-file for plotting analytical transfer functions is given in the attachments.

The steady-state operating point can be found according to well-known volt-second and ampere-second balances (Erickson and Maksimović, 2001), yielding the following steady-state relations. The parasitic elements have been left out for clarity, although they affect the actual steady-state values. There is an additional m-file in the attachments for solving symbolic transfer functions with the parasitic elements.

$$\begin{aligned} U_{\mathrm{C3}} &= U_{\mathrm{C4}} = \frac{1}{2}U_{\mathrm{o}} & I_{\mathrm{L1}} &= I_{\mathrm{in}} \\ U_{\mathrm{C2}} &= nDU_{\mathrm{C3}} = nDU_{\mathrm{C4}} & I_{\mathrm{L2}} &= DI_{\mathrm{L1}} \\ U_{\mathrm{C1}} &= DU_{\mathrm{C2}} & I_{\mathrm{L3}} &= \frac{nD}{2}I_{\mathrm{L2}} \\ U_{\mathrm{in}} &= U_{\mathrm{C1}} & I_{\mathrm{o}} &= I_{\mathrm{L3}} \\ \Rightarrow U_{\mathrm{in}} &= \frac{nD^2}{2}U_{\mathrm{o}} & \Rightarrow I_{\mathrm{o}} &= \frac{nD^2}{2}I_{\mathrm{in}}. \end{aligned} \tag{2.30}$$

The operating-point relations reveal the quadratic dependencies between the input and the output voltage and the corresponding currents. Hence, the constant output voltage is reflected to the input by the quadratic modulo $M(D)$ and the input current is reflected to the output, respectively:

$$U_{\mathrm{in}} = M(D)U_{\mathrm{o}}\ ,\ I_{\mathrm{o}} = M(D)I_{\mathrm{in}}\ ,\ M(D) = \frac{nD^2}{2}\ ,\ 0 \leq D \leq 1. \tag{2.31}$$

The main transformer turns ratio is determined in such a way that the defined maximum input voltage ($U_{\mathrm{in,max}}$) is achieved at the maximum duty cycle (D_{max}) and at the defined minimum value of the voltage-type load ($U_{\mathrm{o,min}}$) according to (2.32):

$$n = \frac{2U_{\mathrm{in,max}}}{D_{\mathrm{max}}^2 U_{\mathrm{o,min}}}. \tag{2.32}$$

Since the proposed converter contains a high-frequency transformer, attention must be paid to avoid the saturation of the transformer core. Using a secondary arrangement of Fig. 2.12, no external measures need to be taken as the secondary capacitors effectively block the dc component of the magnetizing current. However, if a full-wave rectifier arrangement is used at the secondary side, an additional blocking capacitor must be implemented in series with the secondary winding, because there is no inherent mechanism

preventing the saturation of the transformer, contrary to the statement by Song and Lehman (2007). Additionally, a full-wave rectifier arrangement would subject the secondary winding to full output voltage, whereas in the arrangement in Fig. 2.12 only one half of the output voltage is applied on the secondary winding. This would change the turns ratio of the transformer by a factor of 2 and, thus, affect the design as both the voltage and current levels change.

2.4.2 Cascaded Buck-Boost Converters

The power stage of a current-fed buck-boost converter is presented in Fig. 2.16, with an additional output-side CL-type filter (C_2, L_2) included. The input variables are, therefore, $\hat{u}_\mathrm{o}, \hat{i}_\mathrm{in}$, the state variables $\hat{i}_\mathrm{L1}, \hat{i}_\mathrm{L2}, \hat{u}_\mathrm{C1}, \hat{u}_\mathrm{C2}$ and the output variables $\hat{u}_\mathrm{in}, \hat{i}_\mathrm{o}$.

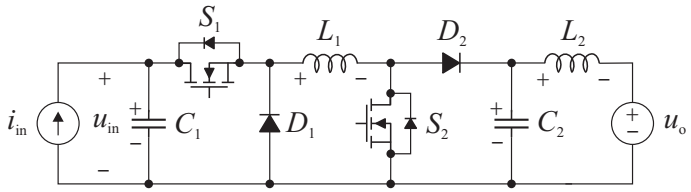

Fig. 2.16. Schematic diagram of a current-fed buck-boost converter.

The buck-boost converter operates as follows: During on-time (t_on), the diodes conduct, yielding the sub-circuit shown in Fig. 2.17. During off-time (t_off), respectively, the switches conduct, yielding the sub-circuit in Fig. 2.18. The parasitic elements are left out of the sub-circuits for clarity.

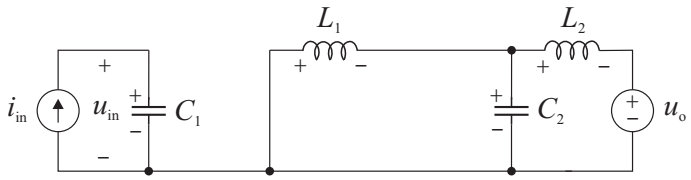

Fig. 2.17. On-time sub-circuit.

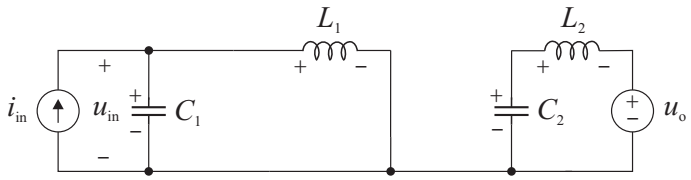

Fig. 2.18. Off-time sub-circuit.

Combining the equations depicting the on-time and off-time sub-circuits, the averaged model (2.33) is obtained:

$$\begin{aligned}
\frac{\mathrm{d}}{\mathrm{d}t}\langle i_{\mathrm{L1}}\rangle &= \frac{r_{\mathrm{L1}} + d(r_{\mathrm{D1}} + r_{\mathrm{D2}} + r_{\mathrm{C2}}) + d'(r_{\mathrm{C1}} + r_{\mathrm{ds1}} + r_{\mathrm{ds2}})}{L_1}\langle i_{\mathrm{L1}}\rangle + \frac{dr_{\mathrm{C2}}}{L_1}\langle i_{\mathrm{L2}}\rangle \\
&\quad + \frac{d'}{L_1}\langle u_{\mathrm{C1}}\rangle - \frac{d}{L_1}\langle u_{\mathrm{C2}}\rangle + \frac{d'r_{\mathrm{C1}}}{L_1}\langle i_{\mathrm{in}}\rangle - \frac{d(U_{\mathrm{D1}} + U_{\mathrm{D2}})}{L_1} \\
\frac{\mathrm{d}}{\mathrm{d}t}\langle i_{\mathrm{L2}}\rangle &= \frac{d'r_{\mathrm{C2}}}{L_2}\langle i_{\mathrm{L1}}\rangle - \frac{r_{\mathrm{C2}} + r_{\mathrm{L2}}}{L_2}\langle i_{\mathrm{L2}}\rangle + \frac{1}{L_2}\langle u_{\mathrm{C2}}\rangle - \frac{1}{L_2}\langle u_{\mathrm{o}}\rangle \\
\frac{\mathrm{d}}{\mathrm{d}t}\langle u_{\mathrm{C1}}\rangle &= -\frac{d'}{C_1}\langle i_{\mathrm{L1}}\rangle + \frac{1}{C_1}\langle i_{\mathrm{in}}\rangle \\
\frac{\mathrm{d}}{\mathrm{d}t}\langle u_{\mathrm{C2}}\rangle &= \frac{d}{C_2}\langle i_{\mathrm{L1}}\rangle - \frac{1}{C_2}\langle i_{\mathrm{L2}}\rangle \\
\langle u_{\mathrm{in}}\rangle &= -d'r_{\mathrm{C1}}\langle i_{\mathrm{L1}}\rangle + \langle u_{\mathrm{C1}}\rangle + r_{\mathrm{C1}}\langle i_{\mathrm{in}}\rangle \\
\langle i_{\mathrm{o}}\rangle &= \langle i_{\mathrm{L2}}\rangle,
\end{aligned} \tag{2.33}$$

where the parasitic elements include the inductor resistances $r_{\mathrm{L1}}, r_{\mathrm{L2}}$, the switch channel resistances $r_{\mathrm{ds1}}, r_{\mathrm{ds2}}$, the capacitor resistances $r_{\mathrm{C1}}, r_{\mathrm{C2}}$ and the diode resistances and the forward voltage drops $r_{\mathrm{D1}}, r_{\mathrm{D2}}$ and $U_{\mathrm{D1}}, U_{\mathrm{D2}}$, respectively.

By linearizing the averaged model, the resulting small-signal state-space can be presented as

$$\begin{aligned}
\frac{\mathrm{d}}{\mathrm{d}t}\hat{i}_{\mathrm{L1}} &= -\frac{R_1}{L_1}\hat{i}_{\mathrm{L1}} + \frac{Dr_{\mathrm{C2}}}{L_1}\hat{i}_{\mathrm{L2}} + \frac{D'}{L_1}\hat{u}_{\mathrm{C1}} - \frac{D}{L_1}\hat{u}_{\mathrm{C2}} + \frac{D'r_{\mathrm{C1}}}{L_1}\hat{i}_{\mathrm{in}} - \frac{U_1}{L_1}\hat{d} \\
\frac{\mathrm{d}}{\mathrm{d}t}\hat{i}_{\mathrm{L2}} &= \frac{Dr_{\mathrm{C2}}}{L_2}\hat{i}_{\mathrm{L1}} - \frac{r_{\mathrm{L2}} + r_{\mathrm{C2}}}{L_2}\hat{i}_{\mathrm{L2}} + \frac{1}{L_2}\hat{u}_{\mathrm{C2}} - \frac{1}{L_2}\hat{u}_{\mathrm{o}} + \frac{r_{\mathrm{C2}}I_{\mathrm{L1}}}{L_2}\hat{d} \\
\frac{\mathrm{d}}{\mathrm{d}t}\hat{u}_{\mathrm{C1}} &= -\frac{D'}{C_1}\hat{i}_{\mathrm{L1}} + \frac{1}{C_1}\hat{i}_{\mathrm{in}} + \frac{I_{\mathrm{L1}}}{C_1}\hat{d} \\
\frac{\mathrm{d}}{\mathrm{d}t}\hat{u}_{\mathrm{C2}} &= \frac{D}{C_2}\hat{i}_{\mathrm{L1}} - \frac{1}{C_2}\hat{i}_{\mathrm{L2}} + \frac{I_{\mathrm{L1}}}{C_2}\hat{d} \\
\hat{u}_{\mathrm{in}} &= -D'r_{\mathrm{C1}}\hat{i}_{\mathrm{L1}} + \hat{u}_{\mathrm{C1}} + r_{\mathrm{C1}}\hat{i}_{\mathrm{in}} + r_{\mathrm{C1}}I_{\mathrm{L1}}\hat{d} \\
\hat{i}_{\mathrm{o}} &= \hat{i}_{\mathrm{L2}}
\end{aligned} \tag{2.34}$$

where the additional variables R_1 and U_1 are defined as follows:

$$\begin{aligned}
R_1 &= r_{\mathrm{L1}} + D(r_{\mathrm{D2}} + r_{\mathrm{D2}} + r_{\mathrm{C2}}) + D'(r_{\mathrm{ds1}} + r_{\mathrm{ds2}} + r_{\mathrm{C1}}) \\
U_1 &= (r_{\mathrm{D1}} + r_{\mathrm{D2}} + r_{\mathrm{C2}} - r_{\mathrm{ds1}} - r_{\mathrm{ds2}} - r_{\mathrm{C2}})I_{\mathrm{L1}} - r_{\mathrm{C2}}I_{\mathrm{L2}} \\
&\quad + U_{\mathrm{C1}} + U_{\mathrm{C2}} + U_{\mathrm{D1}} + U_{\mathrm{D2}} - r_{\mathrm{C1}}I_{\mathrm{in}}.
\end{aligned} \tag{2.35}$$

The steady-state values for capacitor voltages, inductor currents and the output variables without the parasitic elements are

$$\begin{aligned} U_{C1} &= \frac{D}{D'}U_o & I_{L1} &= \frac{1}{D'}I_{in} \\ U_{C2} &= U_o & I_{L2} &= \frac{D}{D'}I_{in} \\ \Rightarrow U_{in} &= \frac{D}{D'}U_o & \Rightarrow I_o &= \frac{D}{D'}I_{in}. \end{aligned} \tag{2.36}$$

The m-files for solving analytical transfer functions both numerically and symbolically are included in the attachments. Operating the buck-boost converter either in buck mode or boost mode (i.e., by disabling unnecessary switching action) yields higher operational efficiency than conventional buck-boost operation. This scheme has been adressed in numerous publications (e.g. by Linares et al. (2009) and Posthkouhi et al. (2011)). Conventional operation can be used to simplify the analysis and practical verification, as the same results and rules apply regardless of operation mode.

Models for Cascaded Structures

To model the small-signal behavior of cascaded converters in DMPPT applications, two system models representing both alternatives were formed using H-parameter scheme (Fig. 2.19).

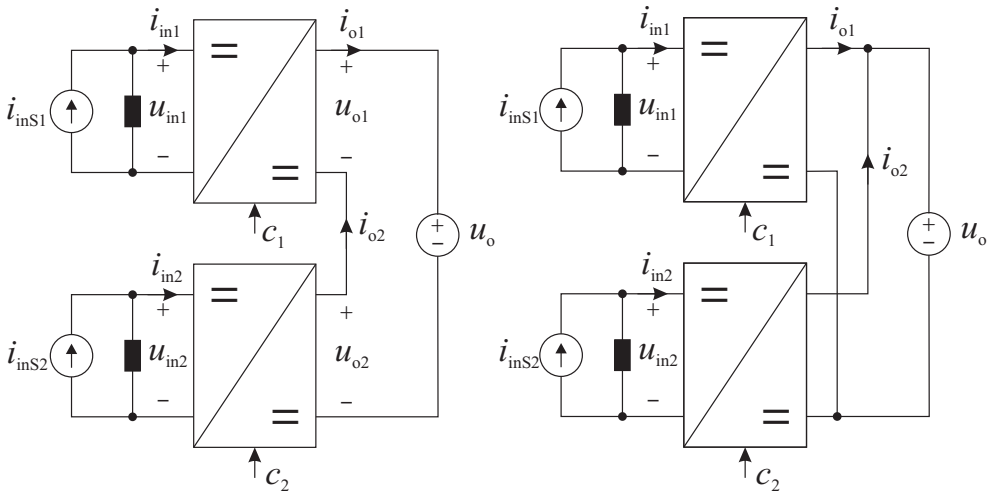

(a) Series configuration. **(b)** Parallel configuration.

Fig. 2.19. Cascaded H-parameter networks with non-ideal sources.

In both models, the individual H-parameter networks have non-ideal current sources

(i_{inS1}, i_{inS2}) at the input terminals and a constant-voltage load (u_{o}) at the system output. A network model for the complete system is formed by merging two individual network models together, yielding the series-connected system model (Fig. 2.21) and the parallel-connected system model (Fig. 2.20), respectively. By computing the transfer functions from the series configuration, one obtains the matrix expression as shown in (2.37).

$$\begin{bmatrix} \hat{u}_{\mathrm{in1}} \\ \hat{u}_{\mathrm{in2}} \\ \hat{i}_{\mathrm{o}} \end{bmatrix} = \begin{bmatrix} Z_{\mathrm{in1}}^{\mathrm{S,c}} & T_{\mathrm{cr1}}^{\mathrm{S,c}} & T_{\mathrm{oi1}} & G_{\mathrm{ci1}}^{\mathrm{S,c}} & G_{\mathrm{cr1}}^{\mathrm{S,c}} \\ T_{\mathrm{cr2}}^{\mathrm{S,c}} & Z_{\mathrm{in2}}^{\mathrm{S,c}} & T_{\mathrm{oi2}} & G_{\mathrm{cr2}}^{\mathrm{S,c}} & G_{\mathrm{ci2}}^{\mathrm{S,c}} \\ G_{\mathrm{io1}}^{\mathrm{S,c}} & G_{\mathrm{io2}}^{\mathrm{S,c}} & -Y_{\mathrm{tot}} & G_{\mathrm{co1}}^{\mathrm{S,c}} & G_{\mathrm{co2}}^{\mathrm{S,c}} \end{bmatrix} \begin{bmatrix} \hat{i}_{\mathrm{inS1}} \\ \hat{i}_{\mathrm{inS2}} \\ \hat{u}_{\mathrm{o}} \\ \hat{c}_1 \\ \hat{c}_2 \end{bmatrix}, \tag{2.37}$$

where the additional superscript 'c' denotes transfer functions affected by cross-coupling. According to Eq. (2.37), there are cross-couplings between the two input sources, both from the converter 1 control signal to converter 2 input voltage (i.e., $\hat{u}_{\mathrm{in2}}/\hat{c}_1$, $G_{\mathrm{cr2}}^{\mathrm{c}}$) and from converter 1 input current to converter 2 input voltage ($\hat{u}_{\mathrm{in2}}/\hat{i}_{\mathrm{in1}}$, $T_{\mathrm{cr2}}^{\mathrm{c}}$), and vice versa. This would imply that the series connection might suffer from unexpected effects caused by the cross-couplings.

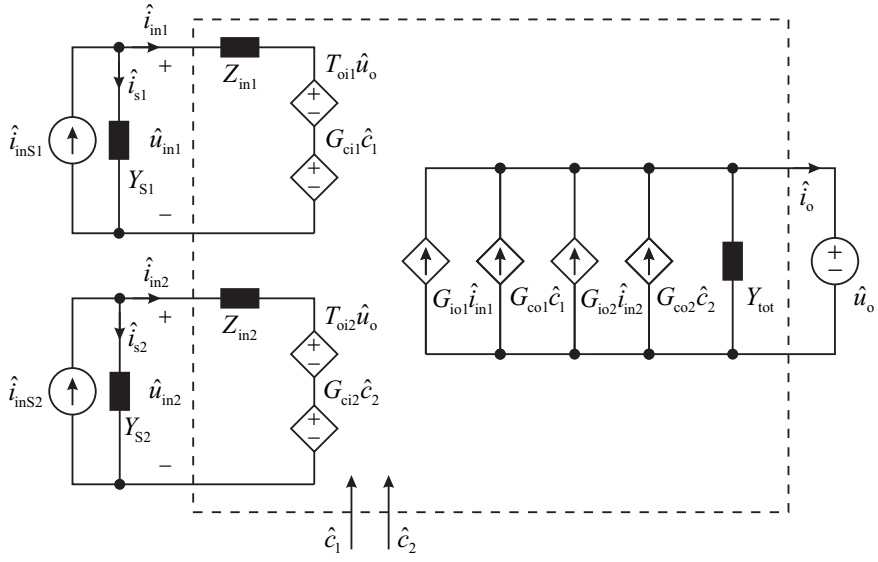

Fig. 2.20. Network model for parallel-connected H-parameter networks with non-ideal sources.

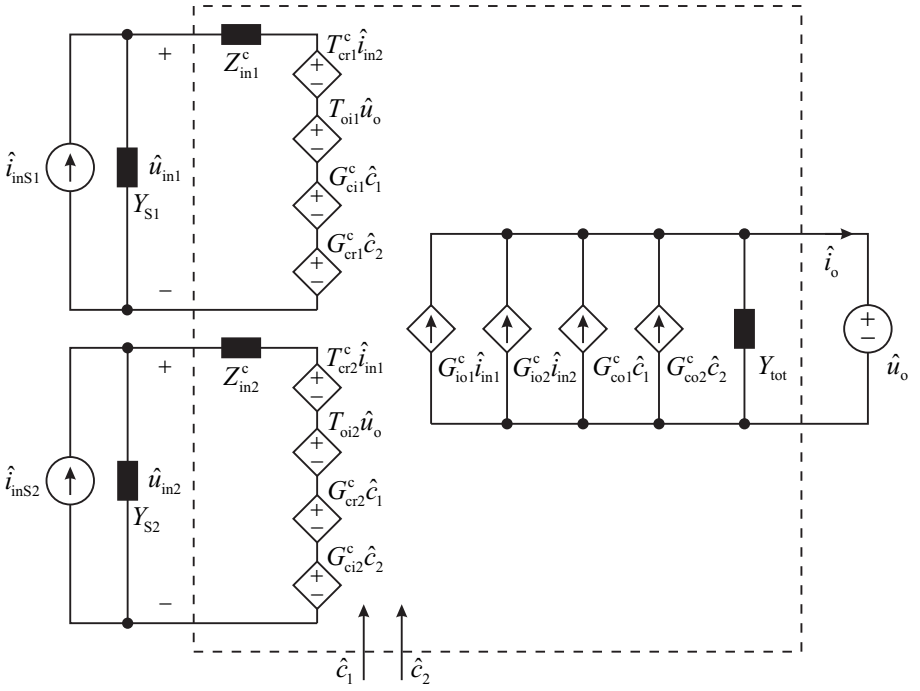

Fig. 2.21. Network model for series-connected H-parameter networks with non-ideal sources.

Similar analysis can be performed for the parallel configuration, resulting in the following set of transfer functions:

$$\begin{bmatrix} \hat{u}_{\mathrm{in1}} \\ \hat{u}_{\mathrm{in2}} \\ \hat{i}_{\mathrm{o}} \end{bmatrix} = \begin{bmatrix} Z^{\mathrm{S}}_{\mathrm{in1}} & 0 & T^{\mathrm{S}}_{\mathrm{oi1}} & G^{\mathrm{S}}_{\mathrm{ci1}} & 0 \\ 0 & Z^{\mathrm{S}}_{\mathrm{in2}} & T^{\mathrm{S}}_{\mathrm{oi2}} & 0 & G^{\mathrm{S}}_{\mathrm{ci2}} \\ G^{\mathrm{S}}_{\mathrm{io1}} & G^{\mathrm{S}}_{\mathrm{io2}} & -Y^{\mathrm{S}}_{\mathrm{tot}} & G^{\mathrm{S}}_{\mathrm{co1}} & G^{\mathrm{S}}_{\mathrm{co2}} \end{bmatrix} \begin{bmatrix} \hat{i}_{\mathrm{inS1}} \\ \hat{i}_{\mathrm{inS2}} \\ \hat{u}_{\mathrm{o}} \\ \hat{c}_{1} \\ \hat{c}_{2} \end{bmatrix} \tag{2.38}$$

The conclusion is that there are no cross-coupling effects between parallel-connected converters in the presented system configuration (i.e., with an ideal load), indicating superior performance over the series configuration (Huusari and Suntio, 2012a).

The cross-coupling effects can be explained intuitively as well, by examining the system structures in Figs. 2.21 and 2.20. In parallel configuration, for each H-parameter network there are two defined input variables. In series configuration, however, only the input current is constant. Because the input variable related to the output terminal is

undefined, the output variable related to the input terminal (i.e., the input voltage) is a product of two undefined variables: the modulo $m(d)$ and the output voltage u_o. In parallel configuration, the input voltage for each converter is a product of the modulo $m(d)$ and the constant output voltage u_o.

Non-Ideal Load in Parallel Configuration

By adding an arbitrary series impedance to the load, the effects of load-imposed cross-couplings in parallel configuration can be studied. The series configuration with a non-ideal load is not examined, as the existence of cross-couplings in series configuration is already verified. The network model for parallel-connected H-parameter networks with common, non-ideal load is presented in Fig. 2.22.

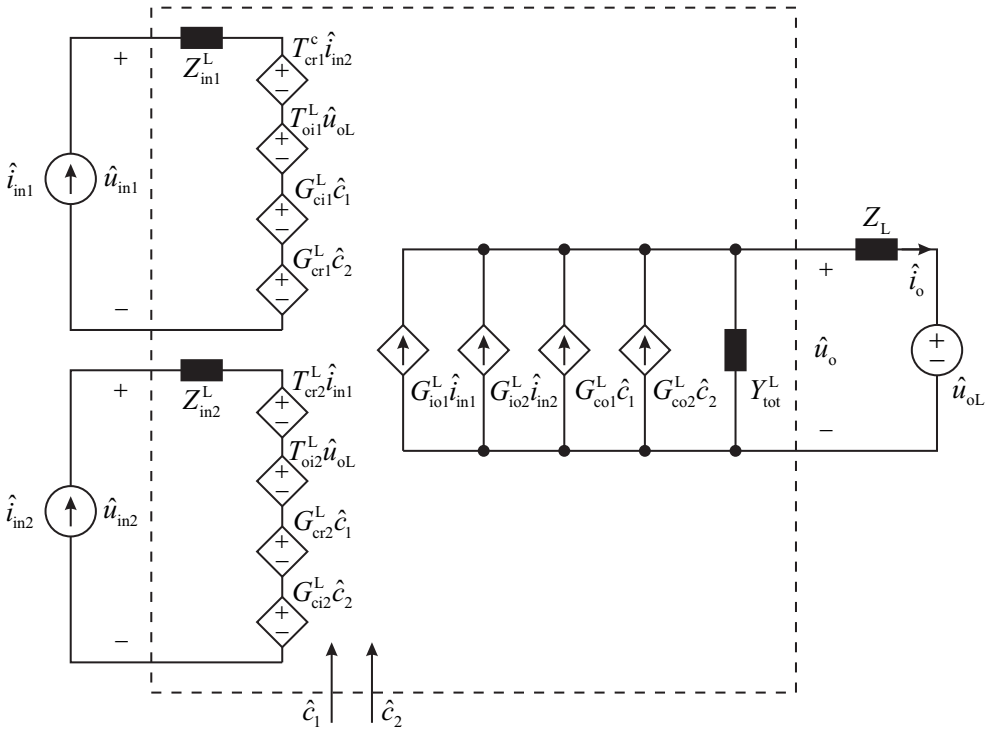

Fig. 2.22. Network model for parallel-connected H-parameter networks with non-ideal load.

The corresponding transfer functions can be presented in matrix form according to (2.39), where superscript 'L' denotes load effect and additional superscript 'c' cross-coupling effect.

$$\begin{bmatrix} \hat{u}_{\mathrm{in1}} \\ \hat{u}_{\mathrm{in2}} \\ \hat{i}_{\mathrm{o}} \end{bmatrix} = \begin{bmatrix} Z^{\mathrm{L}}_{\mathrm{in1}} & T^{\mathrm{L,c}}_{\mathrm{cr1}} & T^{\mathrm{L}}_{\mathrm{oi1}} & G^{\mathrm{L}}_{\mathrm{ci1}} & G^{\mathrm{L,c}}_{\mathrm{cr1}} \\ T^{\mathrm{L,c}}_{\mathrm{cr2}} & Z^{\mathrm{L}}_{\mathrm{in2}} & T^{\mathrm{L}}_{\mathrm{oi2}} & G^{\mathrm{L,c}}_{\mathrm{cr2}} & G^{\mathrm{L}}_{\mathrm{ci2}} \\ G^{\mathrm{L}}_{\mathrm{io1}} & G^{\mathrm{L}}_{\mathrm{io2}} & -Y^{\mathrm{L}}_{\mathrm{tot}} & G^{\mathrm{L}}_{\mathrm{co1}} & G^{\mathrm{L}}_{\mathrm{co2}} \end{bmatrix} \begin{bmatrix} \hat{i}_{\mathrm{in1}} \\ \hat{i}_{\mathrm{in2}} \\ \hat{u}_{\mathrm{oL}} \\ \hat{c}_1 \\ \hat{c}_2 \end{bmatrix}. \tag{2.39}$$

Thus, it can be stated that both system configurations contain cross-coupling effects, although introduced by various reasons. The actual effect on the system performance is dictated by the magnitude of these non-idealities (i.e., by the magnitude of corresponding impedances), as indicated in the corresponding equations.

Open-Loop Transfer Functions in Cascaded H-parameter Configurations

For the series-connected system, the transfer functions become rather complex due to cross-couplings and inclusion of source non-idealities. If source non-idealities are neglected, the cross-coupling-affected transfer functions related to input port 1 (i.e., the first row in the matrix in (2.37), without T_{oi} can be given as follows

$$\begin{aligned} Z^{\mathrm{c}}_{\mathrm{in1}} &= Z_{\mathrm{in1}} - T_{\mathrm{io1}} G_{\mathrm{io1}} \frac{Y_{\mathrm{o2}}}{Y^2_{\mathrm{o1}}} & G^{\mathrm{c}}_{\mathrm{ci}} &= G_{\mathrm{ci1}} - T_{\mathrm{io1}} G_{\mathrm{co1}} \frac{Y_{\mathrm{o2}}}{Y^2_{\mathrm{o1}}} \\ T^{\mathrm{c}}_{\mathrm{cr1}} &= -T_{\mathrm{io1}} G_{\mathrm{io2}} \frac{Y_{\mathrm{tot}}}{Y_{\mathrm{o1}} Y_{\mathrm{o2}}} & G^{\mathrm{c}}_{\mathrm{cr}} &= -T_{\mathrm{io1}} G_{\mathrm{co2}} \frac{Y_{\mathrm{tot}}}{Y_{\mathrm{o1}} Y_{\mathrm{o2}}} \end{aligned} \tag{2.40}$$

where $T^{\mathrm{c}}_{\mathrm{cr1}}$ represents the input cross-coupling transfer function and $G^{\mathrm{c}}_{\mathrm{cr1}}$ the control cross-coupling transfer function. These equations state that the greater the output admittance in a single converter (the smaller the output impedance), the weaker are the cross-coupling effects. In other words, the performance of series configuration is improved, if the individual converters operate as voltage sources having small output impedance. Respectively, a current source behavior increases the cross-coupling effects.

The open-loop transfer functions for parallel-connected system with non-ideal sources in (2.38) are equal to the corresponding source-affected transfer functions for a single converter, except the system output admittance, which can be expressed as

$$Y^{\mathrm{S}}_{\mathrm{tot}} = Y_{\mathrm{o1}} + Y_{\mathrm{o2}} + \frac{G_{\mathrm{io1}} T_{\mathrm{oi1}} Y_{\mathrm{S1}}}{1 + Z_{\mathrm{in1}} Y_{\mathrm{S1}}} + \frac{G_{\mathrm{io2}} T_{\mathrm{oi2}} Y_{\mathrm{S2}}}{1 + Z_{\mathrm{in2}} Y_{\mathrm{S2}}}. \tag{2.41}$$

Therefore, in the parallel configuration neither the system nor non-ideal sources in-

troduce cross-coupling effects that would interfere with the system operation, whereas in series configuration the cross-couplings emerge already from the system configuration.

The open-loop transfer functions for the input channel 1 in parallel configuration with a non-ideal load can be given as in (2.42)

$$\begin{aligned} Z_{\mathrm{in1}}^{\mathrm{L}} &= Z_{\mathrm{in1}}\frac{1+Z_{\mathrm{L}}Y_{\mathrm{o1\text{-}sci}}}{1+Z_{\mathrm{L}}Y_{\mathrm{tot}}} & G_{\mathrm{ci1}}^{\mathrm{c}} &= G_{\mathrm{ci1}}\frac{1+Z_{\mathrm{L}}Y_{\mathrm{o1\text{-}\infty}}}{1+Z_{\mathrm{L}}Y_{\mathrm{tot}}} \\ T_{\mathrm{cr1}}^{\mathrm{c}} &= \frac{Z_{\mathrm{L}}T_{\mathrm{o1}}G_{\mathrm{io2}}}{1+Z_{\mathrm{L}}Y_{\mathrm{tot}}} & G_{\mathrm{cr1}}^{\mathrm{c}} &= \frac{Z_{\mathrm{L}}T_{\mathrm{o1}}G_{\mathrm{co2}}}{1+Z_{\mathrm{L}}Y_{\mathrm{tot}}} \\ T_{\mathrm{oi1}}^{\mathrm{L}} &= T_{\mathrm{oi1}}\frac{1}{1+Z_{\mathrm{L}}Y_{\mathrm{tot}}} \end{aligned} \tag{2.42}$$

Thus, the smaller the load impedance, the weaker the cross-coupling effects. In PV applications, the load for DMPPT converters is the input terminal of the inverter, which acts as a voltage-type load due to inverter control structure, maintaining the input voltage at a constant value. This would imply that the inverter input impedance is low and the load-imposed cross-couplings would be negligible.

Closed-Loop Transfer Functions in Cascaded Configurations

The closed-loop transfer functions in series configuration can be computed most conveniently by the corresponding control engineering block diagram, formed in a similar way as in Fig. 2.10.

Because the series configuration is mostly plagued by input-side cross-coupling effects, the block diagram in Fig. 2.23 can be used to examine the closed-loop cross-coupling transfer functions, corresponding to the matrix equation (2.37). For input channel 1, these are the input cross-coupling transfer function $T_{\mathrm{cr1\text{-}c}}^{\mathrm{S,c}} = \hat{u}_{\mathrm{in1}}/\hat{i}_{\mathrm{inS2}}$ and the control cross-coupling transfer function $G_{\mathrm{cr1\text{-}c}}^{\mathrm{S,c}} = \hat{u}_{\mathrm{in1}}/\hat{u}_{\mathrm{ref2}}$. For clarity, the superscript 'S,c' has been left out of the transfer functions in the following discussion.

To examine $T_{\mathrm{cr1\text{-}c}}$, for example, all other input variables are set to zero and the expressions for the output variables are written. Manipulation of these equations yield expression for $T_{\mathrm{cr1\text{-}c}}$ as shown in (2.43)

$$T_{\mathrm{cr1\text{-}c}} = \frac{1}{1+L_1}\frac{T_{\mathrm{cr1\text{-}o}} - Z_{\mathrm{in2\text{-}o}}\dfrac{G_{\mathrm{cr1\text{-}o}}}{G_{\mathrm{c2\text{-}o}}}\dfrac{L_2}{1+L_2}}{1-\dfrac{G_{\mathrm{cr1\text{-}o}}}{G_{\mathrm{ci2\text{-}o}}}\dfrac{G_{\mathrm{cr2\text{-}o}}}{G_{\mathrm{ci1\text{-}o}}}\dfrac{L_1}{1+L_1}\dfrac{L_2}{1+L_2}}. \tag{2.43}$$

Considering the low-frequency operation, where the magnitude of both input-voltage loop gains L_1 and L_2 is large (therefore, the ratio $L_2/(1+L_2)$ equals unity and $1+L_1 \approx L_1$), the corresponding transfer function can be approximated as in (2.44).

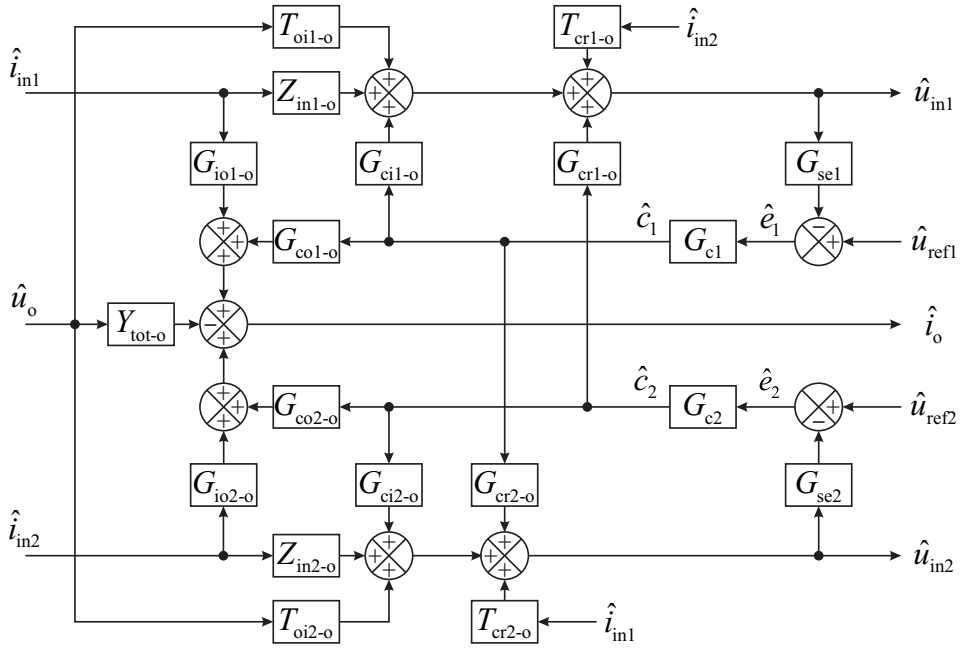

Fig. 2.23. Closed-loop block diagram for series configuration: Source non-idealities included.

$$T_{\text{cr1-c}} \approx \frac{1}{L_1} \frac{T_{\text{cr1-o}} - Z_{\text{in2-o}} \dfrac{G_{\text{cr1-o}}}{G_{\text{c2-o}}}}{1 - \dfrac{G_{\text{cr1-o}}}{G_{\text{ci2-o}}} \dfrac{G_{\text{cr2-o}}}{G_{\text{ci1-o}}}} \approx 0. \tag{2.44}$$

Thus, the loop gain L_1 dominates the low-frequency value of the transfer function, effectively forcing the magnitude $|T_{\text{cr1-c}}|$ to a very low value. Therefore, the closed-loop operation acts as to reduce the input cross-coupling effects, thereby improving the system performance.

Respectively, the control cross-coupling transfer function $G_{\text{cr1-c}}$ can be presented as

$$G_{\text{cr1-c}} = \frac{1}{1+L_1} \frac{G_{\text{cr1-o}} G_{\text{c2-o}} \left(1 - \dfrac{L_2}{1+L_2}\right)}{1 - \dfrac{G_{\text{cr1-o}}}{G_{\text{ci2-o}}} \dfrac{G_{\text{cr2-o}}}{G_{\text{ci1-o}}} \dfrac{L_1}{1+L_1} \dfrac{L_2}{1+L_2}}, \tag{2.45}$$

and the corresponding low-frequency approximation as

$$G_{\text{cr1-c}} \approx \frac{1}{L_1} \frac{G_{\text{cr1-o}} G_{\text{c2-o}} (1-1)}{1 - \dfrac{G_{\text{cr1-o}}}{G_{\text{ci2-o}}} \dfrac{G_{\text{cr2-o}}}{G_{\text{ci1-o}}}} = 0. \tag{2.46}$$

Similar to input cross-coupling transfer function, the loop gain L_1 acts to reduce the disturbances caused by cross-coupling and by the low-frequency approximation, the control cross-coupling is predicted to vanish. The measured $G_{\mathrm{cr1\text{-}c}}$ for buck-boost converters is presented in Chapter 4, revealing the actual frequency-dependent behavior of the cross-couplings.

Considering the parallel configuration with non-ideal sources, the block diagram for input-voltage controlled system can be expressed according to (2.38) as shown in Fig. 2.24. The parallel configuration, therefore, contains independently operating converters. If the load non-idealities are included, however, the system block diagram equals that presented in Fig. 2.23, where the individual transfer functions contain the load effects. Similar analysis reveals that although there are load-imposed cross-couplings in parallel configuration, the input-voltage control loop effectively cancels them out.

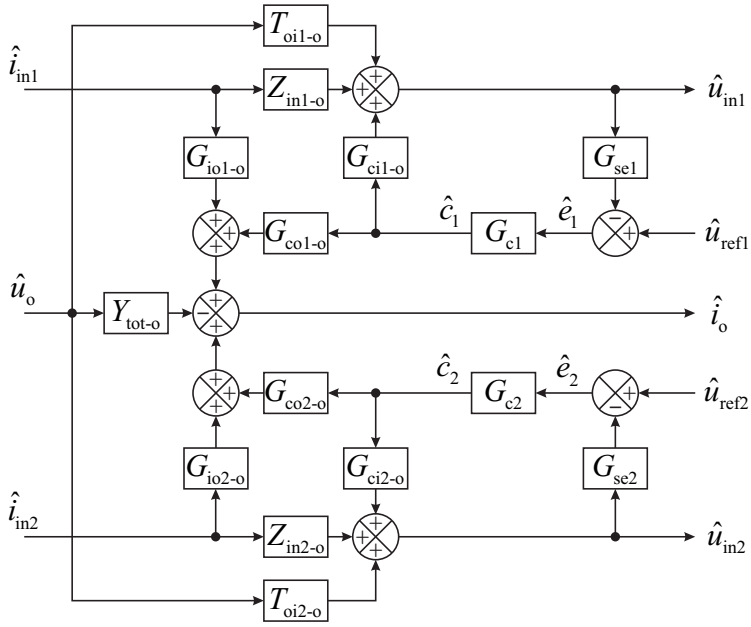

Fig. 2.24. Closed-loop block diagram for parallel configuration: Source non-idealities included.

An excellent example on actual effect of the discussed cross-couplings is presented by Petrone et al. (n.d.): A system of three series-connected converters was studied by introducing an irradiance sequence shown in Fig. 2.25 into PV modules attached to each converter.

The resulting response in the input voltages of the converters at open loop are shown in Fig. 2.26a, revealing the disturbance caused by change in one PV module irradiance. As a result, the MPP operation is lost for all modules. Respectively, under closed-loop

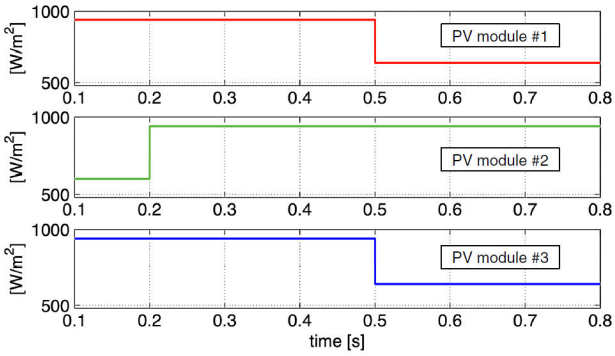

Fig. 2.25. Irradiance sequence for the three PV modules (Petrone et al., n.d.).

operation (Fig. 2.26b), there is no visible disturbance. Thus, the closed-loop operation clearly improves the energy yield of the system.

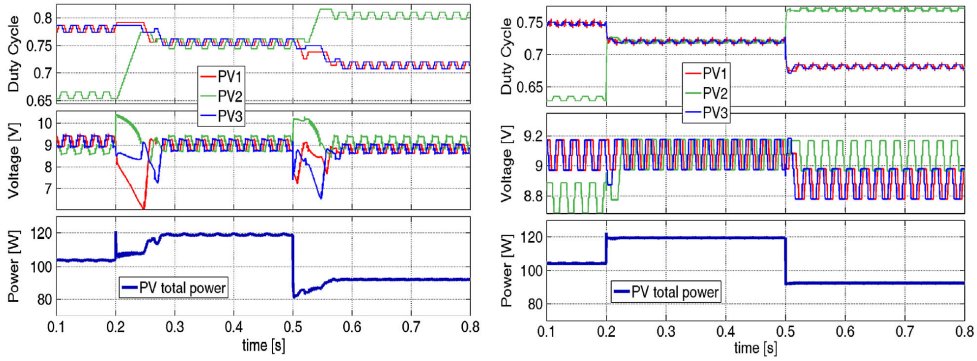

(a) Open-loop operation.

(b) Closed-loop operation.

Fig. 2.26. Simulated example on cross-couplings in series configuration (Petrone et al., n.d.).

2.5 Conclusions

This chapter discussed the modeling methods and concepts relevant to the subject of the thesis. First, a brief introduction to state-space averaging was given, with application to model switched-mode converters. A thorough discussion on the effects of non-ideal load and non-ideal source on the behavior of a switched-mode converter was given as well, emphasizing their significance in the system stability. Considering these non-idealities, a simplified model was presented, which is sufficient for most cases. Additionally, a complete model was presented as well, which can be applied to universal network, either on the

source side or on the load side.

The properties of the PV generator were discussed in the light of small-signal behavior as well. It was shown that due to internal properties of the PV generator (i.e., the relationship of the dynamic resistance r_{pv} to the operating point static resistance R_{pv}), output-side control cannot be applied without compromising the stability of the converter as the MPP is crossed over. Thus, only input-side control is feasible and the feedback has to be taken from the input voltage.

Further, this chapter presented the dynamic model for the patented converter structure as well as dynamic models for system structures composed of two converters, individually characterized by H-parameter networks. It was shown that the series configuration contains inherent cross-couplings, even within ideal system, compromising the open-loop operation. Similar cross-coupling effects do not emerge in parallel-connected system even with non-ideal sources, but a non-ideal load does introduce cross-couplings. However, when both converters operate under input-voltage control loop, these cross-coupling effects were found to effectively vanish, suggesting that PV interfacing dc-dc converters in distributed systems should always have input-voltage control loop. Moreover, in practical DMPPT systems the load impedance is expected to be low in magnitude, effectively removing the cross-coupling effects in parallel configuration.

These findings made on the basis of theoretical analysis are supported by experimental evidence from actual systems, as presented in Chapter 4.

3 DISTRIBUTED PHOTOVOLTAIC ELECTRICITY SYSTEMS

This chapter discusses the distributed photovoltaic electricity systems, their structure and properties as well as the difficulties and practical design issues related to applicable switched-mode converters. A thorough overview is provided for series-connected and parallel-connected dc-dc configurations in DMPPT systems, highlighting the recent viewpoints among researchers in the field. This section justifies the claim that in DMPPT systems, the parallel configuration of dc-dc converters actually provides decent performance and even if otherwise claimed, the conversion efficiency can be high enough for large-scale utilization. Moreover, this section summarizes the interfacing constraints of DMPPT systems, explaining the limitations and operational anomalies that are encountered in the field but mostly left unexplained.

3.1 Introduction

Conventionally, large PV electricity systems are comprised of long strings of PV modules, which are interfaced to the utility grid by means of a VSI-type inverter. Each string contains a number of PV modules connected in series, thus increasing the string voltage high enough for the inverter. These strings have been found to be vulnerable to shading effects, in which the generated power of the string is severely limited by modules that are shaded, e.g., by clouds or shadows caused by nearby objects (Mäki and Valkealahti, 2012). Due to the series connection, each module has to carry equal current, which may force the operating point of the other modules away from the MPP. To overcome this, DMPPT systems have been proposed, where each PV module has a dedicated interfacing converter.

Distributed MPP-tracking systems have been under active research, with novel system configurations and converter topologies especially in the field of building-integrated PV (BIPV) systems, where PV modules are used to replace conventional building structures, such as roof tiles or facade elements (Norton et al., 2011; Roman et al., 2008). The importance of module-level MPP extraction has been widely recognized to yield maximum power output under non-uniform irradiance distribution but a consensus on the means and related restrictions has not been reached.

3.2 Structure of Distributed DC-DC Systems

Distributed MPP-tracking systems are the first part in a two-stage conversion, where the dc power produced by the PV module is interfaced into the ac utility grid by means of an inverter. The two-stage structure contains, therefore, a high-voltage dc link between the module-integrated dc-dc converters and the inverter. Most of the published papers are focused either on the design of dc-dc converters in terms of obtaining high operational efficiency or on control issues, i.e., how to implement MPP-tracking and control of the converter. The general structures of DMPPT systems are presented in Figs. 3.1a and 3.1b, depicting series configuration and parallel configuration, respectively.

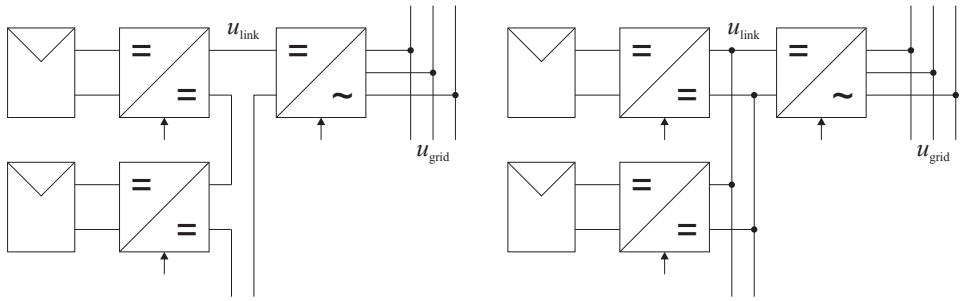

(a) Series configuration. **(b)** Parallel configuration.

Fig. 3.1. DMPPT system configurations.

Quite a number of papers also address the control of the dc link, which itself is of utmost importance in the design process of the entire system. Some of these papers, e.g., (Linares et al., 2009; Poshtkouhi et al., 2010) discuss a concept, in which the grid-connected inverter regulates the dc link current, i.e., its own input current. Thus, the dc link voltage control has to be provided by the dc-dc converters. Theoretically, this could be achieved by utilizing output-voltage controlled converters, resulting in constant-voltage behavior of the converter output terminals. According to circuit theory, the series connection of output-voltage controlled converters is valid and can be interfaced into a current sink, represented by the input-current controlled inverter. However, with a PV generator as the feeding source, output-side control cannot be applied without compromising the system stability, as discussed in detail in Chapter 2, leading to mandatory input-voltage control for the inverter.

Due to above-mentioned reasons, the only viable scheme to provide power transfer to the grid is to utilize an inverter with a cascaded control scheme. The cascaded control scheme is implemented with input-voltage control as the outer loop and grid current control as the inner loop. Thus, the input-voltage controller provides a reference value for the grid current (Puukko et al., 2011). If the power fed to the inverter increases, the

input voltage of the inverter (i.e., the voltage of the dc link) increases, which results in increased grid current reference. Likewise, decreasing input power to the inverter results in decrease in the dc link voltage, and the input-voltage controller responds by lowering the reference value for the grid current. Therefore, the dc link behaves as counter-voltage, or a constant-voltage-type load, requiring the feeding source to behave as a current-source to fulfill circuit theory.

A distinctive aspect in the behavior of the dc link voltage is related to the power injection into the ac grid. As the inverter feeds sinusoidal current (i_{ac}) into the grid, whose voltage (u_{ac}) is naturally also sinusoidal, the instantaneous power fed into the grid (p_{ac}) follows squared sinusoidal form according to (3.1).

$$p_{\mathrm{ac}} = i_{\mathrm{ac}} u_{\mathrm{ac}} = \mathrm{I}\sin(\omega t)\mathrm{U}\sin(\omega t) = \mathrm{UI}\sin^2(\omega t) = \frac{\mathrm{UI}}{2}\left(1 - \cos(2\omega t)\right). \tag{3.1}$$

Therefore, for single-phase inverter the dc link voltage fluctuates at twice the grid frequency, i.e., at 100 Hz or at 120 Hz, whereas for three-phase systems the fluctuation occurs at six times the grid frequency, at 300 Hz or at 360 Hz. This voltage fluctuation cannot be eliminated by increasing the control bandwidth of the input-voltage loop of the inverter, as this will result in contamination of the grid current. Furthermore, to provide maximum power extraction out of the PV modules, this fluctuation should not be transferred into the module terminal, as fluctuation around the MPP lowers the energy yield (Kjaer et al., 2005). A simple solution to minimize the fluctuation of PV terminal voltage caused by grid power fluctuation, is to increase the size of energy buffers between conversion stages, i.e., to increase the input capacitance for each converter. This solution might result in relatively high capacitance values (shown e.g. by Choi and Lai (2010)), increasing the system cost and lowering the reliability, because electrolytic capacitors have to be used (Petrone et al., 2008). Implementing an input-voltage control for module-level converters with a high enough bandwidth effectively eliminates the PV module voltage fluctuation.

The obvious goal in DMPPT systems is to obtain high-efficiency system that maximizes the energy yield of each PV module, regardless of the system configuration or environmental conditions. In the following, the properties and behavior of series and parallel configurations are discussed in detail.

3.2.1 Series-Connected DMPPT System

A widely discussed system configuration comprises dc-dc converters, whose output terminals are connected electrically in series, and the resulting series connection is further connected directly to the input terminal of the inverter. The converters proposed for series configuration are mainly based on non-isolated topologies, which are intended to

operate with low conversion ratio, i.e., the ratio of output and input voltages is close to unity. As the voltage level of a commercial PV module stays at less than 50 volts, the power processing with a non-isolated converter is performed at low voltage levels. It is a well-known issue that switching components with low voltage ratings provide superior performance compared to high-voltage components. Therefore, it would be obvious to assume that the low-voltage module-integrated converters provide high system efficiency. (Bratcu et al., 2011; Kim et al., 2010; Walker and Pierce, 2006; Walker and Sernia, 2004)

It is also claimed that the series configuration provides flexible system design and high modularity, because additional PV modules with interfacing converters can easily be added to the existing system. When the system is expanded with additional components, however, the optimization of each converter is lost. The conversion efficiency of a switched-mode converter can be fully optimized, if the operating conditions are maintained as constant as possible, i.e., if there is only a slight variation in the input voltage or in the output voltage. By narrowing the allowed variation of terminal voltages, component selection can be optimized to yield best performance. However, to optimize the converters operating in series configuration, the number of converters in series has to be constant, to obtain constant dc link distribution among the converters. Adding more converters in the system will, therefore, ruin the optimization based on defined voltage levels. (Liu et al., 2011)

There is, however, a significant restriction in the operation of series-connected converters: Because the output voltage of these converters cannot be controlled, there is no mechanism that would maintain the individual output terminal voltages at constant value. By assuming the dc link voltage to be constant, the output voltage distribution among series-connected converters is dictated by the power levels that each converter is supplying, as discussed, e.g., by Bratcu et al. (2011). In other words, assuming ideal operating conditions (i.e., $P_{\mathrm{in}} = P_{\mathrm{out}}$), the output voltage U_{o} of converter i is defined by

$$U_{\mathrm{o,i}} = \frac{P_{\mathrm{pv,i}}}{\Sigma P_{\mathrm{pv,i}}} U_{\mathrm{link}}, \tag{3.2}$$

where $P_{\mathrm{pv,i}}$ is the power delivered by converter i, $\Sigma P_{\mathrm{pv,i}}$ is the total power delivered by all converter in series configuration and U_{link} is the dc link voltage. Thus, if each converter supplies equal power, then each converter must have equal output voltage (Siri and Willhoff, 2011), because the output current is the same.

Clearly, if the system is affected by partial shading, where the output power of certain converters will drop, there will be an imbalance in the output voltage distribution. Depending on the system configuration, this imbalance may be severe, requiring adequate measures to be taken in the converter design. As an example, a single phase system having dc link voltage of 350 V cannot be safely implemented with module-integrated

converters rated to operate at voltage levels below 50 V. Therefore, high-voltage devices have to be used, lowering the conversion efficiency, which eventually diminishes the aimed benefits of series configuration.

Moreover, the performance of a series configuration is dictated by the actual implementation of the converters, i.e., by the utilized converter topology. The three main types of non-isolated converters used in DMPPT applications are depicted in Fig. 3.2: A voltage step-down converter (Fig. 3.2a), requiring the input voltage to be equal or higher than the output voltage, a voltage step-up converter (Fig. 3.2b), whose output voltage has to be higher than the input voltage and, finally, a converter that is capable of delivering power to the output regardless of the ratio of input and output voltages (Fig. 3.2c).

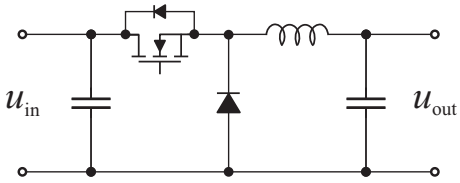

(a) A voltage step-down (buck) converter.

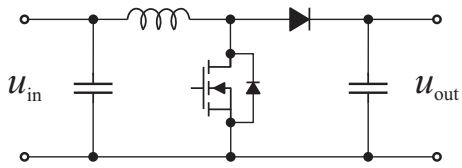

(b) A voltage step-up (boost) converter.

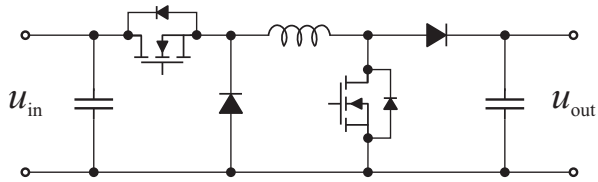

(c) A voltage step-up-and-down (buck-boost) converter.

Fig. 3.2. Three main non-isolated converters utilized in DMPPT systems.

If a DMPPT system comprises voltage step-up converters, controlled power transfer from input to output requires the output voltage to be higher than the input voltage. During daytime operation, if the power generated by the PV module falls down, but the MPP voltage still occurs close to nominal value (see Fig. 1.6b), the output voltage of the converter may fall to lower value than the input voltage. In such case, the operation of the converter is disrupted, resulting in loss of produced power as the converter is unable to deliver power to the dc link. An excellent example of such situation is presented by Kadri et al. (2012). Similarly, by utilizing voltage step-down converters, there might easily emerge similar disruptions, as the changing output voltage distribution impedes the power transfer in the system. Although the converters in Fig. 3.2a and 3.2b can be realized with high efficiency due to low number of power-processing components, converters capable of operating under previously mentioned situations (i.e., voltage step-up-and-down) are favored in many publications, although they are noted to be at an efficiency disadvantage

(Bergveld et al., 2011; Deline et al., 2011; Linares et al., 2009). However, commercial solutions with voltage step-up-and-down properties are in the market, with very high claimed efficiencies (Solaredge, 2012).

A common method to solve the above-mentioned operational problems caused by violation of the conversion ratio, is to implement bypass diodes for each series-connected dc-dc converter. These bypass diodes are either intentionally inserted into the converter shown e.g. by Femia et al. (2008); Linares et al. (2009); Posthkouhi et al. (2011) or by utilizing switching devices that contain inherent bypass diodes. For example, converters shown in Figs. 3.2b and 3.2c have MOSFET-type switches having so-called body diodes, originating from the properties of the semiconductor junction. The bypass action is activated, if the conversion ratio of the converter is violated, i.e. if the converter is unable to support the dc link current. When active, the bypass diode prevents power extraction out of the corresponding PV module, as described by Kadri et al. (2012) and Vighetti et al. (2012). This is an undesired property, as all available power should be utilized.

Generation Control Circuit

A solution to overcome the uneven voltage distribution in series-connected system was first proposed by Shimizu et al. (2001), utilizing so-called generation control circuit (GCC). The operational principle is based on a dedicated dc-dc converter per each PV module that scales the dc link voltage down to the module terminals, thus forcing the module operation point to the defined voltage.

Shimizu et. al. proposed two different configurations: The first contains a single, isolated converter delivering equal voltages to module terminals (Fig. 3.3a). This approach is simple, as the control of the system is done at the isolated converter that can be integrated into the grid-connected inverter. Evident downside is the inability to provide different voltage levels at module terminals, thus making it impossible to maximize energy yield. The second approach takes one step further with implementation of multi-stage dc-dc converters between module terminals (Fig. 3.3b). By increasing the number of controllable dc-dc converters, the aim is to enable improved control of module voltages. However, to effectively adjust the module voltages independently, the system requires complex control and measuring structures, increasing cost and complexity. Furthermore, the sum of module voltages must match the dc link voltage, which is why arbitrary module voltages cannot be obtained (Kim et al., 2010; Orduz et al., n.d.).

More elaborate solutions have been proposed later, where so-called 'shuffle' or 'bypass' dc-dc converters are utilized to change the voltage distribution between series-connected PV modules (Bergveld et al., 2011; Walker and Pierce, 2006). In both solutions, the bypass action is intended to be used only when needed, i.e., when partial shading conditions occur, aiming to reduce the energy loss by processing power only at request. An

application-specific integrated circuit was presented by Bergveld et al. (2011), with which the bypass converter can be easily implemented and integrated into the PV module itself. Although the presented results are decent, the actual voltage distribution dictated by the dc link voltage cannot be solved by these arrangements. Therefore, if majority of PV modules are plagued by partial shading, it may not be possible to force the module voltages to a low enough value as the dc link voltage has to be met.

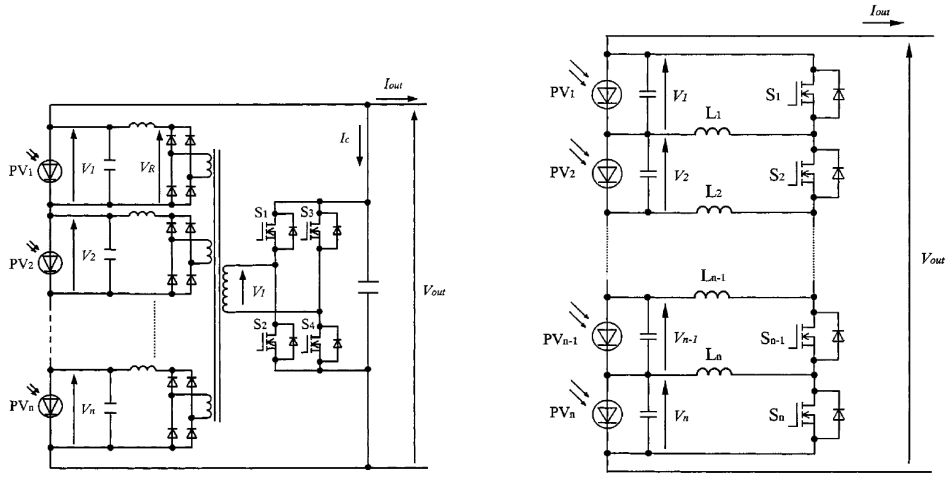

(a) Central dc-dc converter. **(b)** Multi-stage converters.

Fig. 3.3. Generation control circuits according to (Shimizu et al., 2001).

The concept of GCC was further improved by introducing voltage-balancing structures into series connection of dc-dc converters. As previously noted, in a string of series-connected PV module the sum of individual module voltages is bound to the dc link voltage. Additionally, it was addressed previously that the design requirements for series-connected dc-dc converters without output-side control have to be conservative to prevent accidental breakdowns. Both of these restrictions are conveniently dealt with by structures balancing the output voltages of dc-dc converters, such as the string current diverter structure presented, e.g., by Kadri et al. (2012), which is based on the GCC concept.

When the output voltages of dc-dc converters are balanced, significant performance improvements are obtained. Firstly, due to balanced voltages, the design of the converters can be optimized, which increases the power conversion efficiency. Secondly, the voltage balancing structure allows any type of PV modules to be used, without having effect on the system performance. Thirdly, the increase in system complexity is rather low, because a simple open-loop control is sufficient for the balancing structure. It can be concluded, therefore, that the series DMPPT configuration obtains best performance, when there are module-wise dc-dc converters, whose output voltages are balanced.

3.2.2 Parallel-Connected DMPPT System

Another candidate for DMPPT system is the parallel configuration, in which the module-integrated dc-dc converters have their output terminals connected electrically in parallel with the input terminal of a grid-connected inverter. According to the published papers, the parallel configuration is less favored solution, mainly due to assumptions of low conversion efficiency, complex implementation and low performance. However, with the following discussion supported by examples, the feasibility of the parallel configuration may be actually claimed to surpass that of the series configuration.

The parallel configuration, as previously described, requires very high conversion ratio to enable power transfer from a PV module into the inverter. This requirement can either be met with non-isolated converters that are typically based on consecutive conversion stages, or with isolated converters that are well-known and widely implemented in the field of power electronics. It is obvious that the higher the count of components processing power, the lower the overall conversion efficiency. Typically, non-isolated converters with relatively low conversion ratio obtain efficiencies as high as 95 to 98 percent depending, e.g., on the applied converter topology and power level. Recent research results have proved that by careful design, the conversion efficiency for non-isolated, high-conversion-ratio converters can reach above 95 % at power levels of interest (Hsieh et al., n.d.; Li and He, 2011). Similarly, the proposed isolated converters for DMPPT systems have been found to yield efficiencies of greater than 96 % (Choi and Lai, 2010; Liang et al., 2011; Liu et al., 2008). Therefore, the argument of impractically low efficiency as stated, e.g., by Bergveld et al. (2011); Bratcu et al. (2011); Walker and Sernia (2004) is questionable and certainly not sufficient for leaving the parallel configuration out of consideration.

Contrary to the series configuration, the parallel configuration does not experience similar operational disadvantage related to output voltage distribution (Kim et al., 2010). Due to parallel connection, the output voltage is equal to all converters at all times and it is maintained at a constant level by the input-voltage loop of the inverter. Naturally, the dc link voltage contains fluctuation according to (3.1), yet this has negligible effect on the operation of the dc-dc converters. In terms of circuit theory, the inverter acts as a constant-voltage-type load for the converters, effectively turning the output terminals of dc-dc converters into current sources to satisfy the concept of duality, as will be discussed later in this chapter. Thus, each parallel-connected converter supplies current to the dc link, proportional to its output power (defined by the input power). Due to the practical realization of high-conversion-ratio converters, there is always a diode (similar to converter in Fig. 3.2b), or a diode rectifier bridge at the output terminal of the converter, preventing reverse current flow. This, in turn, protects the converters from becoming current sinks. Moreover, no additional protective measures, like the implementation of bypass diodes in series configuration, need to be taken.

An analysis of operational differences of series and parallel configurations is presented by Kim et al. (2010). The authors use extensive simulations to verify the system robustness under various disturbances, such as converter breakdowns or disconnections from the system. Despite the fact that there are authors (e.g., Deline et al. (2011); Liang et al. (2011); Liu et al. (2011)) correctly pointing out the advantages of parallel configuration, the series configuration is widely seen as a better alternative.

Comparison Between Series and Parallel Configurations

To summarize the most important differences between the two system configurations, a short comparison is presented. The considered issues are based on published research results, although there are other issues dictating the overall system feasibility and performance as well, such as manufacturing and maintenance costs, for example. However, to provide the reader with a clear overview on these configurations, only the most relevant issues are discussed.

- Conversion efficiency: The series configuration is claimed to yield better converter-level conversion efficiency due to lower conversion ratio. Partial shading conditions result in imbalance in converter output voltages, forcing some converters to operate at undesired conversion ratios. Each series-connected converter has to be, therefore, designed to endure significant over-voltages at the output terminal, effectively resulting in similar structural solutions or component selections than in parallel-connected converters. If converters with low conversion ratio are used, a voltage-balancing circuit must be applied. Therefore, to obtain decent performance with series configuration, increased power losses have to be accepted. Thus, the total system efficiency between series and parallel configurations may be very close to equal, especially if novel high-efficiency, high-conversion-ratio converters are utilized.

- System performance: According to published results, in a series configuration a misbehaving converter or PV module is bypassed, resulting in loss of produced power. On the other hand, in parallel configuration all converters are able to deliver power to the common dc link regardless of the power level. Respectively, parallel configuration allows any type of PV modules with any orientation to be installed and added to the system. In series configuration, only by adding the balancing network similar changes are allowed to be made.

- Implementation and modularity: In parallel configuration, additional units comprising a PV module and an interfacing dc-dc converter can be freely added or subtracted from the system, as long as the grid-connected inverter is able to handle the changed power level. The series configuration, however, is difficult to be

optimized if changes in the number of PV modules are made. Further, due to the balancing network, the series configuration is inherently more complex as the balancing network requires a controller and additional converters added to each PV module. The parallel configuration is virtually a plug & play system, where each dc-dc converter operates independently.

- Safety and fault tolerance: Both configurations have high-voltage dc link, which is not favored because the protection (i.e., circuit breakers) is more expensive and difficult to implement than for high-voltage ac systems. On the other hand, a failure in a single dc-dc converter in parallel configuration results merely in loss of power generated by corresponding PV module, unless the converter short-circuits the dc link. In series configuration, a failure in a dc-dc converter might compromise the operation of the entire system, if the series connection is broken. It should be noted that if the dc-link is disconnected at the inverter input terminal or if the inverter itself fails, both system configurations might experience destructive over-voltages, resulting in complete loss of produced power, if proper countermeasures are not taken.

On the basis of the presented comparison, the parallel configuration is easier to implement and expand, also it should provide nearly equal power conversion efficiency. However, economic aspects have not been thoroughly discussed in the open literature. Minimizing the cost per produced unit of energy is the ultimate goal. As a summary it can be concluded that extensive and long-lasting field experiments with different system configurations are the only way to find whether the series configuration prevails over the parallel one in the amount of extracted power.

3.3 Distributed DC-AC Conversion

The detrimental effects of partial shading in a system with multiple PV modules can be overcome also by connecting a module-integrated inverter (MIC) to each module. The general concept is to implement a grid-connected low-power inverter directly at the PV module, thus allowing direct connection to the utility grid at the module. Therefore, each MIC operates in parallel with the grid, and module-level MPP-tracking can be guaranteed since the operation of MICs are not affected by nearby modules. Additional benefits of MICs are the absence of high-voltage dc wiring, which improves the system fault tolerance (Sahan et al., 2008) and the possibility to use any type of PV modules with arbitrary module orientation, maximizing the system energy yield. (Deline et al., 2011; Myrzik and Calais, 2003; Wills et al., 1996)

However, there are some disadvantageous properties inherent to MICs, which may well explain why there has not been a wide breakthrough in the installed MIC capacity. Firstly,

the efficiency of an MIC is lower than that of a high-power grid-connected inverter due to two-stage power processing, where the first conversion stage generates most of the power loss. Secondly, as the MIC has to provide MPP-tracking for the PV module, grid current control for undistorted interfacing as well as to contain safety features for anti-islanding operation, the system is complex and the cost per produced watt is high (Liu et al., 2011). A third issue is the low reliability of MICs addressed, e.g., by Sahan et al. (2008). On the other hand, Deline et al. (2011) correctly point out that the actual performance of MICs compared to traditional inverters is an open question, until lifetime results from the field are obtained.

The most significant drawback of MICs is the high cost of produced energy (Norton et al., 2011). A thorough discussion on economic aspects of different PV system configurations with either string inverters, central inverters or MICs is presented by James et al. (2006), contradicting the claimed benefits of the MIC concept. Because the control circuitry of an inverter is essentially the same regardless of the rated power level, it is evident that the price per produced watt falls down as the rated power level of the inverter rises (Fig. 3.4). Therefore, low-power MICs can only beat the high-power inverters in PV systems that are plagued by significant shading problems.

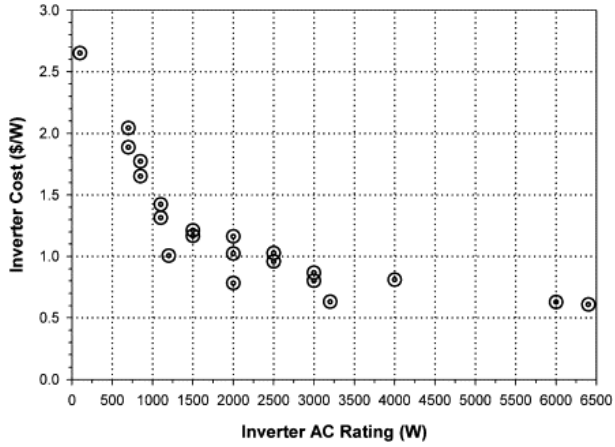

Fig. 3.4. The cost per produced watt for commercial inverters according to James et al. (2006).

A conceptual diagram of an MIC is presented in Fig. 3.5, revealing the two-stage structure of the system. Two-stage conversion is required due to low voltage level (u_{pv}) at which the PV module operates. Therefore, to provide undistorted current into the ac grid, i.e., a sufficiently high dc link voltage, a voltage-boosting stage has to be implemented. The second stage, the actual inverter, provides an interface between the high-voltage dc (u_{link}) and the utility grid (u_{grid}). Conventionally, MICs are designed only for single-phase grid connection due to low power level.

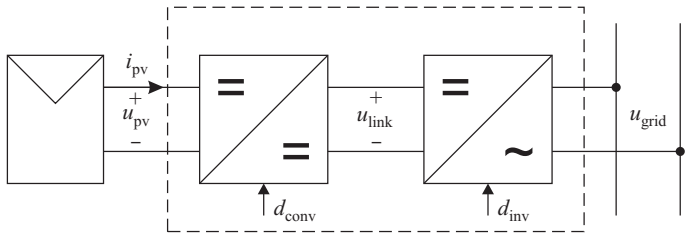

Fig. 3.5. The concept of module-integrated inverter.

An excellent review on different proposed circuit structures for MICs is given by Kjaer et al. (2005). A vast majority of the proposed converters contain a high-frequency transformer, with which the necessary voltage boosting is achieved. This solution provides galvanic isolation at the same time. If isolation is not required, dc-dc converters with very high conversion ratio can be utilized. These approaches are typically based on consecutive conversion stages, such as converters with quadratic voltage conversion ratio (Li and He, 2011).

There are two main concepts for performing the conversion from dc to ac: The first utilizes a so-called pseudo-dc link, whereas the second utilizes an actual high-voltage dc link. In pseudo-dc system, the dc-dc conversion stage is modulated in such a way that the dc link current follows a full-wave rectified sine wave, synchronized to the ac grid voltage. Thus, the task of the inverter stage is to merely 'unfold' the rectified sinusoidal current fed by the dc-dc stage into ac grid current. This approach is beneficial as the unfolder switches operate at line frequency, thereby reducing the power loss caused by switching events. The second approach relies on high-voltage dc link, where the dc voltage remains roughly at the specified level for a conventional inverter. Therefore, high-frequency switching is mandatory, reducing the efficiency of the inverter stage.

3.4 Constraints in Photovoltaic Interfacing

This section discusses the operation of distributed converter systems in light of fundamental circuit theory, and aims to clarify the reasons for the problems encountered when forming practical systems. Recent research results, as discussed later, provide valuable information on the basis of which the operational constraints are classified in three main parts: i) Terminal constraints, based on the properties of the converter power stage and the nature of the source and the load, ii) Topological constraints, which are based on the voltage levels between the input and output terminals of the converter and, iii) Dynamic constraints, related to the issues of closed-loop stability and the feedback methods. (Huusari and Suntio, 2012c)

3.4.1 Terminal Constraints

The terminal constraints can further be divided into two different categories: Constraints dictating the allowed interfacing connection methods for different types of sources and loads and the converter terminal constraints that consider the actual behavior of the converter terminals under different control schemes or system configurations.

Source and Load Constraints

Switching converters are used to enable power transfer from a certain type of electrical energy source to a certain electrical load. Over the past decades a vast majority of switching converters have been designed to transfer power from a constant (or regulated) voltage source, such as the utility grid or a battery and had the output voltage controlled, thereby assuming current-sink type loads. However, the same approach is not valid in PV systems. In PV applications, the source (i.e., the PV generator) properties cannot be claimed to equal those of a constant voltage source. Instead, the PV generator is more properly treated as a non-ideal current source with limited output voltage, as discussed also by Leppäaho et al. (2011).

Basic circuit theory defines the allowed methods to connect switching converter structures to different loads and sources. According to the circuit theory, a load or a source having constant-voltage characteristics should not be short-circuited as that would result in ideally infinite current that is taken from the source. Instead, the possible connections are made either with a series switch (Fig. 3.6a) or with a shunt switch and a series-connected inductor (Fig. 3.6b) that limits the instantaneous current.

Connecting a capacitor in parallel with an ideal constant-voltage load or source serves no purpose according to circuit theory: The voltage of the capacitor is maintained constant and the capacitor current is always zero, because an ideal source is capable of providing arbitrary current. Respectively, in small-signal sense the parallel connection hides the effect of the capacitor, because the ideally zero impedance of the voltage source shunts the capacitor impedance. In practical applications, however, the non-zero series impedance with voltage sources require the use of a parallel capacitor to enhance the voltage-source properties. The reason why input capacitors are typically drawn in the schematic diagrams of converters fed from a voltage source, is the non-zero series impedance of the voltage source. This practice, however, may lead to false conclusions if basic circuit theory is forgotten.

Respectively, a source or a load having current-source characteristics should not be open-circuited since that would result in infinitely high terminal voltage. Therefore, the allowed interfacing connections to a current source can be made either with a shunt switch (Fig. 3.7a) or with a series switch and a parallel-connected capacitor (Fig. 3.7b),

maintaining path for the source current and thus preventing over-voltage surges. Circuit theory also implies that a series connection of an ideal current source and an inductor would be meaningless: The current of the inductor is maintained constant. Respectively, the impedance of the inductor is neglected because of the ideally infinite impedance of the current source. The terminal constraints actually dictate the switching converter power

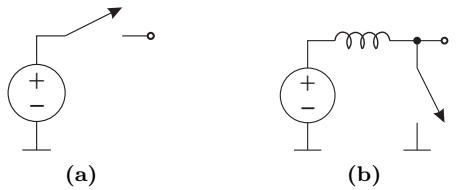

Fig. 3.6. Allowed connections to a voltage-type source or load.

stages that can be used with different configurations of a load and a source. Therefore, the power stages can be designed implicitly when the combination of source and load is known, or by applying a conversion method based on the concept of duality (Leppäaho et al., 2010).

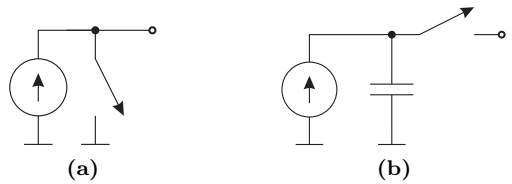

Fig. 3.7. Allowed connections to a current-type source or load.

An excellent example of terminal constraints taken properly into account is given by Leppäaho et al. (2008), as shown in Fig. 3.8:

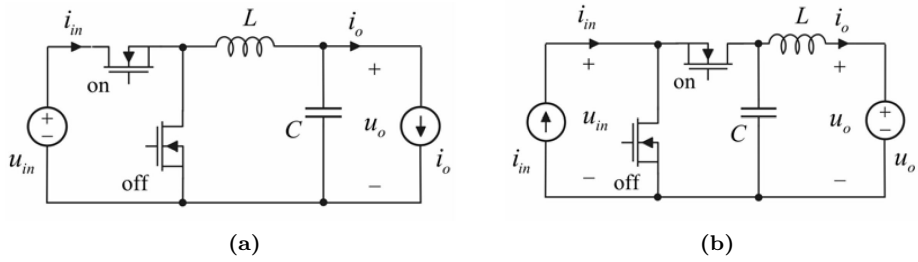

Fig. 3.8. (a) Interfacing a voltage source to a current load and (b) a current source into a voltage-type load (Leppäaho et al., 2008).

Converter Terminal Constraints

The behavior of the input and output terminals of a switching converter are dictated by the nature of the source (i.e., a voltage source or a current source) and the load (a constant-voltage load or a current sink) as well as by the type of feedback, where the point of feedback and the controlled variable play significant roles.

Under conventional output-voltage control, the converter output terminal will behave as constant voltage for the load. Similarly, input-voltage control forces the input terminal to behave as constant-voltage load for the feeding source. The application defines the type of the source and load which, in turn, dictate the controllable variables according to control engineering principles. In other words, if the converter is fed from a constant voltage source, at the input side only the current can be controlled. From a circuit theory point of view this would imply that for each interface, such as the converter input and output terminals, the source and the load at the interface must be duals of each other, i.e., a voltage source must be interfaced to a current sink and vice versa (Fig. 3.9). (Glaser and Witulski, 1994; Huang and Tse, 2007)

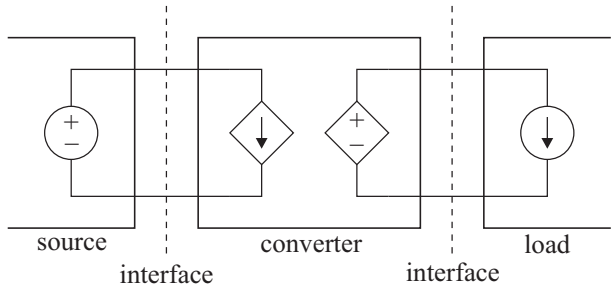

Fig. 3.9. An example of interfaces with dual pairs.

When output-side control is inactive, i.e., either the converter operates in open-loop mode or under input-side control, the output terminal of the converter no longer acts as a voltage source. Instead, the output terminal acts then as a power source and the terminal characteristics are defined solely by the load, i.e., connecting a constant-voltage load will force the output terminal of the converter to act as a current source and vice versa. A resistive load R_L is neither a current-type nor a voltage-type load and, therefore, maintains the converter output terminal as power source, whose output voltage and current are naturally defined as given in (3.3), assuming ideal conditions (i.e., $P_\mathrm{in} = P_\mathrm{out}$).

$$U_\mathrm{o} = \sqrt{P_\mathrm{in} R_\mathrm{L}} \quad , \quad I_\mathrm{o} = \sqrt{\frac{P_\mathrm{in}}{R_\mathrm{L}}}. \tag{3.3}$$

A series connection of distributed MPP-tracking converters under input voltage control will, therefore, essentially be a series connection of power sources and the output

terminal behavior will be dictated by the actual current-voltage characteristics of these power sources. A series connection forces the sources to carry equal current, which makes the terminal voltages of the sources dependent on the output power levels of the converters. If each source supplies equal power, then each source must have equal terminal voltage, according to Siri and Willhoff (2011).

This observation itself will render the series connection of DMPPT converters without any load voltage-sharing circuitry vulnerable to over-voltages at the output terminals, severely limiting the usefulness of the concept in practical PV systems.

3.4.2 Topological Constraints

In order to enable controlled power transfer from input terminal to the output terminal, the topological constraints for a given switching converter must be fulfilled. For example, for a conventional buck converter fed from a constant voltage source, the output voltage must always be less than the input voltage, otherwise the direction of the power transfer will change.

Series-Connected Converters

If a DMPPT system comprises series-connected dc-dc converters without output-side feedback or external control circuitry, the output voltage of each converter is defined by the ratio of the power generated by the corresponding converter to the power generated by the entire system according to (3.2). This phenomenon is well known and widely recognized to be a severe constraint regarding series-connected dc-dc converters (Kadri et al., 2012; Kim et al., 2010; Shimizu et al., 2001) as the design requirements for the converters have to be selected conservatively, thus lowering the conversion efficiency. However, the origin of this phenomenon has not been truly understood.

The measurement results presented by Kadri et al. (2012) clearly show the effect of topological constraints, as the output voltage of the boost converter producing least amount of power in the series connection collapses to zero. According to the power levels of corresponding PV modules, this boost converter should have an output voltage of 1/8 of the dc link voltage (i.e., 25 V), but the input voltage is in the order of 33 V, resulting in violation of topological constraints as the requirements for intended direction of power transfer are not satisfied. A buck-boost type converter would have been able to operate and hence to extract the power of the PV module generating the least amount of power, because the topological constraints are not limiting the direction of power transfer.

Many publications discuss the feasibility of different dc-dc converter topologies such as buck, boost and buck-boost in DMPPT, e.g., (Du and Lu, 2011; Femia et al., 2008; Linares et al., 2009; Roman et al., 2006; Walker and Sernia, 2004; Xiao, Ozog and Dunford, 2007)). In the light of the research performed around this subject, it is reasonable to

conclude that the only viable solution to tackle the topological constraints in a series-connected system without balancing structures, is to utilize buck-boost type converters able to endure high voltages at the output terminal under shaded conditions, where the output voltage is dictated according to (3.2). The primary objective is to achieve the MPP voltage at the PV module terminals regardless of the converter output terminal voltage, as noted e.g. by Balato et al. (2011).

Parallel-Connected Converters

In a system consisting of DMPPT converters in a parallel configuration (Fig. 3.1b), the constant dc bus voltage is applied to the output terminal of each converter. A grid-connected inverter controlling its own input voltage maintains the dc bus voltage at constant value which, in turn, forces the dc-dc converters to act as current sources as explained in Section 3.4.1. Due to the current-source behavior, the parallel connection is well justified and does not contain similar operational constraints as the series-connection. Instead, the converters are able to deliver correct voltage level to the PV modules at all conditions, provided that the converter can reach high enough conversion ratio, i.e., to provide low enough PV module voltage to handle even severe shading conditions.

3.4.3 Dynamic Constraints

The dynamic constraints in DMPPT systems can be categorized into four sections: i) Feedback limitations, arising from the properties of the source and load, which may introduce anomalies in the control loop limiting the operational range of the converter, ii) restrictions related to the Kirchhoff's laws and the controlled variables, iii) cross-coupling restrictions, severely affecting the operation of open-loop MPP-tracking in series configuration, and iv) minor-loop constraint, dictating impedance-based stability of the system.

Feedback Limitations

It has been demonstrated by Leppäaho et al. (2011) that pure output-side feedback in PV applications cannot be implemented without compromising the stability of the interfacing converter due to the inherent properties of the PV generator itself, as discussed also in Chapter 2. As explained in Leppäaho et al. (2011), the maximum power limit introduces a zero in the output-side control transfer function, which will move from left half of the complex plane (LHP) to the right half (RHP) as the maximum power point is crossed over. Therefore, a loop designed to operate on the other side of the maximum power point would become unstable on the other side. The same limitation emerges with any type of source with similar power-limited characteristics, and for this reason the output-side

feedback cannot operate throughout the entire input source current-voltage curve. As a result, converters interfacing a power-limited source, such as PV generators and fuel cells, must utilize input-side control. It should be emphasized that emulating output-power limited sources with near-ideal laboratory supplies effectively hides the true nature of the original sources, and the output-side control constraints would not emerge. A conventional laboratory voltage source, although power limited, does not have distinctive operating regions on both sides of maximum power point and, therefore, may lead to misconclusions when examining practical operation, as shown e.g., in the analysis presented by Hamza et al. (2011).

Circuit Theory Restrictions

Another aspect in dynamic constraints is the set of restrictions arising from the Kirchhoff's current and voltage laws. For a converter interfacing a PV generator with input-current control, a situation might easily emerge where the input current reference exceeds the actual PV current, leading to controller saturation and short-circuit at the PV generator terminals (Xiao, Dunford, Palmer and Capel, 2007). In this situation, the controller tries to violate the Kirchhoff's current law. This phenomenon may emerge also if the interfacing converter is designed so that the PV generator current contains significant ripple component. Similarly, the same phenomenon should occur with PV generator voltage feedback according to the PV generator current-voltage curve. However, the PV terminal voltage stays relatively constant under even illumination and is more a function of the module temperature. Moreover, the issue with high PV terminal voltage ripple is rarely encountered due to the power stage configuration and input capacitor selection leading to almost negligible PV terminal voltage ripple. Typically there is a relatively large capacitor connected at the input of the interfacing converter, followed by an inductor, which lower the high-frequency ripple voltage at the terminal.

The final conclusion regarding restrictions introduced by the circuit laws is that if duality exists at a certain interface (i.e., a voltage source is interfaced to a current source or vice versa), then the circuit laws are automatically satisfied and stable operation is guaranteed. On the other hand, if duality is violated (i.e., the control circuitry operates in a manner that contradicts circuit laws), the system operation is forced away from the stable operating point. In practical PV systems, a violation in interface duality might result in unintentional short-circuit of the PV generator, as discussed with practical verification by Suntio, Huusari and Leppäaho (2010).

Cross-Coupling Restrictions

The third dynamic constraint is related to cross-couplings between DMPPT converters. As presented in Chapter 2, in series configuration there are cross-couplings between in-

dividual dc-dc converters, caused by the structure of the system. These cross-couplings imply that open-loop operation of series-connected DMPPT converters is prone to disturbances, reducing the extracted power. This disadvantage is a consequence of undefined converter output voltages and can be solved either by applying input-voltage control (i.e., closed-loop operation) or by applying balancing structures that effectively decouple individual converters from each other. Chapter 4 provides supporting experimental evidence for these claims.

Minor-Loop Constraint

The fourth dynamic constraint is defined by the minor-loop gain concept, discussed in Chapter 2. Designing a high-performance PV system requires that the impedance behavior at all relevant interfaces is examined. Let us consider a practical situation, where an interfacing converter is operated at open loop, to verify the power conversion efficiency. It would be reasonable to assume that the input power can be taken from any type of power source, as long as correct voltage and current levels are obtained. However, depending on the minor-loop gain between the source and the converter, the system may be open-loop unstable, thus ruining the verification process. Chapter 4 presents practical evidence of an open-loop unstable system.

3.5 Conclusions

This chapter discussed the operation and properties of series-connected and parallel-connected DMPPT systems. It was concluded that although otherwise claimed, the parallel configuration contains indisputable benefits not achievable by series configuration. Moreover, it was shown that the conversion efficiency in parallel configuration, which is frequently seen as the main drawback, actually is not a limiting issue. Other considered aspects were related to system configuration and operation, with the conclusion that in terms of expandability and autonomous MPP-tracking, the parallel configuration shows better performance. Yet, it was also concluded that long-lasting field experiments are still needed to reveal the actual behavior and reliability of both configurations. Regardless of these open questions, the parallel configuration provides a better alternative on the basis of presented arguments.

In addition to the performance comparison, this chapter presented the interfacing constraints for DMPPT converters. These constraints can be categorized into different classes, each considering its own branch of practical implementation of DMPPT converters. Based on published research results and fundamental circuit theory, these constraints are intended to aid in understanding the limits and properties of converters interfacing the PV generator.

4 EXPERIMENTAL VERIFICATION

This chapter discusses the experimental verification of the previously presented discussions and findings as well as provides the reader with an overview on the actual measurement setups and instruments used in verification. The measurement results are mainly in frequency domain, as the most important findings are related to frequency-domain phenomena. First, a brief discussion is given on the frequency-domain behavior of the PV generator, with examples supporting the claim that an electronic emulator has to possess similar characteristics than an actual PV generator in order to yield correct performance. For the patented converter (Huusari and Suntio, 2012d), the presented frequency-domain behavior validates the analysis and shows that the impedance and control behavior of the converter indicate good performance in PV applications. On the other hand, for the system of two cascaded buck-boost converters, the measurement results are used to explain the cross-coupling phenomena observed in series configuration of PV interfacing dc-dc converters.

4.1 Measurement System

The frequency-domain measurements were carried out using Venable Instruments' frequency response analyzer (FRA) Model 3120 with an impedance measurement kit. Additionally, an external transformer was used to enable the ground-referenced output of the FRA to be injected to an arbitrary potential, such as the output terminal of the converter under study.

In addition to standard laboratory equipment (i.e., a high-speed oscilloscope, current probes, voltage sources, electronic loads), an important tool used as the input source was the Agilent Solar Array Simulator E4360A (further referred to as SAS_1), which contains two independent and isolated E4361A modules. A single module is capable of providing an output power of 510 W with maximum voltage and current 65 volts and 8.5 amperes, respectively. The modules can be programmed to operate either as current sources with limited output voltage, voltage sources with limited short-circuit current or as source emulating an actual PV generator.

In PV-emulation operation, two different modes can be selected. In *SAS mode*, the user inserts the short-circuit current (I_{sc}), the open-circuit voltage (U_{oc}) and the MPP (I_{mpp} and U_{mpp}), from which the device replicates an IV-curve. In *table mode*, the user

inputs a table with up to 4096 current-voltage pairs and the resulting curve is replicated by the module. The table mode provides a more accurate replication of an actual PV generator, yet both modes yield a behavior that is characteristic to PV generator. As such, both modes can be used to emulate an actual PV generator with sufficient accuracy. The SAS mode was used in the measurements with details representing a 190-W PV module (setup 1) or a 15-W PV module ('nominal', setup 2 and 'shaded', setup 3), according to Table 4.1.

Table 4.1. Details for SAS_1 setups.

	Setup 1	Setup 2	Setup 3
I_{sc} (A)	8.02	1.00	0.50
U_{oc} (V)	33.10	19.00	18.00
I_{mpp} (A)	7.33	0.90	0.45
U_{mpp} (V)	25.90	16.00	15.50

4.1.1 Dynamic Properties of Devices Emulating a PV Generator

The SAS_1 is extremely well suited for this type of testing purposes because the static and dynamic operation matches very well with an actual PV module, as shown by Mäki et al. (2010). The measured static and dynamic characteristics of the SAS_1 are shown in Fig. 4.1: The relationship of the static and dynamic resistances (R_{pv} and r_{pv}) correspond to Fig. 2.11 presented previously.

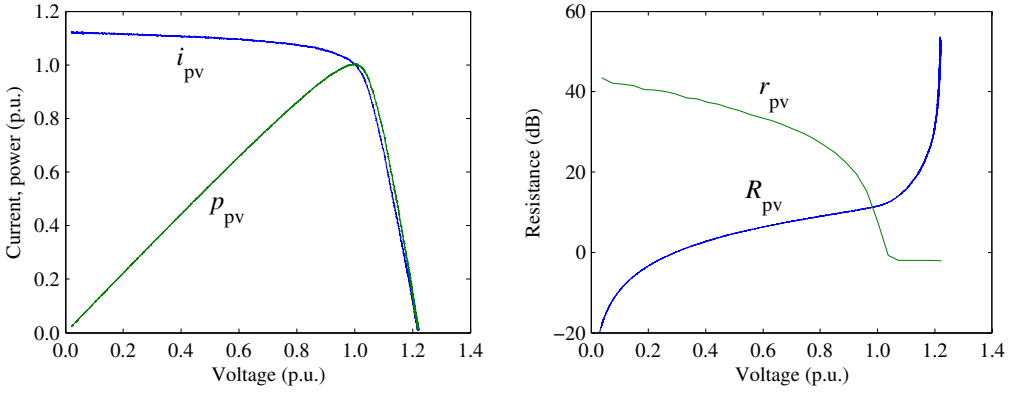

(a) Static characteristics. **(b)** Dynamic characteristics.

Fig. 4.1. Characteristics of E4361A in SAS mode.

If a conventional laboratory voltage source is used as the input source, the output impedance of the source would be very low and, thus, correct dynamic behavior would not be experienced. An excellent example of false conclusions arising from the use of a source not emulating a PV generator is given by Hamza et al. (2011): According to Fig. 5a in the publication, the output impedance of the source is constant over wide frequency range and corresponds to a source resistance of 0.16 ohms, indicating the use of a voltage source with some series resistance. No indication on the operating point is given, yet it is obvious that for an actual PV module the output impedance is neither that low, nor constant. In the publication, an input filter is designed for the interfacing converter and the system stability is studied on the basis of the impedance relationships. Thus, as the source impedance behavior does not equal that of a PV generator, conclusions regarding system stability are not valid in actual application.

The output impedance of the SAS_1 operating with setup 1 is presented in Fig. 4.2 in three different operating points: In the current region (CC, U_{sas} = 10.0 V), in MPP (U_{sas} = 25.9 V) and in voltage region (CV, U_{sas} = 30.0 V). The output impedance varies significantly along the operating point on the IV-curve and, therefore, affects the operation of the interfacing converter.

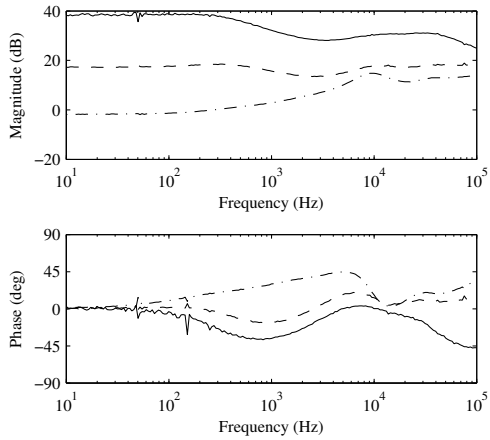

Fig. 4.2. Output impedance of SAS_1 in three different operating points (setup 1): CC (solid line), MPP (dashed line) and CV (dash-dotted line)

For comparison purposes, the output impedances of another commercial solar array simulator (SAS_2) and an actual PV generator were measured. A measurement setup was formed, where 16 halogen lamps illuminated a NAPS NP190GKg module, yielding the characteristic IV-curve shown in Fig. 4.3. The corresponding curve was loaded into SAS_2, resulting in the same static operation.

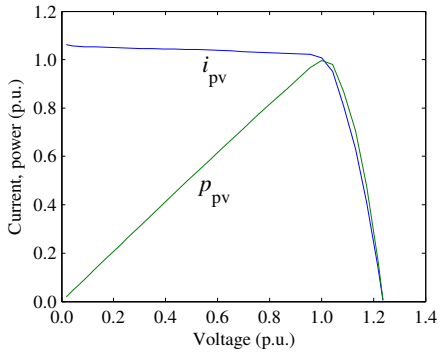

Fig. 4.3. Measured static characteristics of a PV module.

However, the dynamic behavior of the SAS_2 and the actual PV module are quite different, as shown in Fig. 4.4: In current region, the behavior for SAS_2 shows no significant deviation from the actual module. In voltage region, there is a low-frequency resonance, causing anomalous behavior in the phase of the impedance.

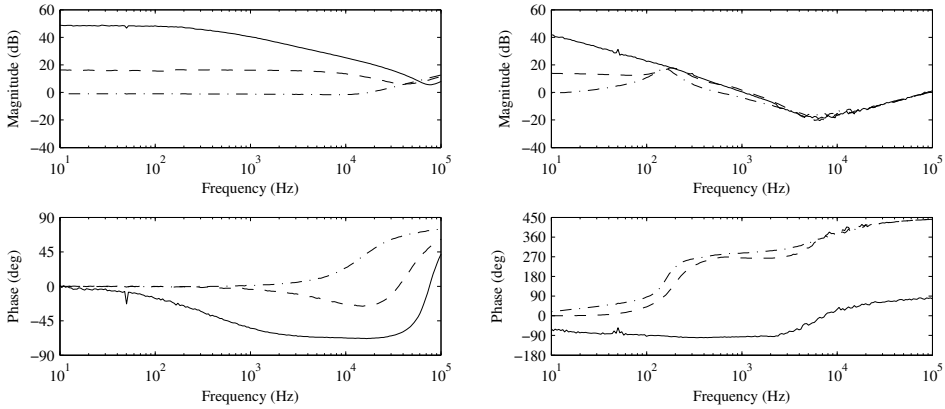

(a) Actual PV module. **(b)** SAS_2.

Fig. 4.4. Dynamic characteristics of SAS_2 and a PV module: CC (solid line), MPP (dashed line) and CV (dash-dotted line).

The detrimental effect of the source impedance on the behavior of an interfacing converter was examined by using a buck-boost type converter operating at open loop. The interfacing converter was used to adapt the SAS_2 into a constant-voltage load of 30 volts. The input impedance of the interfacing converter and the output impedance of SAS_2 in CC and in CV are shown in Fig. 4.5a and the corresponding minor-loop gains in Fig. 4.5b, respectively.

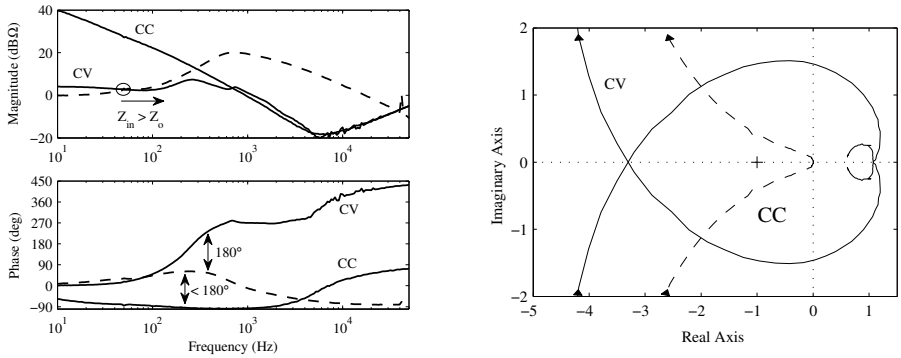

(a) Impedances in frequency domain. **(b)** Corresponding minor-loop gains.

Fig. 4.5. Converter input impedance (dashed line) and SAS_2 output impedances.

According to Fig. 4.5a, the phase difference between the SAS_2 output impedance and the converter input impedance does not reach 180 degrees in current region, indicating that the system is stable. However, the low-frequency resonance within SAS_2 causes significant phase deviation, exceeding 180 degrees in voltage region. In addition, as the magnitude of the input impedance of the converter exceeds the SAS_2 output impedance at low frequencies, conditions for instability exist. The same prediction can be seen from the Nyquist plot in Fig. 4.5b, presenting the minor-loop gain in CC and in CV. The Nyquist plot reveals the instability in CV, as the curve encircles the point (-1,0).

Time-domain behavior of the interfacing buck-boost converter and the SAS_2 is presented in Fig. 4.6, revealing open-loop instability in voltage region. Similar anomalous behavior would not be seen with either an actual PV generator or an emulator having similar characteristics.

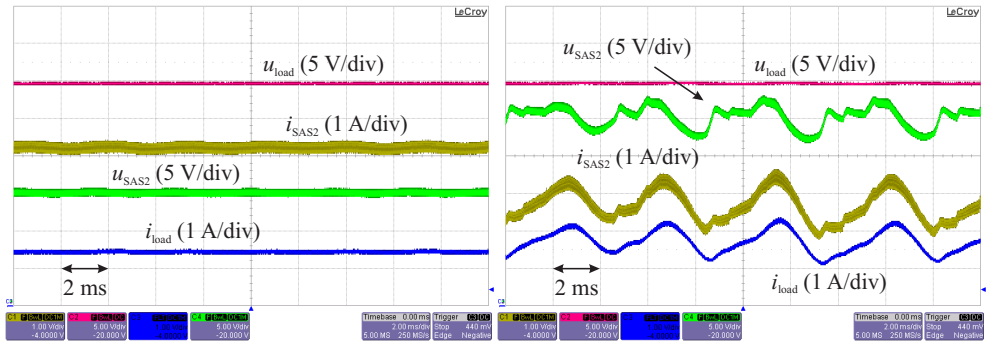

(a) Current region. **(b)** Voltage region.

Fig. 4.6. Time-domain operation of SAS_2 with an open-loop buck-boost converter.

4.2 Current-Fed Quadratic Full-Bridge Buck Converter

The schematic diagram of the patented converter structure is shown in Fig. 2.12, as discussed in Chapter 2. The power stage can be split into individual blocks as follows: The input filter (L_1, C_1), the quadratic element (Maksimovic and Cuk, 1991) (D_1, D_2, C_2, L_2), the main transformer with controllable primary side switches and the voltage-doubler secondary arrangement (D_3, D_4, C_3, C_4) (Leu and Huang, 2010). The output passive network (C_3, C_4, L_3) is a topological part of the power stage, where the purpose of the inductor is to ensure continuous output current. From the theoretical point of view, the input filter is not a mandatory part of the converter and, as such, can be removed. The purpose of the filter is, however, to make the input voltage continuous thus enabling input voltage control.

Time-Domain Measurements

To validate the proposed converter operation, extensive measurements were carried out on the prototype (Huusari and Suntio, 2011a,b). These measurements included static and transient time-domain measurements as well as frequency domain measurements both at open loop and closed loop. The prototype was fed by the SAS_1 and loaded with an electronic load (Elektro-Automatik EA-EL 9400, referred to as EA). Between the prototype and the load there was an additional CL-type filter. An external digital signal controller (DSC) evaluation kit (with Texas Instruments TMS320F28335) was used to implement the control circuitry, where the switching frequency f_s was 200 kHz. The main details of the realized prototype are presented in Table 4.2.

Table 4.2. Main details of the CFQFB prototype.

Element	Value	Element	Details
L_1	18 μH	Main XFR	ETD29, N97
L_2	22 μH	$S_1 - S_4$	FDP2532
L_3	10 μH	D_1, D_2	MBR30H60
C_1, C_2	1000 μF	D_3, D_4	DHG5I600PA
C_3, C_4	33 μF	U_load	350 V
L_M	5.63 mH	Rated power	190 W
N_1/N_2	0.24		

The measured primary-side waveforms of the proposed converter at MPP are given in Fig. 4.7, containing the gate-to-source voltages (Gate A, Gate B) of the primary switches, the main transformer primary current (i_pri) and the primary switch bridge voltage (u_bridge). The applied gate drive scheme is depicted in Fig. 4.7. It is vital to

provide some amount of minimum overlapping time for gate signals to maintain paths for primary inductor currents. Controlling all of the primary switches into non-conducting state would cause destructive overvoltage on the MOSFET switches, as the path for inductor L_2 current is broken.

The prototype was operated from an external auxiliary supply, providing constant supply for the control and gate drive circuitry. For this reason, the main switches continued to operate even if the solar array simulator was turned off. Thus, the energy stored in the magnetic components was safely discharged. In practical applications the converter should be designed to take the auxiliary supply from the dc link, resulting in similar safe shut-down and turn-on operation. There should not be operational problems as long as the auxiliary supply and gate drive are turned on before connecting the PV module (with a relay, for example) and, respectively, by disconnecting the PV module first during shut-down.

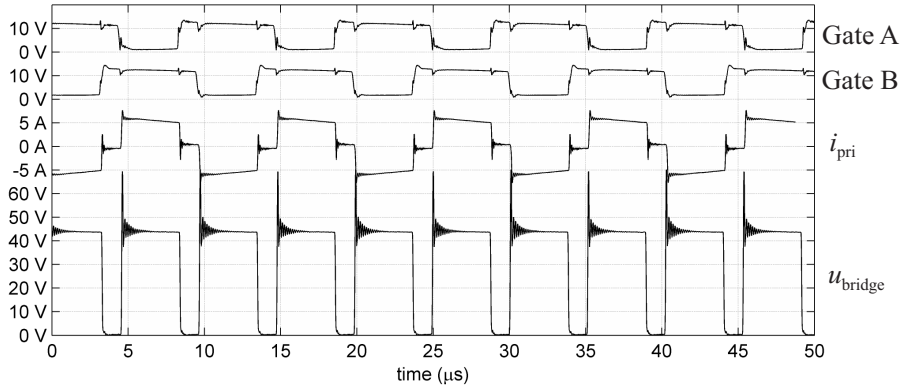

Fig. 4.7. Primary side waveforms at MPP ($D = 0.59$).

The efficiency of the prototype was measured by operating the converter along the SAS_1 IV-curve between 2 and 33 volts. The resulting curve is presented in Fig. 4.8. According to these measurements, the prototype had an efficiency of 92 % at MPP, and the peak efficiency reached 94 %. Moreover, the prototype was able to deliver power to the high-voltage load even at very low input voltages, which would improve the daily energy harvesting in actual application, as maximum power can be extracted even under most severe shading conditions.

Frequency-Domain Measurements

The open-loop measurements were carried out to verify the predicted transfer functions and to investigate the behavior of the transfer functions at different SAS_1 operating

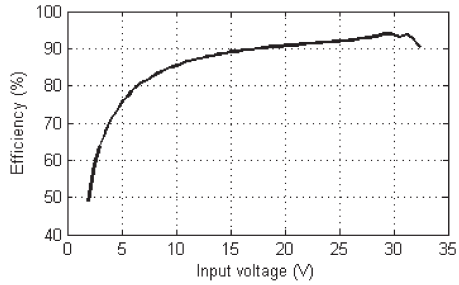

Fig. 4.8. Measured efficiency.

points. The four open-loop transfer functions presented in Figs. 4.9 and 4.10 reveal that the analytical predictions match very well with the experimental results. The inductive high-frequency tail visible in the open-loop input impedance (Fig. 4.9a) results from the measurement setup and corresponds to a small inductance in series with the input terminal of the converter.

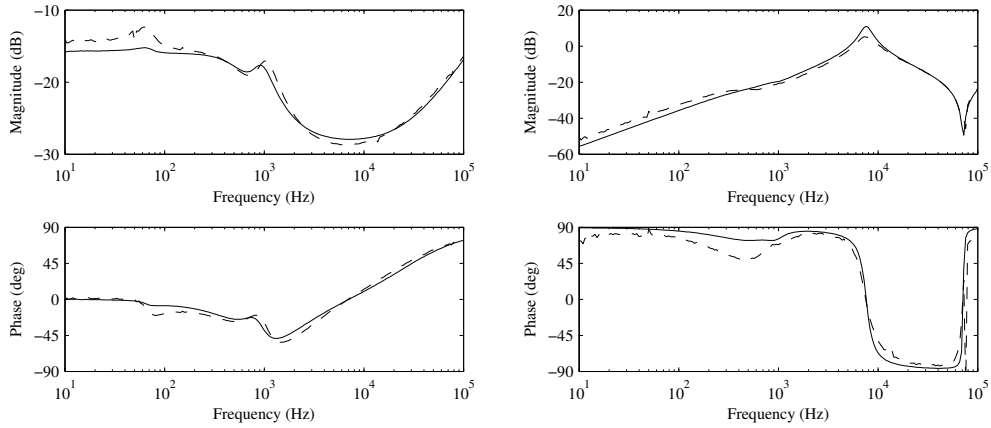

(a) Zin-o. **(b)** Yo-o.

Fig. 4.9. Measured (dashed line) and predicted (solid line) transfer functions at MPP.

The mismatch in the low-frequency behavior of the control-to-output transfer function $G_{\text{co-o}}$ (Fig. 4.10b) indicates that the actual operating point of the measurement has been slightly on the other side of the MPP than the corresponding prediction. This is typical behavior with practical experiments, as it is fairly difficult to operate exactly at the MPP while performing frequency-domain measurements involving continuous perturbation to the operating point.

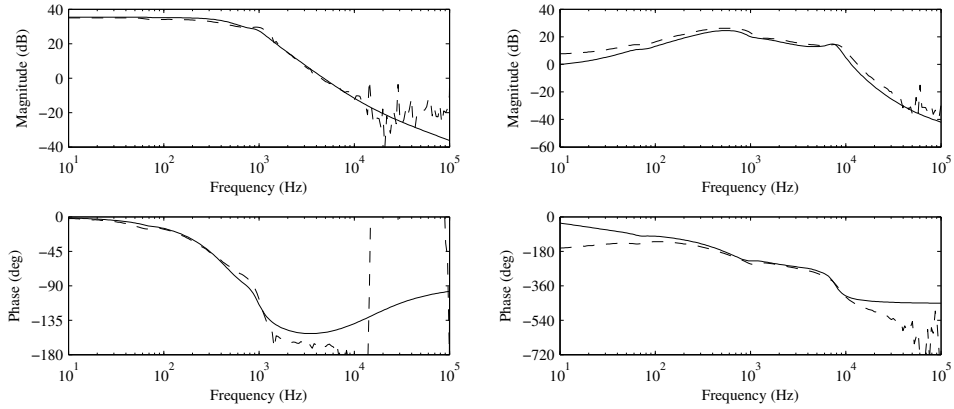

(a) Gci-o. **(b)** Gco-o.

Fig. 4.10. Measured (dashed line) and predicted (solid line) transfer functions at MPP.

Considering the operation on both sides of the MPP, the control transfer functions were measured to support the claim that output-side control for converters interfacing a PV generator is not justified. According to Fig. 4.11, the control-to-input transfer function $G_{\text{ci-o}}$ behaves similarly despite the operating point, whereas in the control-to-output transfer function, a phase shift of 180 degrees is experienced at low frequencies. Thus, it is possible to design a stable output-side control loop, but only in CC or in CV. On the other hand, the input-side control loop is easily designed, as no anomalies exist.

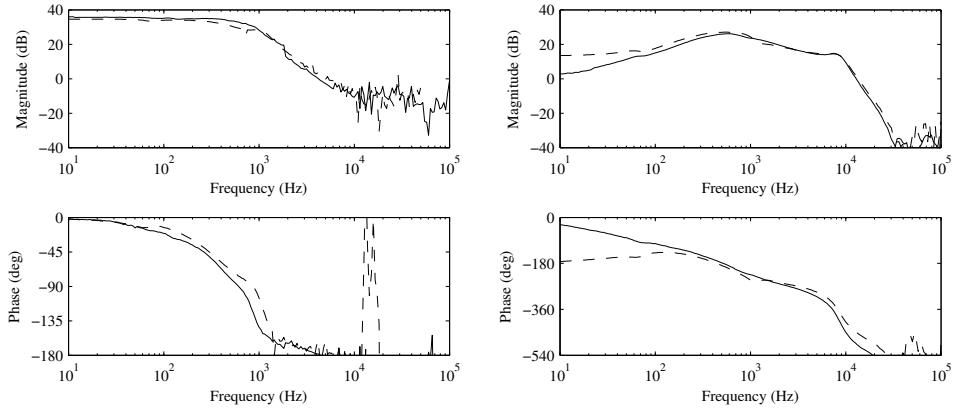

(a) Gci-o. **(b)** Gco-o.

Fig. 4.11. Measured control transfer functions: CC (solid line) and CV (dashed line).

The input-voltage control loop was implemented around the DSC as follows: A PID controller was designed in continuous-time domain and transferred into discrete-time domain by using bilinear transformation. As the analog-to-digital conversion introduces delay within the control loop, a time delay block (4.1) was included within the analytical model according to the first-order Padé approximation, where the sampling time was set to equal the switching period, i.e., $T_\mathrm{d} = T_\mathrm{s} = 5\mu\mathrm{s}$.

$$G_\mathrm{d}(s) = \frac{1 - s\frac{T_\mathrm{s}}{2}}{1 + s\frac{T_\mathrm{s}}{2}}. \tag{4.1}$$

The control bandwidth was designed to be 100 Hz, which is sufficient for the PV generator interfacing due to rather low dynamics of the PV module voltage (Kumar et al., 2006; Mäki et al., 2010; Suntio, Leppäaho, Huusari and Nousiainen, 2010). The discrete-time controller was designed on the basis of the measured $G_\mathrm{ci}(s)$ shown in Fig. 4.10a. The resulting controller is given in (4.2).

$$G_\mathrm{cc}(z) = \frac{5.284z^{-3} - 5.566z^{-2} - 5.280z^{-1} + 5.570}{-0.113z^{-3} + 1.172z^{-2} - 2.059z^{-1}} \cdot 1e^{-3}. \tag{4.2}$$

The measured loop gains at the three operating points are shown in Fig. 4.12a, indicating proper phase margins at all operating points. The crossover frequency varies slightly according to the operating point, yet without compromising the loop robust stability.

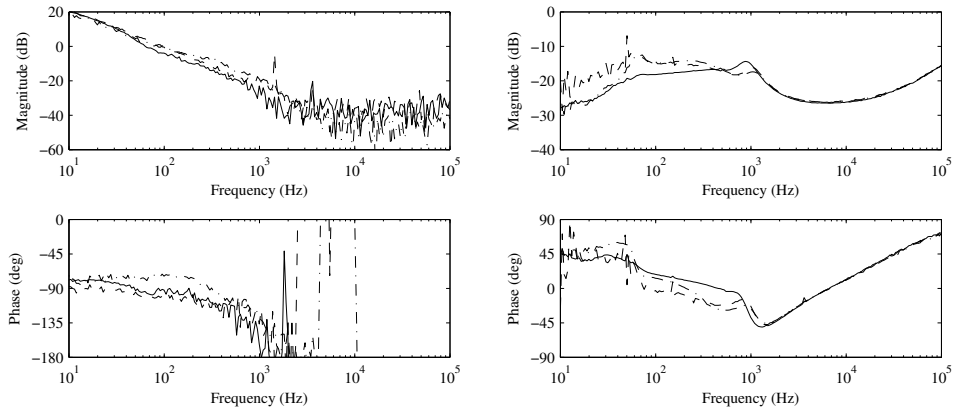

(a) Loop gain. **(b)** Input impedance.

Fig. 4.12. Measured closed-loop transfer functions: CC (solid line) and CV (dashed line).

The closed-loop input impedance is shown in Fig. 4.12b: By comparing the converter

input impedance and the SAS_1 output impedance presented in Fig. 4.2, it can be concluded that violation of Nyquist stability criterion does not take place, because the output impedance of the PV generator is higher than the converter input impedance. The time-domain response of the input voltage control is demonstrated in Figs. 4.13 and 4.14. A triangle-type continuous change was introduced into the digital reference within the source code, resulting in triangle waveform for the input voltage (i.e., the SAS_1 voltage, u_{pv}) between 10 and 30 volts, yielding response in the SAS_1 current (i_{pv}) as shown in Fig. 4.13. (Huusari and Suntio, 2012b)

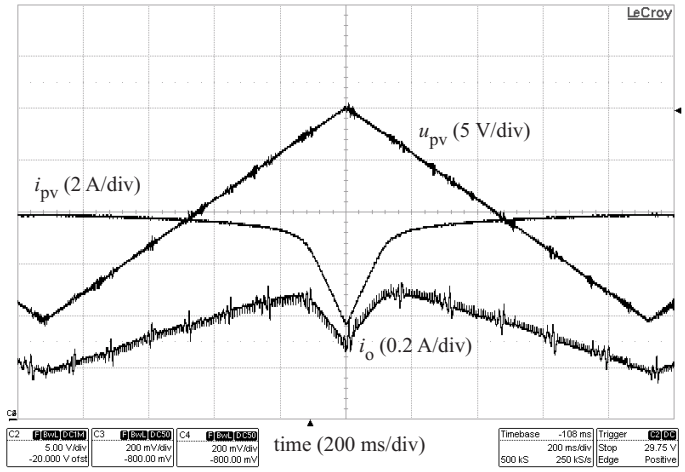

Fig. 4.13. Continuous change in input voltage reference.

The transient response for a step change in input voltage from 10.0 to 25.9 volts (i.e., from CR to the MPP) and back is shown in Fig. 4.14, revealing stable control loop operation. Thus, it can be concluded that the presented converter provides excellent performance in terms of conversion ratio, efficiency and controllability. In addition, according to closed-loop input impedance, there is no violation of Nyquist stability criterion.

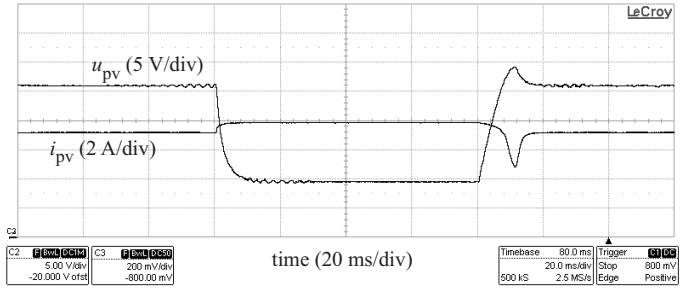

Fig. 4.14. Step change in input voltage reference.

4.3 Cascaded Buck-Boost Converters

The cascade structure with two buck-boost converters was examined by configuring a solar array simulator (Agilent E4360A, 'SAS') modules according to values in Table 4.1. Both converters operated at 100 kHz and were controlled by individual DSCs and the system had a constant-voltage load of 50 volts, realized with EA. The converters were connected in series configuration and in parallel configuration and for both setups, the input cross-coupling and the control cross-coupling transfer functions were measured. Further, time-domain operation of series configuration with individual MPP trackers was examined.

Both buck-boost converters had identical circuit structure, with power stages comprising components presented in Table 4.3.

Table 4.3. Component details in buck-boost converters.

Component	Value	Component	Details
L_1	120 μH	D_1, D_2	SK56C
L_2	100 nH	S_1, S_2	IPD200N15N3
C_1	440 μF		
C_2	33 μF		

4.3.1 Frequency-domain measurements

To verify the predictions presented in Section 2, the corresponding transfer functions for series and parallel configurations were measured using frequency response analyzer. During these measurements, both SAS modules were configured according to setup 2 in Table 4.1.

The measured input cross-coupling transfer functions at open loop ($T_{\text{cr-o}} = \hat{u}_{\text{in1}}/\hat{i}_{\text{inS2}}$, see Fig. 2.19) for series and parallel configurations are presented in Fig. 4.15a and 4.15b, respectively. According to Fig. 4.15, the analytical predictions presented in Chapter 2 are proven valid as the series configuration contains strong cross-coupling at low frequencies. On the basis of Fig. 4.15a, the magnitude of $T_{\text{cr-o}}$ is significant at low frequencies. Thus, the input voltage u_{in1} is strongly affected by changes in input current i_{inS2}, as shown in Fig. 2.26. On the other hand, as indicated by analytical study, the parallel configuration is virtually free of such cross-coupling effects.

The measured control cross-coupling transfer functions at open loop ($G_{\text{cr-o}} = \hat{u}_{\text{in1}}/\hat{c}_2$) for both system configurations are shown in Fig. 4.16. For series configuration this cross-coupling, although weaker than $T_{\text{cr-o}}$, is still significant at low frequencies and, thus,

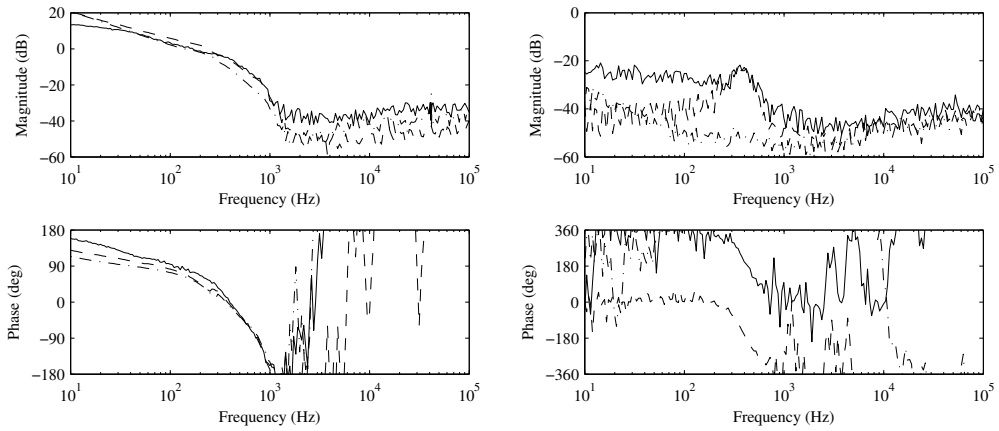

(a) Series configuration. **(b)** Parallel configuration.

Fig. 4.15. Measured $T_{\text{cr-o}}$: CC (solid line), MPP (dashed line) and CV (dash-dotted line).

contributes to experienced disturbances. Respectively, the parallel configuration does not suffer from this cross-coupling. The only visible effect shown between 100 Hz and 1 kHz is due to resonance caused by the components in the power stage, namely C_1 and L_1. Yet, the magnitude remains below -20 dB, indicating very weak cross-coupling at worst case.

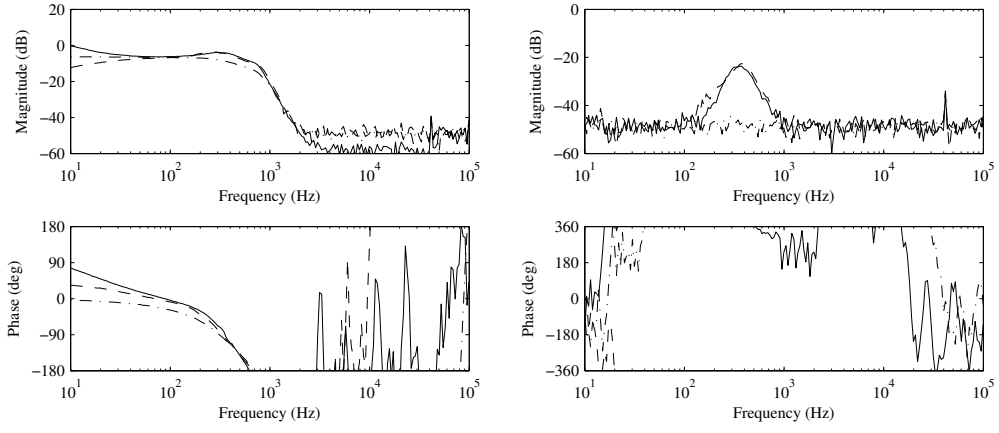

(a) Series configuration. **(b)** Parallel configuration.

Fig. 4.16. Measured $G_{\text{cr-o}}$: CC (solid line), MPP (dashed line) and CV (dash-dotted line).

To investigate the effect of closed-loop control on the performance of series configuration, an input-voltage control loop was designed for the buck-boost converters with a PID-controller presented in (4.3).

$$G_{\mathrm{cc}}(z) = \frac{4.981z^{-3} - 4.374z^{-2} - 4.963z^{-1} + 4.393}{-0.786z^{-3} - 0.370z^{-2} + 0.157z^{-1}}. \tag{4.3}$$

According to Fig. 4.17, the input-voltage control loop effectively reduces the cross-couplings introduced by changes in the input current (Fig. 4.17a) or in the reference (Fig. 4.17b) of the neighboring converter.

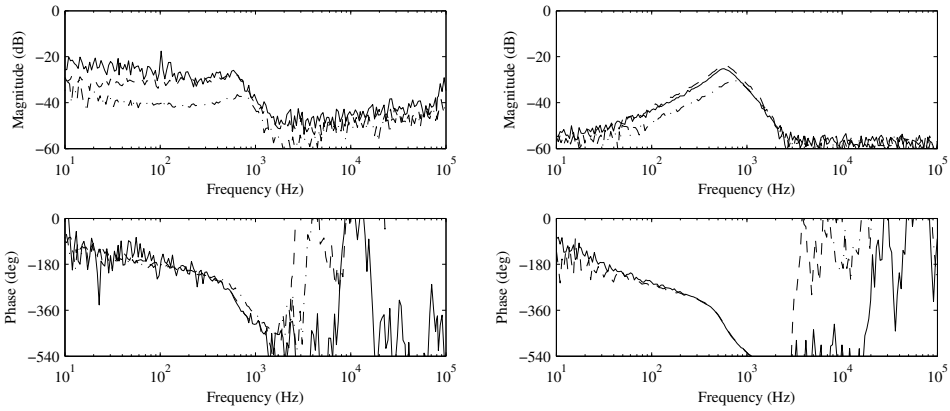

(a) $T_{\text{cr-c}}$. **(b)** $G_{\text{cr-c}}$.

Fig. 4.17. Measured closed-loop cross-couplings for series configuration: CC (solid line), MPP (dashed line) and CV (dash-dotted line).

4.3.2 Time-domain measurements

Individual MPP-tracking algorithms were implemented in series configuration, using perturb & observe method. To examine the system operation under changing environmental conditions, a transient was introduced in the other SAS module, so that the module output varied between setup 2 and setup 3 with a period of 10 seconds. The transient modeled a sudden drop in the irradiance, resulting in the 'shaded' curve described by setup 3.

Figure 4.18 shows the system behavior under transient, when both converters operated at open loop, with the MPP block giving the duty cycle directly to the converters. The examined variables were the input voltages of the converters (i.e., the SAS module output voltages), the output voltage of the converter experiencing the transient at its SAS module

and, finally, the load current delivered to the voltage-type load. Next, the MPP algorithm was added to the closed-loop control scheme, where the MPP block gave reference value for the input voltage control. Similar transient was introduced to the other SAS module and the system operation was verified as previously described.

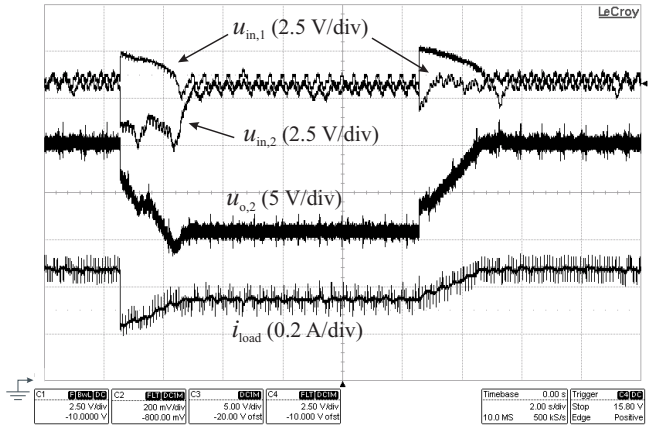

Fig. 4.18. Open-loop MPP-tracking: Transients in other SAS module.

Next, the MPP algorithm was added to the closed-loop control scheme, where the MPP block gave reference value for the input voltage control. Similar transient was introduced to the other SAS module and the system operation was verified as previously described. The results are shown in Figs. 4.19 and 4.20, respectively.

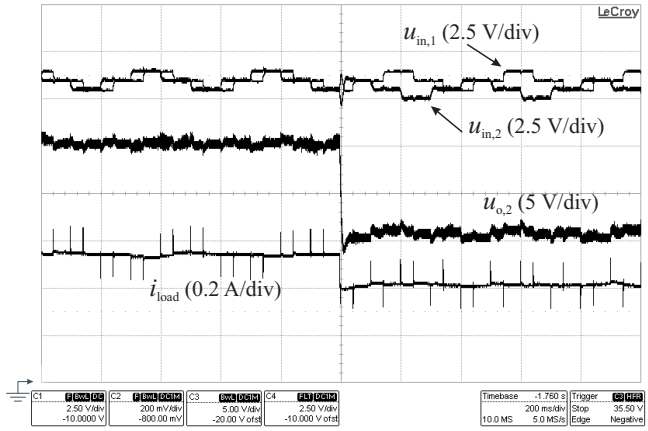

Fig. 4.19. Closed-loop MPP-tracking: Sudden decrease in the output power of the other SAS module.

The presented results validate the simulated predictions given by Petrone et al. (n.d.) and the analytical claims presented in this paper. It can be concluded that input-voltage

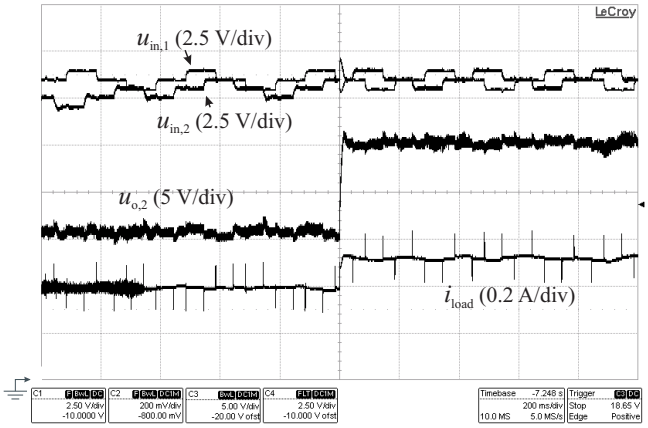

Fig. 4.20. Closed-loop MPP-tracking: Sudden increase in the output power of the other SAS module.

control is mandatory to obtain a high-performance system with series-connected DMPPT converters.

4.4 Conclusions

This chapter presented experimental validation of the analytical predictions discussed in Chapter 2. It was shown that the dynamic properties of the PV generator are of significant importance. Therefore, the properties of the solar array simulator, which is used to emulate an actual PV generator in laboratory environment, were studied. It was shown that the static operation of an emulating source is not sufficient for correctly reproducing the behavior of the PV generator. Instead, the dynamic behavior of the emulator should always be verified in order to obtain correct conclusions on the system performance.

Additionally, this chapter presented the measurement results for the patented converter structure both in frequency and time domain. The feasibility for PV interfacing, especially in parallel DMPPT system, was verified by examining the capability to provide power transfer from very low module voltages as well as by examining the conversion efficiency and dynamic characteristics. It was concluded that the proposed converter provides excellent performance in PV applications.

The third main aspect discussed in this chapter was the series and parallel configurations of interfacing converters. The predicted open-loop cross-coupling effects were verified to exist by frequency-domain analysis and shown to attenuate significantly, when the input-voltage control was applied. This phenomenon has been observed and presented by Ramos-Paja et al. (2010) and Petrone et al. (n.d.), but not explained earlier in the literature.

5 CONCLUSIONS

This chapter provides the final concluding discussion on the thesis and the scientific contribution. In addition, a brief discussion on future topics related to the subject of the thesis is given.

5.1 Final Conclusions

The field of power electronics, particularly the analysis and design of switched-mode converters and inverters, is dominated by the issues arising from practical applications. Most notably, the properties of electrical sources seem to persistently influence the way of thinking. Regarding practical applications, most often the input source for converters and inverters possesses voltage-type properties, and this has effectively narrowed the focus in the field to discuss almost solely voltage-sourced converters. Although the analysis and modeling of voltage-fed converters is well established and thoroughly verified, the dominance of voltage-fed thinking seems to be a burden, when analyzing systems with a current source as the input source for the converter. It has even been expressed that no native current sources exist (Sun, 2011).

It has been verified that the photovoltaic generator is a troublesome source of power, and its behavior differs significantly from a voltage-type source. The internal semiconductor structure yields a characteristic non-linear current-voltage relationship, and the generated power is maximized only under specific terminal voltage and current. Therefore, the non-linearity changes drastically the principles, according which the components in the power stage of the converter are selected and designed. Moreover, the existence of maximum power point introduces challenges for designing control circuitry, as the generated power should be maximized for power generation purposes. The tracking of the maximum power point is conveniently performed with switched-mode dc-dc converters.

Maximum power point tracking requires that the photovoltaic generator terminal current or terminal voltage is constantly adjusted, i.e., regulated, by a feedback loop to ensure operation at the maximum power point. A high-performance maximum power point tracking can be said to consist of three main parts: i) A high-efficiency switched-mode converter, capable of forcing the source to desired operating point, ii) a control circuitry that enables undistorted control of the source, and iii) an efficient algorithm that tracks the maximum power point and provides a corresponding reference to the

control circuitry. This thesis discussed the first two issues, as they have proven to be the most problematic, according to published research results.

The first switched-mode converters intended to interface a photovoltaic generator were conventional voltage-fed converters, having no feedback from the source terminal variables. These converters proved to yield operational anomalies and disturbances in the power generation. The reason for these findings can be explained to result from the power-limited nature of the photovoltaic generator, requiring a feedback loop from the source terminal to obtain stable operation. Thus, the choice between controlling source current or source voltage has to be made. For conventional voltage sources, only input current control is justified, as explained by control engineering principles. For current sources, the same rules justify only input voltage control. The photovoltaic generator, although widely treated as a non-linear current source, is persistently treated in a similar manner as a voltage source, leading to false interpretations, improper modeling and claims that do not hold. In this thesis, the current-source nature is emphasized in detail, with examples clearly pointing out the importance of correct modeling of the photovoltaic generator. A thorough discussion on the impedance properties of sources and their effect on the control of the converter is among the issues.

A well-designed control loop with stable operation is useless, if the power stage of the converter fails to complete its task, i.e., to force the source operating point to a desired value. Conventional voltage-sourced converters are designed to yield a desired *output terminal* voltage, whereas in photovoltaic converters the design requirement is defined according to the *input terminal* voltage. As the maximum power point may occur at very low voltages due to environmental conditions and shading issues, the converter must be able to provide a low enough voltage to the source terminal. Furthermore, in large systems it is beneficial to control discrete photovoltaic modules individually to maximize energy yield. For this reason, the concept of distributed photovoltaic system is presented with two main configurations, where the output terminals of interfacing converters are connected either in series or in parallel. A thorough discussion for both configurations is given, highlighting the operational benefits and disadvantages, with the conclusion that the parallel configuration is preferable. The series configuration is shown to contain inherent cross-coupling effects, impeding the maximum power extraction. A patented converter structure was presented for the parallel configuration, with notable performance.

The analysis procedure and practical verification presented in this thesis provides the reader a step-by-step method to correctly analyze and design an interfacing converter for a photovoltaic generator. It is shown that the non-ideal properties of the load and the source are essential and if neglected during the analysis, the performance of the system will be compromised. The concept of minor-loop gain is applied as means to verify the impedance-based stability of the interfacing converter. It is shown that an electronic

source emulating a photovoltaic generator must contain corresponding impedance behavior, to yield correct practical operation of the system. The foundations for the analysis and guidelines for implementation and verification of interfacing converters are summarized as the interfacing constraints, which form the basis for reliable operation of the interfacing converters in photovoltaic applications.

5.2 Future Topics

This thesis provided a comprehensive study on switched-mode dc-dc converters and their applications in interfacing a photovoltaic generator into a dc link. In light of the recent studies around the dynamic properties of dc-dc converters (Karppanen, 2008; Leppäaho, 2011) it can be said that a strong and well justified background for dynamic characterization of dc-dc converters in photovoltaic applications has now been presented. Thus, the foundations for designing and implementing high-performance photovoltaic electricity systems exist. However, this thesis and the preceding work have to be considered only as a summary of guidelines and not as the end of open questions.

In this thesis, the dynamic properties of balancing structures applied in a series connected configuration of distributed converters have not been studied. A complete understanding of the system requires understanding of the sub-systems as well, which is why the actual behavior of balancing structures should be examined.

In terms of increasing the energy yield of photovoltaic systems, novel converter topologies with high conversion efficiency are required. However, the dynamic characteristics of the power stage have to be analyzed as well, to verify the feasibility of the topology in photovoltaic interfacing.

Issues related to the maximum power point tracking algorithm may introduce additional phenomena in the control loop of the interfacing dc-dc converter. Thus, an additional control loop may actually emerge due to the tracking algorithm, but so far the analysis and interpretation related to this have not been presented.

An evident issue for future is the introduction of the concepts and methods presented in this thesis into practical use in the field. Recently, the photovoltaic power systems have experienced a strong market boom, which indicates that current-sourced converters are no longer an academic peculiarity. Instead, they have become a significant tool in the joint efforts to provide green energy sources and sustainable generation of electricity.

REFERENCES

Abbott, D. (2010). Keeping the energy debate clean: How do we supply the world's energy needs?, *Proc. IEEE* **98**(1): pp. 42–66.

Armstrong, S. and Hurley, W. G. (2005). Investigating the effectiveness of maximum power point tracking for a solar system, *IEEE 2005 Power Electronics Specialist Conf.*, pp. 204–209.

Averberg, A., Meyer, K. R. and Mertens, A. (2008). Current-fed full bridge converter for fuel cell systems, *IEEE 2008 Power Electronics Specialist Conf.*, pp. 866–872.

Balato, M., Vitelli, M., Femia, N., Petrone, G. and Spagnuolo, G. (2011). Factors limiting the efficiency of dmppt in pv applications, *2011 Int. Conf. on Clean Electrical Power*, pp. 604–608.

Bergveld, H. J., Büthker, D., Castello, C., Doorn, T. S., de Jong, A., van Otten, R. and de Waal, K. (2011). Module-level dc/dc conversion for photovoltaic systems, *IEEE 2011 Int. Telecommunications Energy Conf.*, pp. 1–9.

Bose, B. K. (2010). Global warming: Energy, environmental pollution, and the impact of power electronics, *IEEE Industrial Electronics Magazine* **4**(1): pp. 6–17.

Bratcu, A. I., Munteanu, I., Bacha, S., Picault, D. and Raison, B. (2011). Cascaded dc-dc converter photovoltaic systems: Power optimization issues, *IEEE Trans. Ind. Electron.* **58**(2): pp. 403–411.

Burger, B., Goeldi, B., Rogalla, S. and Schmidt, H. (2010). Module integrated electronics - an overview, *2010 European Photovoltaic Solar EnergyConf. and Exposition*, pp. 3700–3707.

Cabeza, L. F., Sole, C., Castell, A., Ono, E. and Gil, A. (2011). Review of solar thermal storage techniques and associated heat transfer technologies, *Proc. IEEE* **100**(2): pp. 525–538.

Capel, A., Marpinard, J. C., Jalade, J. and Valentin, M. (1983). Current fed and voltage fed switching dc/dc converters - steady state and dynamic models their applications in space technology, *Fifth Int. Telecommunications Energy Conf.*, pp. 421–430.

Chapin, D. M., Fuller, C. S. and Pearson, G. L. (1954). A new p-n junction photocell for converting solar radiation into electrical power, *J. Appl. Phys.* **25**(5): pp. 676–677.

Chenvidhya, D., Kirtikara, K. and Jivacate, C. (2006). Pv module dynamic impedance and its voltage and frequency dependencies, *Sol. Energy Mater. Sol. Cells* **86**(2): pp. 243–251.

Choi, W.-Y. and Lai, J. (2010). High-efficiency grid-connected photovoltaic module integrated converter system with high-speed communication interfaces for small-scale distributed power generation, *Solar Energy* **84**(4): pp. 636–649.

Deline, C., Marion, B., Granata, J. and Gonzalez, S. (2011). A performance and economic analysis of distributed power electronics in photovoltaic systems (accessed 14.5.2012). **URL:** *http://www.nrel.gov/docs/fy11osti/50003.pdf*

Dhople, S., Ehlmann, J., Davouli, A. and Chapman, P. (2010). Multiple-input boost converter to minimize power losses due to partial shading in photovoltaic modules, *IEEE 2010 Energy Conversion Congress and Exposition*, pp. 2633–2636.

Dorf, R. C. and Bishop, R. H. (2001). *Modern Control Systems*, 9th edn, Prentice-Hall Inc., USA. 831 pp.

Du, Y. and Lu, D. (2011). Battery-integrated boost converter utilizing distributed mppt configuration for photovoltaic systems, *Solar Energy* **85**(9): pp. 1992–2002.

Erickson, R. and Maksimović, D. (2001). *Fundamentals of Power Electronics*, 2nd edn, Kluwer Academic Publishers, USA. 883 pp.

Esram, T. and Chapman, P. L. (2007). Comparison of photovoltaic array maximum power point tracking techniques, *IEEE Trans. Energy Convers.* **22**(2): pp. 439–449.

Femia, N., Lisi, G., Petrone, G., Spagnuolo, G. and Vitelli, M. (2008). Distributed maximum power point tracking of photovoltaic arrays: Novel approach and system analysis, *IEEE Trans. Ind. Electron.* **55**(7): pp. 2610–2621.

Glaser, J. and Witulski, A. (1994). Output plane analysis of load-sharing in multiple-module converter systems, *IEEE Trans. Power Electron.* **9**(1): pp. 43–50.

Glass, M. (1977). Advancements in the design of solar array to battery charge current regulators, *IEEE 1977 Power Electronics Specialist Conf.*, pp. 346–350.

Hamza, D., Qiu, M. and Jain, P. (2011). Interface impedance consideration in the design of an input emi filter for grid-tied pv micro-inverter, *IEEE 2011 Industrial Electronics Conf.*, pp. 1390–1395.

Hsieh, Y.-P., Chen, J.-F., Liang, T.-J. and Yang, L.-S. (n.d.). Novel high step-up dc-dc converter for distributed generation system, *IEEE Trans. Ind. Electron.* . DOI: 10.1109/TIE.2011.2107721.

Huang, Y. and Tse, C. K. (2007). Circuit theoretic classification of parallel connected dc-dc converters, *IEEE Trans. Circuits Syst. I, Reg. Papers* **54**(5): pp. 1099–1108.

Huusari, J. and Suntio, T. (2011a). Current-fed quadratic full-bridge buck converter for pv systems interfacing: Dynamic characterization, *IEEE 2011 Energy Conversion Congress and Exposition*, pp. 487–494.

Huusari, J. and Suntio, T. (2011b). Current-fed quadratic full-bridge converter for pv systems interfacing: Static operation, *IEEE 2011 Power Electronics and Applications Conf.*, pp. 1–10.

Huusari, J. and Suntio, T. (2012a). Distributed mpp-tracking: Cross-coupling effects in series and parallel connected dc/dc converters, *2012 Photovoltaic Specialists Conf.* (in press).

Huusari, J. and Suntio, T. (2012b). Dynamic properties of current-fed quadratic full-bridge buck converter for distributed photovoltaic electricity systems, *IEEE Trans. Power Electron.* **27**(10). DOI: 10.1109/TPEL.2012.2186318.

Huusari, J. and Suntio, T. (2012c). Interfacing constraints of distributed maximum power point tracking converters in photovoltaic applications, *2012 Int. Power Electronics and Motion Control Conf.* (in press).

Huusari, J. and Suntio, T. (2012d). Transformer-isolated switching converter. Patent. US 7062320, EP 2421138, CN 102377346.

Imhoff, J., Pinheiro, J. R., Russi, J. L., Brum, D., Gules, R. and Hey, H. L. (2008). Dc-dc converters in a multi-string configuration for stand-alone photovoltaic systems, *IEEE 2008 Power Electronics Specialists Conf.*, pp. 2806–2812.

Jain, S. and Agarwal, V. (2007). Comparison of the performance of maximum power point tracking schemes applied to single-stage grid-connected photovoltaic systems, *IET Electr. Power Appl.* **1**(5): pp. 753–762.

James, P., Bahaj, A. and Braid, R. (2006). Pv array <5 kwp + single inverter = grid connected pv system: Are multiple inverter alternatives economic?, *Solar Energy* **80**(9): pp. 1179–1188.

Kadri, R., Gaubert, J.-P. and Champenois, G. (2012). Non-dissipative string current diverter for solving the cascaded dc-dc converter connection problem in photovoltaic power generation system, *IEEE Trans. Power Electron.* **27**(3): 1249–1258.

Karppanen, M. (2008). *Issues in Dynamic Analysis and Design of Interconnected DC-DC Power Supply Systems*, PhD thesis, Tampere University of Technology.

Kim, K. and Krein, P. (2010). Photovoltaic converter module configurations for maximum power point operation, *2010 Power and Energy Conf. at Illinois*, pp. 77–82.

Kim, S.-Y., Kim, N., Lee, H.-G., Hwang, C., Kim, G.-H., Seo, H.-R., Park, W. and Yu, I.-K. (2010). Analysis of differences between series and parallel connection of cascaded converters for pv generation system, *2010 Int. Electrical Machines and Systems Conf.*, pp. 628–632.

Kjaer, S., Pedersen, J. and Blaabjerg, F. (2005). A review of single-phase grid-connected inverters for photovoltaic modules, *IEEE Trans. Ind. Electron.* **41**(5): pp. 1292–1306.

Kopp, G. and Lean, J. L. (2011). A new, lower value of total solar irradiance: Evidence and climate significance, *Geophys. Res. Lett.* **38**(L01706): 7 pp.

Krein, P. T. (1998). *Elements of Power Electronics*, Oxford University Press, USA. 766 pp.

Kroposki, B., Margolis, R. and Ton, D. (2009). Harnessing the sun: An overview of solar technologies, *IEEE Power & Energy Magazine* **7**(3): pp. 22–33.

Kumar, R. A., Suresh, M. S. and Nagaraju, J. (2006). Effect of solar array capacitance on the performance of switching shunt regulator, *IEEE Trans. Power Electron.* **21**(2): pp. 543–548.

Leppäaho, J. (2011). *MPP-tracking DC-DC converters in photovoltaic applications*, PhD thesis, Tampere University of Technology.

Leppäaho, J., Huusari, J., Nousiainen, L., Puukko, J. and Suntio, T. (2011). Dynamic properties and stability assessment of current-fed converters in photovoltaic applications, *IEEJ Trans. Ind. Appl.* **131**(8): pp. 976–984.

Leppäaho, J., Karppanen, M. and Suntio, T. (2008). Current-sourced buck converter, *2008 Nordic Workshop on Power and Industrial Electronics*, p. 7.

Leppäaho, J., Nousiainen, L., Puukko, J., Huusari, J. and Suntio, T. (2010). Implementing current-fed converters by adding an input capacitor at the input of voltage-fed converter for interfacing solar generator, *2010 Int. Power Electronics and Motion Control Conf.*, pp. 81–88.

Leu, C.-S. and Huang, P.-Y. (2010). A novel voltage doubler rectifier for high output voltage applications, *2010 Power Electronics Conf.*, pp. 2082–2085.

Li, Q. and Wolfs, P. (2008). A review of the single phase photovoltaic module integrated converter topologies with three different dc link configurations, *IEEE Trans. Power Electron.* **23**(3): pp. 1320–1333.

Li, W. and He, X. (2011). Review of nonisolated high-step-up dc/dc converters in photovoltaic grid-connected applications, *IEEE Trans. Ind. Electron.* **58**(4): pp. 1239–1250.

Liang, Z., Guo, R., Li, J. and Huang, A. (2011). A high-efficiency pv module-integrated dc/dc converter for pv energy harvest in freedm systems, *IEEE Trans. Power Electron.* **26**(3): pp. 897–909.

Linares, L., Erickson, R. W., MacAlpine, S. and Brandemuehl, M. (2009). Improved energy capture in series string photovoltaics via smart distributed power electronics, *IEEE 2009 Applied Power Electronics Conf.*, pp. 904–910.

Liu, B., Duan, S. and Cai, T. (2011). Photovoltaic dc-building-module-based bipv system - concept and design considerations, *IEEE Trans. Power Electron.* **26**(5): pp. 1418–1429.

Liu, B., Liang, C. and Duan, S. (2008). Design considerations and topology selection for dc module-based building integrated photovoltaic system, *IEEE 2008 Industrial Electronics and Applications Conf.*, pp. 1066–1070.

Liu, K.-H. and Lee, F. C. (1988). Topological constraints on basic pwm converters, *IEEE 1988 Power Electronics Specialist Conf.*, pp. 164–172.

Lugue, A. and Hegedus, S. (2003). *Handbook of Photovoltaic Science and Engineeringn*, John Wiley & Sons, UK. 1164 pp.

Maksimovic, D. and Cuk, S. (1991). Switching converters with wide dc conversion range, *IEEE Trans. Power Electron.* **6**(1): pp. 151–157.

Maksimović, D., Stanković, A. M., Thottuvelli, V. J. and Verghese, G. C. (2001). Modeling and simulation of power electronic converters, *Proc. IEEE* **89**(6): pp. 898–912.

Mattick, C. S., Williams, E. and Allenby, B. R. (2010). Historical trends in global energy consumption, *IEEE Technol. Soc. Mag.* **29**(3): pp. 22–30.

Middlebrook, R. D. (1976). Input filter considerations in design and application of switching regulators, *1976 Industrial Applications Society Annual Meeting*, pp. 91–107.

Middlebrook, R. D. (1988). Small-signal modeling of pulse-width modulated switched-mode power converters, *Proc. IEEE* **76**(4): pp. 343–354.

Middlebrook, R. D. and Ćuk, S. (1976). A general unified approach to modelling switching-converter power stages, *IEEE 1976 Power Electronics Specialists Conf.*, pp. 18–34.

Mäki, A. and Valkealahti, S. (2012). Power losses in long string and parallel-connected short strings of series-connected silicon-based photovoltaic modules due to partial shading conditions, *IEEE Trans. on Energy Conversion* **27**(1): pp. 173–183.

Mäki, A., Valkealahti, S. and Suntio, T. (2010). Dynamic terminal characteristics of a photovoltaic generator, *2010 Int. Power Electronics and Motion Control Conf.*, pp. 76–80.

Mohan, N., Undeland, T. M. and Robbins, W. P. (2003). *Power Electronics: Converters, Applications and Design*, 3rd edn, John Wiley & Sons, Inc., USA. 802 pp.

Mohr, M. and Fuchs, F.-W. (2006). Voltage fed and current fed full bridge converter for the use in three phase grid connected fuel cell systems, *IEEE 2006 Int. Power Electronics and Motion Control Conf.*, pp. 1–7.

Myrzik, J. and Calais, M. (2003). String and module integrated inverters for single-phase grid connected phovoltaic systems - a review, *IEEE 2003 Power Tech Conf.*

Norton, B., Eames, P. C., Mallick, T. K., Huang, M. J., McCormack, S. J., Mondol, J. D. and Yohanis, Y. G. (2011). Enhancing the performance of building integrated photovoltaics, *Solar Energy* **85**(8): pp. 1629–1664.

Orduz, R., Solorzano, J., Edigo, M. A. and Roman, E. (n.d.). Analytical study and evaluation results of power optimizers for distributed power conditioning in photovoltaic arrays, *Progress in Photovoltaics* . DOI: 10.1002/pip.1188.

Patel, H. and Argawal, V. (2008). Maximum power point tracking scheme for pv systems operating under partially shaded conditions, *IEEE Trans. Ind. Electron.* **55**(4): pp. 1689–1698.

Petrone, G., Ramos-Paja, C. A., Spagnuolo, G. and Vitelli, M. (n.d.). Granular control of photovoltaic arrays by means of a multi-output maximum power point tracking algorithm, *Progress in Photovoltaics* . DOI: 10.1002/pip.2179.

Petrone, G., Spagnuolo, G., Teodorescu, R., Veerachary, M. and Vitelli, M. (2008). Reliability issues in photovoltaic power processing systems, *IEEE Trans. Ind. Electron.* **55**(7): pp. 2569–2580.

Poshtkouhi, S., Varley, J., Popuri, R. and Trescases, O. (2010). Analysis of distributed peak power tracking in photovoltaic systems, *IEEE 2010 Int. Power Electronics Conf.*, pp. 942–947.

Posthkouhi, S., Palaniappan, V., Fard, M. and Trescases, O. (2011). A general approach for quantifying the benefit of distributed power electronics for fine grained mppt in photovoltaic applications using 3d modeling, *IEEE Trans. Power Electron.* . DOI: 10.1109/TPEL.2011.2173353.

Puukko, J., Messo, T. and Suntio, T. (2011). Effect of photovoltaic generator on a typical vsi-based three-phase grid-connected photovoltaic inverter dynamics, *IEEE 2011 Conf. on Renewable Power Generation*, pp. 1–6.

Ramos-Paja, C., Spagnuolo, G., Petrone, G., Vitelli, M. and Bastidas, J. D. (2010). A multivariable mppt algorithm for granular control of photovoltaic systems, *IEEE 2010 Int. Symposium on Industrial Electronics*, pp. 3433–3437.

Razykov, T. M., Ferekides, C. S., Morel, D., Stefanekos, E., Ullal, H. S. and Upadhaya, H. M. (2011). Solar photovoltaic electricity: Current status and future prospects, *Solar Energy* **85**(8): pp. 1580–1608.

REN21 (2011). Renewables 2011: Global status report (accessed 14.5.2012).
URL: *http://bit.ly/REN21_GSR2011*

Renewable Energy Index (2011). Solar cell materials (accessed 14.5.2012).
URL: *http://renewableenergyindex.com/solar/solar-cell-materials*

Roman, E., Alonso, R., Ibanez, P., Elorduizapatarietxe, S. and Goitia, D. (2006). Intelligent pv module for grid-connected pv systems, *IEEE Trans. Ind. Electron.* **53**(4): pp. 1066–1073.

Roman, E., Martinez, V., Jimeno, J. C., Alonso, R., Ibanez, P. and Elorduizapatarietxe, S. (2008). Experimental results of controlled pv module for building integrated pv systems, *Solar Energy* **82**(5): pp. 471–480.

Sahan, B., Vergara, A., Henze, N., Engler, A. and Zacharias, P. (2008). A single-stage pv module integrated converter based on a low-power current-source inverter, *IEEE Trans. Ind. Electron.* **55**(7): pp. 2602–2609.

Shimizu, T., Hirakata, M., Kamezawa, T. and Watanabe, H. (2001). Generation control circuit for photovoltaic modules, *IEEE Trans. Power Electron.* **16**(3): pp. 293–300.

Shmilovitz, D. (2005). On the control of photovoltaic maximum power poin tracker via output parameters, *IEE Proc.-Electr. Power Appl.* **152**(2): pp. 239–248.

Shmilovitz, D. and Singer, S. (2002). Interfacing photovoltaic panels via a capacitive converter, *2002 Electrical and Electronics Engineers in Israel Conv.*, pp. 160–162.

Siri, K. and Willhoff, M. (2011). Optimum power tracking among series-connected power sources with uniform voltage distribution, *IEEE 2011 Aerospace Conf.*, pp. 1–11.

Solaredge (2012). Solaredge power optimizer - module embedded solution (accessed 14.5.2012).

URL: *http://www.solaredge.com/files/pdfs/products/powerboxes/se-pb-csi-datasheet.pdf*

Song, W. and Lehman, B. (2007). Current-fed dual-bridge dc-dc converter, *IEEE Trans. Power Electron.* **22**(2): pp. 461–469.

Spagnuolo, G., Petrone, G., Araújo, S. V., Cecati, C., Friis-Madsen, E., Gubía, E., Hissel, D., Jasinski, M., Knapp, W., Liserre, M., Rodriguez, P., Teodorescu, R. and Zacharias, P. (2010). Renewable energy operation and conversion schemes: A summary of discussions during the seminar on renewable energy systems, *IEEE Industrial Electronics Magazine* **4**(1): pp. 38–51.

Streetman, B. G. and Banerjee, S. K. (2005). *Solid state electronic devices*, 6th edn, Prentice-Hall Inc., USA. 581 pp.

Sun, J. (2011). Impedance-based stability criterion for grid-connected inverters, *IEEE Power Electron Lett.* **26**(11): pp. 3075–3078.

Suntio, T. (2009). *Dynamic Profile of Switched-Mode Converter: Modeling, Analysis and Control*, Wiley-VCH, Germany. 357 pp.

Suntio, T., Huusari, J. and Leppäaho, J. (2010). Issues on solar-generator interfacing with voltage-fed mpp-tracking converters, *EPE Journal* **20**(3): pp. 40–47.

Suntio, T., Leppäaho, J., Huusari, J. and Nousiainen, L. (2010). Issues on solar-generator interfacing with current-fed mpp-tracking converters, *IEEE Trans. Power Electron.* **25**(9): pp. 2409–2419.

The Federal Government of Germany (2011). Switching to the electricity of the future (accessed 14.5.2012).
URL: *http://www.bundesregierung.de/Content/EN/Artikel/_2011/06/2011-06-09-regierungserklaerung_en.html?nn=454766*

Tsao, P., Sarhan, S. and Jorio, I. (2009). Distributed max power point tracking for photovoltaic arrays, *IEEE 2009 Photovoltaic Specialists Conf.*, pp. 2293–2298.

Vighetti, S., Ferrieux, J.-P. and Lembeye, Y. (2012). Optimization and design of a cascaded dc/dc converter devoted to grid connected photovoltaic systems, *IEEE Trans. Power Electron.* **27**(4): pp. 2018–2027.

Walker, G. and Pierce, J. (2006). Photovoltaic dc-dc module integrated converter for novel cascaded and bypass grid connection topologies - design and optimization, *IEEE 2006 Power Electronics Specialist Conf.*, pp. 1–7.

Walker, G. and Sernia, P. (2004). Cascaded dc-dc converter connection of photovoltaic modules, *IEEE Trans. Power Electron.* **19**(4): pp. 1130–1139.

Weaver, W. and Krein, P. T. (2007). Analysis and applications of a current-sourced buck converter, *IEEE 2007 Applied Power Electronics Conf.*, pp. 1664–1670.

Wenham, S. R. and Green, M. A. (1996). Silicon solar cells, *Progress in Photovoltaics* **4**(1): pp. 3–33.

Wills, R., Halla, F., Strong, S. and Wohlgemuth, J. (1996). The ac photovoltaic module, *IEEE 1996 Photovoltaic Specialists Conf.*, pp. 1231–1234.

Xiao, W., Dunford, W. G., Palmer, P. R. and Capel, A. (2007). Regulation of photovoltaic voltage, *IEEE Trans. Ind. Electron.* **54**(3): pp. 1365–1374.

Xiao, W., Ozog, N. and Dunford, W. (2007). Topology study of photovoltaic interface for maximum power point tracking, *IEEE Trans. Ind. Electron.* **54**(3): pp. 1696–1704.

APPENDICES

Appendix A: Impedance Measurement Setups

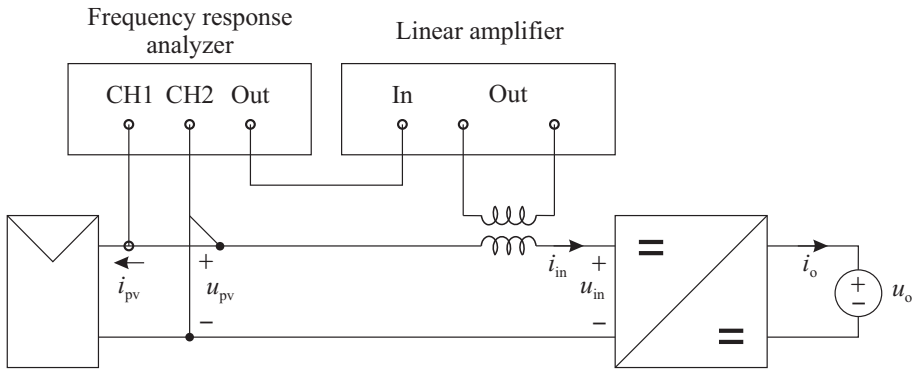

Fig. A-1. Setup for measuring the output impedance of the PV generator.

Output impedance of the PV generator:

$$Z_{\mathrm{o,pv}} = \frac{u_{\mathrm{pv}}}{i_{\mathrm{pv}}}. \tag{A-1}$$

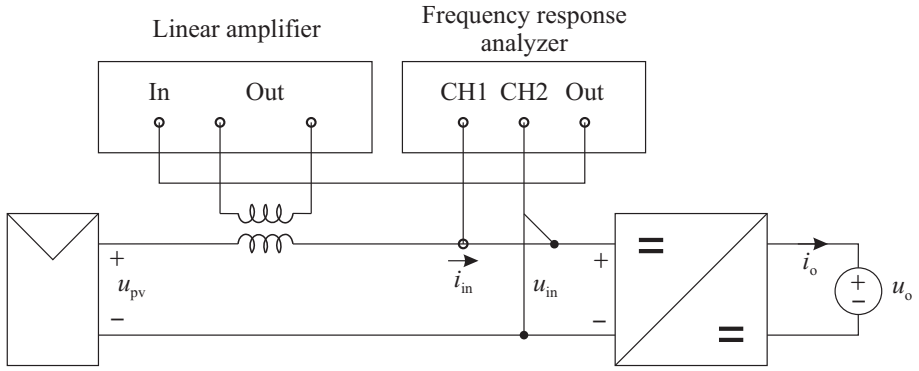

Fig. A-2. Setup for measuring the input impedance of an interfacing converter.

Input impedance of the converter:

$$Z_{\mathrm{in,conv}} = \frac{u_{\mathrm{in}}}{i_{\mathrm{in}}}. \tag{A-2}$$

Appendix B: Cross-Coupling Measurement Setup

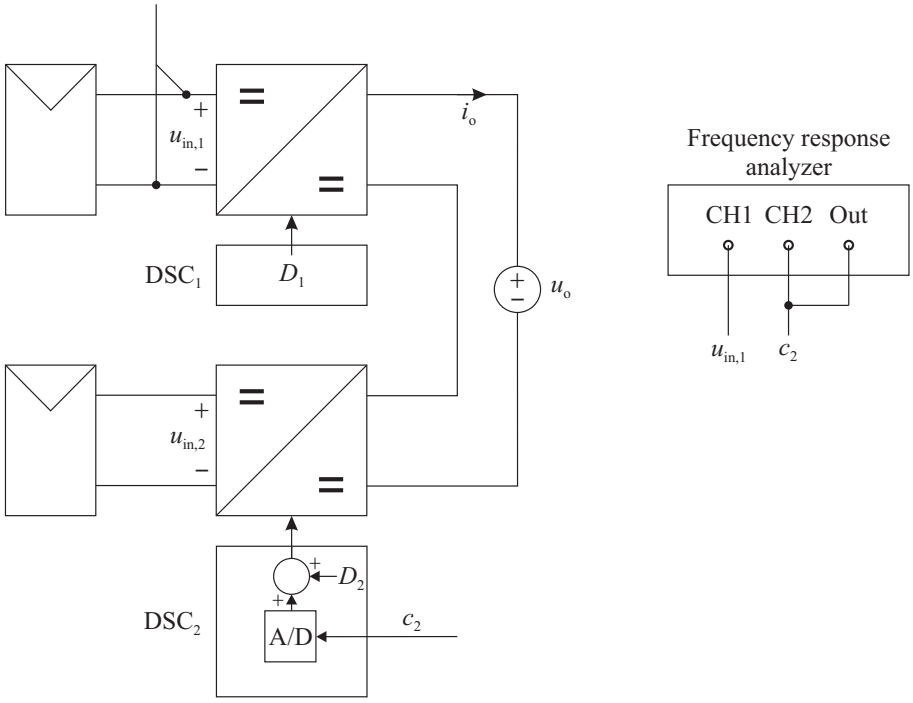

Fig. B-3. Scheme for measuring the open-loop control cross-coupling.

Control cross-coupling:

$$G_{\mathrm{cr1}} = \frac{u_{\mathrm{in},1}}{c_2}. \tag{B-3}$$

- At open loop: Both converters receive constant duty cycle from corresponding DSC. External perturbation is injected into DSC$_2$, digitalized and added into duty cycle. The transfer function is measured directly as the ratio between the perturbation c_2 and the input voltage $u_{\mathrm{in},1}$.
- At closed loop: Both converters operate under input-voltage control. External perturbation is injected into DSC$_2$, digitalized and added into input voltage reference. The transfer function is measured directly as the ratio between the perturbation $u_{\mathrm{ref},2}$ and the input voltage $u_{\mathrm{in},1}$.

Appendix C: Matlab Code for Analyzing the CFQFB Converter

```
%%%%%%%%%%%%%%%%%%%%%%%%%%%%%%%%%%%%%%%%%%%%%%%%%%%%%%%%%%%%%%%%%%%%%%%%%%%%%%%
% Current-Fed Quadratic Full-Bridge Buck Converter                             %
% Analytical transfer functions                                               %
% ------------------------------------------------------------------------- %
% (c) Juha Huusari                                                            %
% Tampere University of Technology 2012                                       %
%%%%%%%%%%%%%%%%%%%%%%%%%%%%%%%%%%%%%%%%%%%%%%%%%%%%%%%%%%%%%%%%%%%%%%%%%%%%%%%

% Input parameters
Uo = 350; Uin = 25.9; Iin = 7.33; fs = 200e3; Ts = 1/fs; n = 0.225

% Parasitic elements
rc1 = 5e-3; rc2 = 5e-3; rc3 = 120e-3; rc4 = 130e-3; rl1 = 10e-3; rl2 = 10e-3;
rl3 = 30e-3; rd1 = 30e-3; rd2 = 40e-3; rd3 = 40e-3; rd4 = 10e-3; rds = 55e-3;
rpri = 20e-3; rsec = 70e-3; Ud1 = 1.2; Ud2 = 1.1; Ud3 = 1.2; Ud4 = 1.0;

% The duty cycle D with its complement (D1 = 1 - D) at operating point
D  = sqrt((2*Uin)/(ns*Uo)); D1 = 1 - D;

% Component values
L1 = 20e-6; L2 = 24e-6; L3 = 25e-6; Lm = 1e-3;
C1 = 2300e-6; C2 = 2200e-6; C3 = 35e-6; C4 = 35e-6;

% The steady-state parameters
Uc1 = Uin; Uc2 = n*Uo/2; Uc3 = Uo/2 + n*D^2*rl3*Iin/4;
Uc4 = Uc3; Il1 = Iin; Il2 = D*Il1; Il3 = 0.5*n*D*Il2;

% The state-space coefficients R1-R3, U1, U2
R1 = rc1 + rl1 + D*(rd2+rc2) + D1*(rd1+rds);
R2 = D1*rds - D*rc2;
R3 = rc2 + rl2 + D1*rds + D*(2*rds + rpri + 0.5*n*n*(2*rsec + ...
    rd3 + rc3 + rd4 + rc4));
R4 = 0.5*n*(rc3 + rc4);
R5 = rc3 + rc4 + rlo;
R6 = 2*rsec + rd3 + rd4 + rc3 + rc4;
R7 = rd4 + rc4 - rd3 - rc3;
U1 = (rd2 + rc2 - rd1 - rds)*Il1 - (rds + rc2)*Il2 + Uc2 - Ud1 + Ud2;
U2 = -(rds+rc2)*Il1 + (2*rds + rpri - rds + 0.5*n*n*(2*rsec + ...
    rd3 + rc3 + rd4 + rc4))*Il2 + 0.5*n*(rc3 + rc4)*Il3 + ...
    0.5*n*(Uc3 + Uc4 + Ud3 + Ud4);
```

```
U3 = n*Il2*R7 + 0.5*Il3*(rc4 - rc3) - 0.5*Uc3 + 0.5*Uc4;
k1 = 0.5*D; k2 = 0.5*D*n; k3 = 0.5*D*(rc3-rc4);

% The state matrices
Am = [...
-R1/L1    -R2/L1       0        0 1/L1 -D/L1      0      0;
-R2/L2    -R3/L2 D*R4/L2 k2*R7/L2    0  1/L2 -k2/L2 -k2/L2;
     0   D*R4/L3  -R5/L3    k3/L3    0     0   1/L3   1/L3;
     0 n*D*R7/Lm   k3/Lm -D*R6/Lm    0     0 -k1/Lm  k1/Lm;
 -1/C1         0       0        0    0     0      0      0;
  D/C2     -1/C2       0        0    0     0      0      0;
     0     k2/C3   -1/C3   -k1/C3    0     0      0      0;
     0     k2/C4   -1/C4    k1/C4    0     0      0      0];

Bm = [rc1/L1     0       -U1/L1;
           0     0       -U2/L2;
           0 -1/L3    R4*Il2/L3;
           0     0        U3/Lm;
        1/C1     0            0;
           0     0       Il1/C2;
           0     0 0.5*n*Il2/C3;
           0     0 0.5*n*Il2/C4];

Cm = [-rc1   0   0   0   1   0   0   0;
         0   0   1   0   0   0   0   0];

Dm = [rc1  0 0;
        0  0 0];

% ------------------------------------------------------------------------ %
% The H-parameters                                                         %
% ------------------------------------------------------------------------ %
H = ss(Am,Bm,Cm,Dm);

Zin_o =  H(1,1);  % Open-loop input impedance
Toi_o =  H(1,2);  % Open-loop reverse transfer function
Gci_o =  H(1,3);  % Open-loop control-to-input transfer function
Gio_o =  H(2,1);  % Open-loop forward transfer function
Yo_o  = -H(2,2);  % Open-loop output admittance
Gco_o =  H(2,3);  % Open-loop control-to-output transfer function

% End
```

Appendix D: Matlab Code for Symbolic Transfer Functions (CFQFB)

```
%%%%%%%%%%%%%%%%%%%%%%%%%%%%%%%%%%%%%%%%%%%%%%%%%%%%%%%%%%%%%%%%%%%%%%%%%%%%%%%
% Current-Fed Quadratic Full-Bridge Converter                                  %
% Symbolic transfer functions                                                  %
% ---------------------------------------------------------------------------- %
% (c) Juha Huusari                                                             %
% Tampere University of Technology 2012                                        %
%%%%%%%%%%%%%%%%%%%%%%%%%%%%%%%%%%%%%%%%%%%%%%%%%%%%%%%%%%%%%%%%%%%%%%%%%%%%%%%

% Define symbolic variables
syms D rc1 R1 R2 R3 R4 R5 R6 R6 R7 U1 U2 U3 L1 L2 L3 Lm C1 C2 C3 C4
syms rc1 k1 k2 k3 n Il1 Il2 s

% The state matrices
Am = [...
-R1/L1    -R2/L1       0        0 1/L1 -D/L1      0      0;
-R2/L2    -R3/L2 D*R4/L2 k2*R7/L2    0  1/L2 -k2/L2 -k2/L2;
     0   D*R4/L3  -R5/L3    k3/L3    0     0   1/L3   1/L3;
     0 n*D*R7/Lm   k3/Lm -D*R6/Lm    0     0 -k1/Lm  k1/Lm;
 -1/C1         0       0        0    0     0      0      0;
  D/C2     -1/C2       0        0    0     0      0      0;
     0     k2/C3   -1/C3   -k1/C3    0     0      0      0;
     0     k2/C4   -1/C4    k1/C4    0     0      0      0];

Bm = [rc1/L1     0       -U1/L1;
           0     0       -U2/L2;
           0 -1/L3    R4*Il2/L3;
           0     0        U3/Lm;
        1/C1     0            0;
           0     0       Il1/C2;
           0     0 0.5*n*Il2/C3;
           0     0 0.5*n*Il2/C4];

Cm = [-rc1   0   0   0   1   0   0   0;
         0   0   1   0   0   0   0   0];

Dm = [rc1  0 0;
        0  0 0];

% Unity matrix corresponding to the size of Am
sI = s*eye(8);
```

```
% ------------------------------------------------------------------------ %
% The H-parameters                                                         %
% ------------------------------------------------------------------------ %
H = Cm*inv(sI-Am)*Bm+Dm;

Zin_o =  H(1,1);  % Open-loop input impedance
Toi_o =  H(1,2);  % Open-loop reverse transfer function
Gci_o =  H(1,3);  % Open-loop control-to-input transfer function
Gio_o =  H(2,1);  % Open-loop forward transfer function
Yo_o  = -H(2,2);  % Open-loop output admittance
Gco_o =  H(2,3);  % Open-loop control-to-output transfer function

% End
```

Appendix E: Matlab Code for Analyzing the Buck-Boost Converter

```
%%%%%%%%%%%%%%%%%%%%%%%%%%%%%%%%%%%%%%%%%%%%%%%%%%%%%%%%%%%%%%%%%%%%%%%%%%%%%%%
% Current-Fed Buck-Boost Converter                                             %
% Analytical transfer functions                                                %
% ---------------------------------------------------------------------------- %
% (c) Juha Huusari                                                             %
% Tampere University of Technology 2012                                        %
%%%%%%%%%%%%%%%%%%%%%%%%%%%%%%%%%%%%%%%%%%%%%%%%%%%%%%%%%%%%%%%%%%%%%%%%%%%%%%%

% Input parameters
Upv = 16; Uo  = 50; Ipv = 1.0; fs = 100e3; Ts = 1/fs;

% Component values
L1 = 120e-6; L2 = 1e-9; C1 = 200e-6; C2 = 100e-6;

% Parasitic elements
rL1 = 40e-3; rL2 = 1e-3; rC1 = 40e-3; rC2 = 30e-3; rD1 = 40e-3;
rD2 = 35e-3; rDS1 = 50e-3; rDS2 = 45e-3; Ud1 = 0.5; Ud2 = 0.4;

% The duty cycle D with its complement D'
D  = Upv/(Uo + Upv);
D1 = 1 - D;

% The steady-state values
IL1 = Ipv/D1; IL2 = D*IL1; Uc1 = Upv; Uc2 = Uo;

% The state-space coefficients R1 and U1
R1 = rL1 + D*(rD1 + rD2 + rC2) + D1*(rC1 + rDS1 + rDS2);
U1 = (rD1+rD2+rC2-rDS1-rDS2-rC1)*IL1 - rC2*IL2 + Uc1 ...
    + Uc2 + Ud1 + Ud2 - rC1*Ipv;

% The state matrices
Am = [  -R1/L1      D*rC2/L1 D1/L1 -D/L1;
      D*rC2/L2 -(rC2+rL2)/L2     0  1/L2;
        -D1/C1              0     0     0;
          D/C2         -1/C2     0     0];

Bm = [D1*rC1/L1     0       -U1/L1;
              0 -1/L2 (rC2*IL1)/L2;
           1/C1     0       IL1/C1;
              0     0       IL1/C2];
```

```
Cm = [-D1*rC1   0   1   0;
            0   1   0   0];

Dm = [rC1   0   0;
        0   0   0];

s = tf('s');

% Unity matrix corresponding to the size of Am
sI = s*eye(4);

Hm = Cm*inv(sI-Am)*Bm+Dm;

% ------------------------------------------------------------------------ %
% The H-parameters                                                         %
% ------------------------------------------------------------------------ %
H = ss(Am,Bm,Cm,Dm);

Zin_o =  H(1,1);  % Open-loop input impedance
Toi_o =  H(1,2);  % Open-loop reverse transfer function
Gci_o =  H(1,3);  % Open-loop control-to-input transfer function
Gio_o =  H(2,1);  % Open-loop forward transfer function
Yo_o  = -H(2,2);  % Open-loop output admittance
Gco_o =  H(2,3);  % Open-loop control-to-output transfer function

% End
```

Appendix F: Matlab Code for Symbolic Transfer Functions (Buck-Boost)

```
%%%%%%%%%%%%%%%%%%%%%%%%%%%%%%%%%%%%%%%%%%%%%%%%%%%%%%%%%%%%%%%%%%%%%%%%%%%%%%%
% Current-Fed Buck-Boost Converter                                              %
% Symbolic transfer functions                                                   %
% ----------------------------------------------------------------------------- %
% (c) Juha Huusari                                                              %
% Tampere University of Technology 2012                                         %
%%%%%%%%%%%%%%%%%%%%%%%%%%%%%%%%%%%%%%%%%%%%%%%%%%%%%%%%%%%%%%%%%%%%%%%%%%%%%%%

% Symbolic variables
syms Upv Uo Ipv L1 L2 C1 C2 rC1 rC2 rL2 D D1 IL1 R1 U1 s

% The state matrices
Am = [  -R1/L1      D*rC2/L1 D1/L1 -D/L1;
      D*rC2/L2 -(rC2+rL2)/L2     0  1/L2;
        -D1/C1              0     0     0;
          D/C2         -1/C2     0     0];

Bm = [D1*rC1/L1     0       -U1/L1;
              0 -1/L2 (rC2*IL1)/L2;
           1/C1     0       IL1/C1;
              0     0       IL1/C2];

Cm = [-D1*rC1   0   1   0;
            0   1   0   0];

Dm = [rC1   0   0;
        0   0   0];

% Unity matrix corresponding to the size of Am
sI = s*eye(4);

% ----------------------------------------------------------------------------- %
% The H-parameters                                                              %
% ----------------------------------------------------------------------------- %
Hm = Cm*inv(sI-Am)*Bm+Dm;

Zin_o =  Hm(1,1);  % Open-loop input impedance
Toi_o =  Hm(1,2);  % Open-loop reverse transfer function
Gci_o =  Hm(1,3);  % Open-loop control-to-input transfer function
```

```
Gio_o =  Hm(2,1);  % Open-loop forward transfer function
Yo_o  = -Hm(2,2);  % Open-loop output admittance
Gco_o =  Hm(2,3);  % Open-loop control-to-output transfer function

% An example: Separate numerator and denominator for Zin-o
[Zin_num, Zin_den] = numden(Zin_o);

% Simplify the expressions
Zin_num_simplified = simplify(Zin_num);
Zin_den_simplified = simplify(Zin_den);

% Display the results
pretty(Zin_num_simplified)
pretty(Zin_den_simplified)

% End
```

Appendix G: Matlab Code for Inclusion of Source and Load Non-Idealities

```
%%%%%%%%%%%%%%%%%%%%%%%%%%%%%%%%%%%%%%%%%%%%%%%%%%%%%%%%%%%%%%%%%%%%%%%%%%%%%%%%
% Current-Fed Converters:                                                       %
% Inclusion of source and load non-idealities to ideal open-loop                %
% transfer functions                                                            %
% ----------------------------------------------------------------------------- %
% (c) Juha Huusari                                                              %
% Tampere University of Technology 2012                                         %
%%%%%%%%%%%%%%%%%%%%%%%%%%%%%%%%%%%%%%%%%%%%%%%%%%%%%%%%%%%%%%%%%%%%%%%%%%%%%%%%

% ----------------------------------------------------------------------------- %
% The H-parameters (open-loop, ideal)                                           %
% ----------------------------------------------------------------------------- %
H = ss(Am,Bm,Cm,Dm);

Zin_o =  H(1,1);
Toi_o =  H(1,2);
Gci_o =  H(1,3);
Gio_o =  H(2,1);
Yo_o  = -H(2,2);
Gco_o =  H(2,3);

% ----------------------------------------------------------------------------- %
% Load and source effects added to the analytical transfer functions            %
% ----------------------------------------------------------------------------- %

% Measured load impedance ZL and source admittance YS:
% Can be replaced with analytical predictions
ZL = ZL_meas; YS = YS_meas;

% The special parameters
Zin_oc  = Zin_o + (Gio_o*Toi_o)/Yo_o;
Zin_inf = Zin_o - (Gio_o*Gci_o)/Gco_o;
Yo_inf  = Yo_o  + (Toi_o*Gco_o)/Gci_o;
Yo_sci  = Yo_o  + (Gio_o*Toi_o)/Zin_o;
Gio_inf = Gio_o - (Zin_o*Gco_o)/Gci_o;

% Predicted transfer functions
Zin_oL = Zin_o*(1 + ZL*Yo_sci)/(1 + ZL*Yo_o) + Zadd;
Toi_oS = Toi_o/(1 + YS*Zin_o);
```

```
Gio_oL = Gio_o/(1 + ZL*Yo_o);
Yo_oS  = (1 + YS*Zin_oc)/(1 + YS*Zin_o)*Yo_o;
Gci_LS = (Gci_o + (ZL*Gco_o*Toi_o)/(1+ZL*Yo_o))*(1/(1+Zin_o*YS));
Gco_LS = Gco_o*(1 + YS*Zin_inf)/((1 + YS*Zin_o)*(1 + ZL*Yo_o));

% Note:
% - Load effect visible in input impedance and in forward transfer
%   function
% - Source effect visible in output admittance and in reverse
%   transfer function
% - Control transfer functions contain both effects

% End
```

Appendix H: Derivation of Closed-Loop Control Cross-Coupling

Referring to Fig. 2.23, by neglecting all other input variables except $\hat{u}_{\mathrm{ref2}}$, the input voltages can be expressed as

$$\begin{aligned}\hat{u}_{\mathrm{in1}} &= G_{\mathrm{ci1}}\hat{c}_1 + G_{\mathrm{cr1}}\hat{c}_2 \\ \hat{u}_{\mathrm{in2}} &= G_{\mathrm{cr2}}\hat{c}_1 + G_{\mathrm{ci2}}\hat{c}_2.\end{aligned} \tag{H-1}$$

By denoting loop gains as $L_1 = G_{\mathrm{se1}}G_{\mathrm{c1}}G_{\mathrm{ci1}}$ and $L_2 = G_{\mathrm{se2}}G_{\mathrm{c2}}G_{\mathrm{ci2}}$, the control variables can be presented as

$$\begin{aligned}\hat{c}_1 &= -G_{\mathrm{se1}}G_{\mathrm{c1}}\hat{u}_{\mathrm{in1}} = -\frac{L_1}{G_{\mathrm{ci1}}}\hat{u}_{\mathrm{in1}} \\ \hat{c}_2 &= G_{\mathrm{c2}}(\hat{u}_{\mathrm{ref2}} - G_{\mathrm{se2}}\hat{u}_{\mathrm{in2}}) = G_{\mathrm{c2}}\hat{u}_{\mathrm{ref2}} - \frac{L_2}{G_{\mathrm{ci2}}}\hat{u}_{\mathrm{in2}}.\end{aligned} \tag{H-2}$$

Substituting $\hat{c}_1$ and $\hat{c}_1$ in (H-1) with the expressions shown in (H-2) yields

$$\begin{aligned}\hat{u}_{\mathrm{in1}} &= -L_1\hat{u}_{\mathrm{in1}} + G_{\mathrm{cr1}}G_{\mathrm{c2}}\hat{u}_{\mathrm{ref2}} - L_2\frac{G_{\mathrm{cr1}}}{G_{\mathrm{ci2}}}\hat{u}_{\mathrm{in2}} \\ \hat{u}_{\mathrm{in2}} &= -L_1\frac{G_{\mathrm{cr2}}}{G_{\mathrm{ci1}}}\hat{u}_{\mathrm{in1}} + G_{\mathrm{ci2}}G_{\mathrm{c2}}\hat{u}_{\mathrm{ref2}} - L_2\hat{u}_{\mathrm{in2}},\end{aligned} \tag{H-3}$$

which can be simplified to yield

$$\hat{u}_{\mathrm{in1}} = \frac{G_{\mathrm{cr1}}G_{\mathrm{c2}}}{1+L_1}\hat{u}_{\mathrm{ref2}} - L_2\frac{G_{\mathrm{cr1}}}{G_{\mathrm{ci2}}}\frac{1}{1+L_1}\hat{u}_{\mathrm{in2}} \tag{H-4}$$

$$\hat{u}_{\mathrm{in2}} = -L_1\frac{G_{\mathrm{cr2}}}{G_{\mathrm{ci1}}}\frac{1}{1+L_2}\hat{u}_{\mathrm{in1}} + \frac{G_{\mathrm{ci2}}G_{\mathrm{c2}}}{1+L_2}\hat{u}_{\mathrm{ref2}}. \tag{H-5}$$

Finally, by substituting $\hat{u}_{\mathrm{in2}}$ in (H-4) with (H-5), the following expression for $\hat{u}_{\mathrm{in1}}$ is obtained

$$\hat{u}_{\mathrm{in1}} = \frac{G_{\mathrm{cr1}}G_{\mathrm{c2}}}{1+L_1}\hat{u}_{\mathrm{ref2}} + \frac{G_{\mathrm{cr1}}}{G_{\mathrm{ci2}}}\frac{G_{\mathrm{cr2}}}{G_{\mathrm{ci1}}}\frac{L_1}{1+L_1}\frac{L_2}{1+L_2}\hat{u}_{\mathrm{in1}} - G_{\mathrm{cr1}}G_{\mathrm{c2}}\frac{1}{1+L_1}\frac{L_2}{1+L_2}\hat{u}_{\mathrm{ref2}}. \tag{H-6}$$

The control cross-coupling transfer function is, therefore

$$\frac{\hat{u}_{\mathrm{in1}}}{\hat{u}_{\mathrm{ref2}}} = \frac{1}{1+L_1}\frac{G_{\mathrm{cr1}}G_{\mathrm{c2}}\left(1-\dfrac{L_2}{1+L_2}\right)}{1-\dfrac{G_{\mathrm{cr1}}}{G_{\mathrm{ci2}}}\dfrac{G_{\mathrm{cr2}}}{G_{\mathrm{ci1}}}\dfrac{L_1}{1+L_1}\dfrac{L_2}{1+L_2}}. \tag{H-7}$$

Appendix I: Derivation of Closed-Loop Input Cross-Coupling

Referring to Fig. 2.23, by neglecting all other input variables except $\hat{i}_{\mathrm{in2}}$, the input voltages can be expressed as

$$\begin{aligned}\hat{u}_{\mathrm{in1}} &= G_{\mathrm{ci1}}\hat{c}_1 + T_{\mathrm{cr1}}\hat{i}_{\mathrm{in2}} + G_{\mathrm{cr1}}\hat{c}_2\\ \hat{u}_{\mathrm{in2}} &= G_{\mathrm{cr2}}\hat{c}_1 + Z_{\mathrm{in2}}\hat{i}_{\mathrm{in2}} + G_{\mathrm{ci2}}\hat{c}_2.\end{aligned} \tag{I-1}$$

By denoting loop gains as $L_1 = G_{\mathrm{se1}}G_{\mathrm{c1}}G_{\mathrm{ci1}}$ and $L_2 = G_{\mathrm{se2}}G_{\mathrm{c2}}G_{\mathrm{ci2}}$, the control variables can be presented as

$$\begin{aligned}\hat{c}_1 &= -G_{\mathrm{se1}}G_{\mathrm{c1}}\hat{u}_{\mathrm{in1}} = -\frac{L_1}{G_{\mathrm{ci1}}}\hat{u}_{\mathrm{in1}}\\ \hat{c}_2 &= -G_{\mathrm{se2}}G_{\mathrm{c2}}\hat{u}_{\mathrm{in2}} = -\frac{L_2}{G_{\mathrm{ci2}}}\hat{u}_{\mathrm{in2}}.\end{aligned} \tag{I-2}$$

Substituting $\hat{c}_1$ and $\hat{c}_2$ in (I-1) with the expressions shown in (I-2) yields

$$\begin{aligned}\hat{u}_{\mathrm{in1}} &= -L_1\hat{u}_{\mathrm{in1}} + T_{\mathrm{cr1}}\hat{i}_{\mathrm{in2}} - L_2\frac{G_{\mathrm{cr1}}}{G_{\mathrm{ci2}}}\hat{u}_{\mathrm{in2}}\\ \hat{u}_{\mathrm{in2}} &= -L_1\frac{G_{\mathrm{cr2}}}{G_{\mathrm{ci1}}}\hat{u}_{\mathrm{in1}} + Z_{\mathrm{in2}}\hat{i}_{\mathrm{in2}} - L_2\hat{u}_{\mathrm{in2}},\end{aligned} \tag{I-3}$$

which can be simplified to yield

$$\hat{u}_{\mathrm{in1}} = \frac{T_{\mathrm{cr1}}}{1+L_1}\hat{i}_{\mathrm{in2}} - \frac{G_{\mathrm{cr1}}}{G_{\mathrm{ci2}}}\frac{L_2}{1+L_1}\hat{u}_{\mathrm{in2}} \tag{I-4}$$

$$\hat{u}_{\mathrm{in2}} = -\frac{G_{\mathrm{cr2}}}{G_{\mathrm{ci1}}}\frac{L_1}{1+L_2}\hat{u}_{\mathrm{in1}} + \frac{Z_{\mathrm{in2}}}{1+L_2}\hat{i}_{\mathrm{in2}}. \tag{I-5}$$

Finally, by substituting $\hat{u}_{\mathrm{in2}}$ in (I-4) with (I-5), the following expression for $\hat{u}_{\mathrm{in1}}$ is obtained

$$\hat{u}_{\mathrm{in1}} = \frac{T_{\mathrm{cr1}}}{1+L_1}\hat{i}_{\mathrm{in2}} + \frac{G_{\mathrm{cr1}}}{G_{\mathrm{ci2}}}\frac{G_{\mathrm{cr2}}}{G_{\mathrm{ci1}}}\frac{L_1}{1+L_1}\frac{L_2}{1+L_2}\hat{u}_{\mathrm{in1}} - Z_{\mathrm{in2}}\frac{G_{\mathrm{cr1}}}{G_{\mathrm{c2}}}\frac{1}{1+L_1}\frac{L_2}{1+L_2}\hat{i}_{\mathrm{in2}}. \tag{I-6}$$

The input cross-coupling transfer function is, therefore

$$\frac{\hat{u}_{\mathrm{in1}}}{\hat{i}_{\mathrm{in2}}} = \frac{1}{1+L_1}\frac{T_{\mathrm{cr1}} - Z_{\mathrm{in2}}\dfrac{G_{\mathrm{cr1}}}{G_{\mathrm{c2}}}\dfrac{L_2}{1+L_2}}{1 - \dfrac{G_{\mathrm{cr1}}}{G_{\mathrm{ci2}}}\dfrac{G_{\mathrm{cr2}}}{G_{\mathrm{ci1}}}\dfrac{L_1}{1+L_1}\dfrac{L_2}{1+L_2}}. \tag{I-7}$$

Appendix J: Experimental Prototypes of the Converters

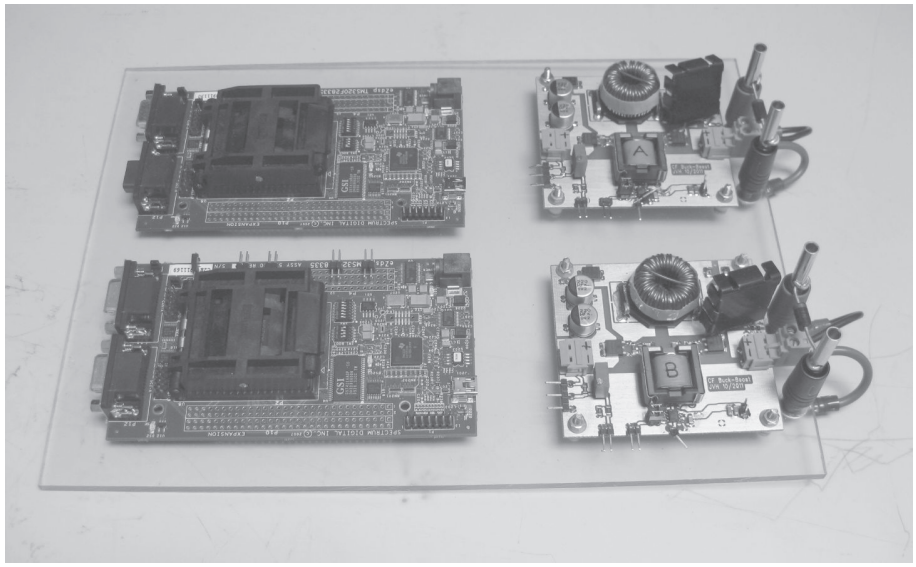

Fig. J-1. Buck-Boost Converters for DMPPT System.

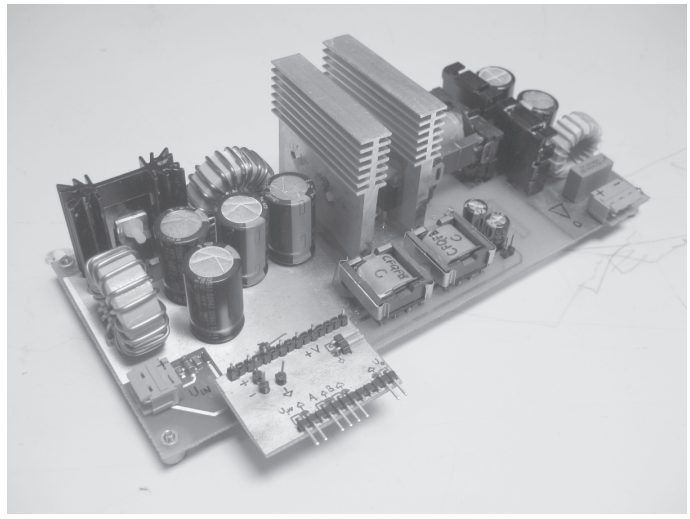

Fig. J-2. Current-Fed Quadratic Full-Bridge Buck Converter.

Appendix K: Measurement Setup and Lamp Unit for a PV Module

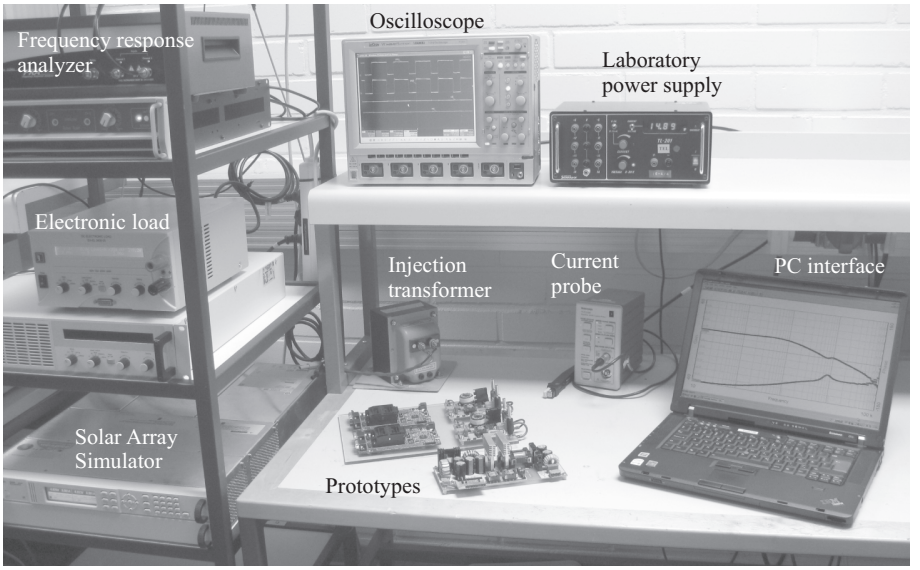

Fig. K-1. Overview on the measurement setup.

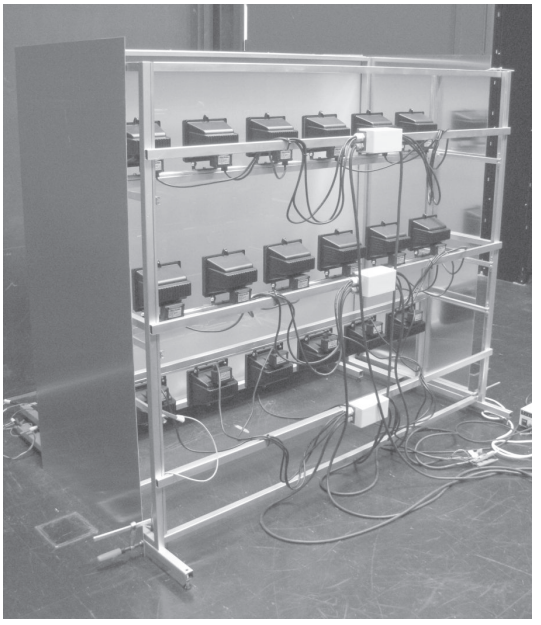

Fig. K-2. Lamp unit for illuminating the PV module.

Tampereen teknillinen yliopisto
PL 527
33101 Tampere

Tampere University of Technology
P.O.B. 527
FI-33101 Tampere, Finland

ISBN 978-952-15-2901-6
ISSN 1459-2045